Dipl.-Ing. Sebastian Hofer, BSc

Combining Grazing Incidence X-ray Diffraction with Computational Methods for Organic Semiconductor Structural Analysis

DOCTORAL THESIS

to achieve the university degree of
Doktor der technischen Wissenschaften

submitted to

Graz University of Technology

Supervisor
Ao. Univ.-Prof. Dipl.-Ing Dr.techn. Roland Resel
Institute of Solid State Physics
Graz University of Technology

Graz, July 2021

AFFIDAVIT

I declare that I have authored this thesis independently, that I have not used other than the declared sources/resources, and that I have explicitly indicated all material which has been quoted either literally or by content from the sources used. The text document uploaded to TUGRAZonline is identical to the present doctoral thesis.

Date, Signature

Abstract

The molecule 2-decyl-7-phenyl-[1]benzothieno[3,2-b][1]benzo-thiophene (Ph-BTBT-10) is an molecular semiconductor, with promising charge charrier mobilities and liquid crystalline behavior. This thesis presents a comprehensive structural characterization of the molecular packing based on X-ray diffractometry, which is extended by computational methods, with an emphasis on thin films. Films are prepared via solution processing by various methods and parameters, as well as by vacuum-based methods in the form of physical vapor deposition and characterized extensively. In a more fundamental investigation, a specific type of disorder that is present due to molecular shape anisotropy is described and modelled towards a possibility of extracting quantitative values of molecular ordering from diffraction experiments. The temperature dependent molecular packing motif in a liquid crystalline phase is resolved and discussed. A polymorph, produced by specific preparation conditions and stabilized by cross-nucleation of molecules is presented in a growth study. Finally, the charge carrier mobilities of shear coated samples with a preferred texture are investigated and correlated to structural properties of the film, revealing a case of charge-transport anisotropy along specific directions. The combined theoretical as well as experimental approach proves very valuable for the system in question and can be employed towards similar molecular systems, where a structural solution can be reached, even though diffraction data is insufficient.

Kurzfassung

Das Molekül 2-Decyl-7-phenyl-[1]benzothieno[3,2-b][1]benzo-thiophen (Ph-BTBT-10) ist ein molekularer Halbleiter mit vielversprechenden Ladungsträgermobilitäten und flüssigkristallinem Verhalten. Diese Dissertation präsentiert eine umfassende strukturelle Charakterisierung der molekularen Packung basierend auf Röntgendiffraktometrie, die durch computergestützte Methoden mit Schwerpunkt auf dünne Schichten erweitert wird. Proben werden mittels Lösungsmitteln nach verschiedenen Methoden und Parametern sowie durch vakuumbasierte Verfahren in Form der physikalischen Gasphasenabscheidung hergestellt und umfassend charakterisiert. In einer grundlegenderen Untersuchung wird eine spezifische Art von Fehlordnung, die aufgrund von molekularer Formanisotropie vorliegt, beschrieben und eine Möglichkeit modelliert, quantitative Werte der molekularen Ordnung aus Beugungsexperimenten zu extrahieren. Das temperaturabhängige molekulare Packungsmotiv in einer flüssigkristallinen Phase wird aufgelöst und diskutiert. In einer Wachstumsstudie wird ein Polymorph vorgestellt, das durch spezifische Präparationsbedingungen hergestellt und durch Kreuznukleation von Molekülen stabilisiert wird. Schließlich werden die Ladungsträgermobilitäten von scherbeschichteten Proben mit einer bevorzugten Textur untersucht und mit den strukturellen Eigenschaften des Films korreliert, was einen Fall von Ladungstransportanisotropie entlang bestimmter Richtungen offenbart. Der kombinierte theoretische und experimentelle Ansatz erweist sich für das analysierte System als sehr wertvoll und kann auf ähnliche molekulare Systeme angewendet werden, bei denen eine strukturelle Lösung erreicht werden kann, obwohl die Beugungsdaten unzureichend sind.

Acknowledgment

First of all, I want to thank my supervisor Roland Resel for providing me the opportunity to do a PhD in an amazing research group and his continuous support during the last couple of years. Both doing research on my own and being pushed in the right direction at times was excellently balanced under his oversight. I thank him dearly for broadening my scientific as well as my personal scope on life.

I would also like to thank all colleagues that I had the pleasure to work with. First and foremost, Benedikt Schrode, who was tirelessly helping me at the beginning to get into the basics of my research work and always had time for conversations. He is not only credited as the developer of the *GIDVis* software package, without which my data analysis would not have been possible, but also for excellent discussion and the realization that a coffee break with the right people can be more useful than a full day's work trying things alone.

I also want to acknowledge all the other current and previous members of the *k-room*, it was a pleasure to work with people you also genuinely enjoy spending time with.

No scientific work is ever done alone and I would like to thank all my collaborators. From Milano the group of Luca Beverina, from Barcelona the group of Marta Mas-Torrent, Jiří Novák from Brno and Josef Simbrunner from our own institute were excellent partners and I'm happy with the results we were able to produce.

A remarkable experience that I had the pleasure of coming in contact with, was measurements at Synchrotron facilities, which were not only astonishing from a scientific perspective but also a challenging personal feat. I regret no nightshift I

have ever done and would like to thank Luisa Barba at the XRD1 beamline at Elettra for her support.

After having acknowledged their help already two times in my past theses, I would like to thank my parents a final time for their never-ending support during my studies and providing me the opportunity to spend an amazing time in academia without needing to worry too much. I am truly grateful.

Contents

1 Introduction

The crystallization of materials, i.e. the formation of regular, periodic structures is an essential process that is relevant for applications in industry as well as for a fundamental understanding of the interactions of molecules and is a very complex procedure, especially in the context of thin films. Whereas the fabrication of crystalline materials as big single-crystals or fine powders is as standard technique in industry, the formation of thin films is not as well understood, due to the complexity that arises from the involved substrate surfaces. Generally, the formation of thin films can be described in thermodynamic equilibrium via consideration of the surface tension of the involved constituents, that contribute γ_S, γ_F and γ_{SF} as the surface energy of the substrate surface, the film and the interface between the substrate and the film, respectively, and the contact angle ϕ[1]:

$$\gamma_S = \gamma_{SF} + \gamma_F \cos(\phi)\,, \tag{1.1}$$

Films of a given material will grow in different growth modes, depending on the parameters above, i.e. they can form molecular islands, continuous layers or a combination of the two[2]. But the complex interactions of surfaces with molecules, as well as the interactions of the molecules themselves, in a system that is far away from thermodynamic equilibrium, is governed by the kinetics of many different competing processes and is generally not well understood. As such the morphology of the film is not the only characteristic one is interested in. The specific arrangement of molecules in a crystal, the packing motif, is extremely important for the properties that the film will show as it governs what

intermolecular interaction can exist. As the transport of charge carriers in a molecular crystal is strongly dependent on the packing [3,4], even small conformational changes can introduce huge differences in the electronic band structure[5]. In the case of molecular crystal this is even more important, as one molecule can exhibit many different packing motifs, i.e. it can form polymorphic phases[6,7]. These phases may be metastable but can be stabilized under specific preparation conditions and reveal improved properties when compared to the bulk structure[8]. When the effect is due to the interaction with the substrate, so-called substrate-induces phases can be observed[9,10], where the substrate itself does stabilize a specific phase. Furthermore, it can be due to the processing methods, i.e. the system does not have enough time to form the thermodynamically most favorable packing motif as the process happens too fast for it, e.g. when producing films via single molecular processes, e.g. physical vapor deposition, compared to slow evaporation of a solvent. Resolving the packing motif is thus a big challenge, if one is interested to be able to really describe the properties of a given material. In the context of single-crystals, diffraction techniques to solve the structure are state-of-the-art and can determine the packing with little effort. But thin films of crystalline materials remain an experimental challenge as special surface sensitives techniques need to be employed and the data is principally limited, due to the small size of the film. An extension of purely experimental methods is thus necessary, where computational modelling is used to support the restricted measured data with the goal of understanding the packing of molecules in thin films.

As systems get increasingly complex, the simple perfectly periodic structure of a crystal, seizes to be the most useful description and also disorder plays an important role. This disorder might be present due to weak inter-molecular interactions that are of the order of the thermal energy and liquid crystalline behavior might emerge, where the average position of the molecules show some regularity but molecules can move around similar to a liquid. But also, more general cases of disorder in a molecular system are to be considered, as any

deviation from the crystal structure can have pronounced implications for the properties of the resulting films.

This thesis is focused on a specific molecule that is investigated by means of X-ray diffraction methods and computational modeling, to show the applications and possibilities with such a combined approach. A brief introduction into the general topic of organic semiconductors and the specific molecule in question is provided and the concept of the crystallographic unit cell and how it is studied with diffraction experiments is given. Finally, the fundamentals will present an overview on the topic of liquid crystals and their orderings and nomenclatures. The used methods, i.e. the computational as well as the experimental techniques are explained before presenting the results of the work, in terms of the published manuscripts as well as publications that are still in preparation of publishing and related work.

2 Fundamentals

In this chapter an introduction to the theoretical background of the presented work will be provided. To start, an overview on the field of organic semiconductors is given, followed by an in-depth look on the molecule in question. The key features of molecular crystal structures are presented and expanded towards less-ordered systems, i.e. liquid crystals.

2.1 Organic Semiconductors

Conventional semiconductors are ubiquitous to our modern world and their production has been optimized to remarkable levels. Thus, transistors based on conventional semiconductor materials (e.g. Silicon) are the main component in almost all electronic devices. But an increasing interest is grown towards transistor application with certain specific features. Examples range from flexible and transparent substrates to bio-degradable devices, all with a focus on cheap, scalable production methods. Here organic semiconductor materials can prove to be very useful and furthermore, one can exploit the whole toolkit of organic chemistry to tune the materials desired properties.

The typical organic semiconductor is a flat, aromatic molecule, which then forms a molecular crystal by means of Van-der-Waals interaction. Such conjugated systems are shown to be promising candidates for possible electronic applications[11]. As organic materials they consist of carbon, which has six electrons in its ground state, resulting in an electronic configuration with two electrons in a 1s orbital, two in a 2s orbital and the final two in either $2p_x$, $2p_y$ or $2p_z$ orbitals. Those outer p orbitals will hybridize when bonding occurs and can form a π-bond

where the orbital is localized out-of-plane of the bond's direction. This has important consequences for the molecular crystal that an organic molecule might form. As the π-bond character in one flat molecule will show a quadrupole moment with a positive charge in the plane of the molecule and a negative one perpendicular to it, the minimum energy arrangement of a periodic arrangement of such molecules will usually exhibit a so-called herringbone arrangement (See Fig.1).

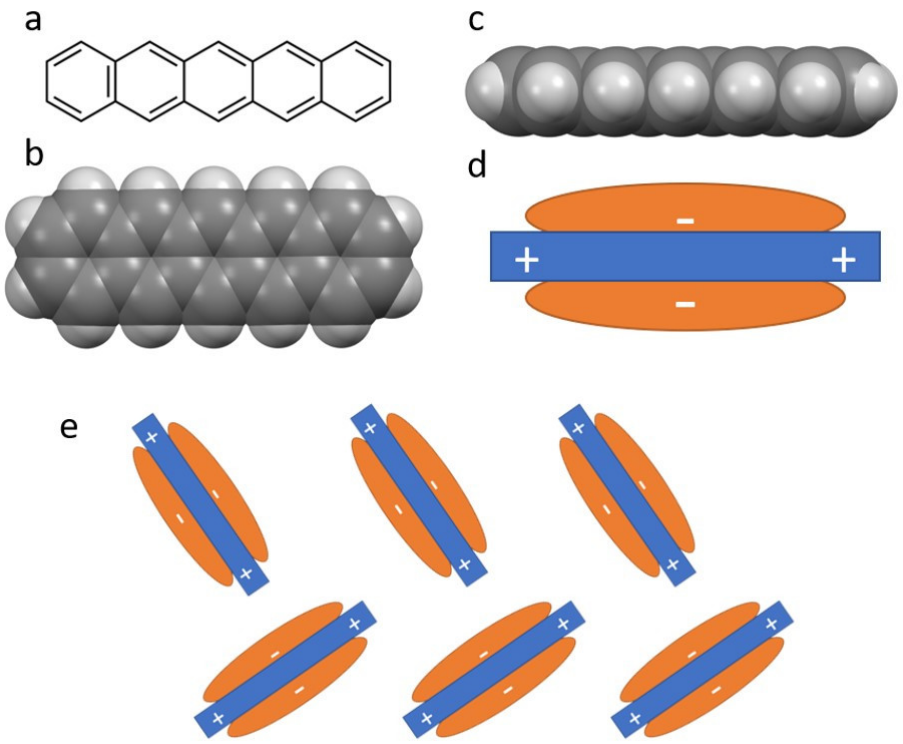

Figure 1: Chemical structure of the prototypical organic semiconductor pentacene (a), and its Van-der-Waals structure from top (b) and side (c) view. Electronic contributions in the π-system in an isolated molecule (d) and emergent property of herringbone packing from quadrupole interactions (e).

2.2 Ph-BTBT-C10

This section is intended to describe the main molecule of the work and summarize the current status of scientific work that was performed.

The molecule 2-decyl-7-phenyl-[1]benzothieno[3,2-b][1]benzo-thiophene (Ph-BTBT-10) received notoriety as it exhibits very high charge carrier mobilities of over 10 cm^2/Vs in thin film transistor devices[12]. It consist of a core based on benzothieno[3,2-b][1]benzo-thiophene (BTBT), a well-known organic semiconductor, that is modified with solubility groups on both sides. Literature[13] describes many different chemical moieties that can be used to modify the BTBT core, whereas in most cases the resulting molecule is symmetric, i.e. both sides have the same group attached. Contrary to this, the present molecule Ph-BTBT-10 has a phenyl ring on one end and a decyl chain on the other, resulting in a molecule with an asymmetric shape. Fig 2 depicts the molecular structure as well as the crystallographic packing motive in the bulk unit cell[14], which is monoclinic with unit cell parameters $\boldsymbol{a} = 6.0471\ \text{Å}, \boldsymbol{b} = 7.7568\ \text{Å}, \boldsymbol{c} = 53.124\ \text{Å}$ and $\gamma = 93.135°$. Typically for an aromatic conjugated unit the BTBT core forms a herringbone packing motif[15].

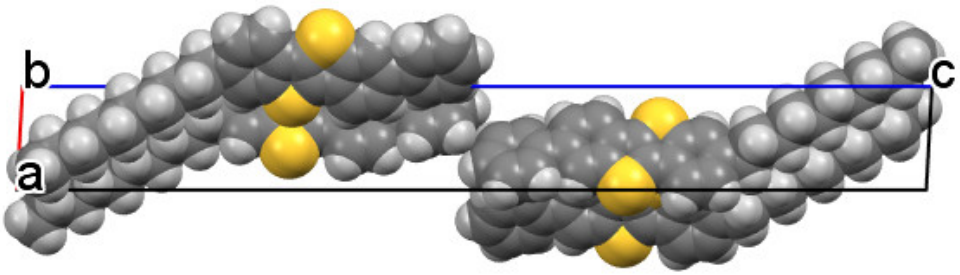

Figure 2: Crystal structure of the molecule Ph-BTBT-10 in the bulk unit cell.

Due to the long and rod like shape and the combination of a rigid core with flexible side chains the molecule exhibits the tendency to undergo liquid-crystalline phase transitions when heated[12]. It goes from the crystalline state to a *Smectic E* soft crystalline state and further on to a *Smectic A* phase, before melting. The exact

nature of those high temperature states is not fully resolved, but plays an important role in the formation of films with remarkable charge carrier mobilities[12,16]. A mechanism of inducing the Smectic E order in the system upon heating is described based on theoretical calculations[17,18], by which the bilayer structure undergoes a transition towards a single layer structure. Stabilization of this single layer packing motive at room temperature and achieving highly homogenous films based on it, appear to be crucial towards fabricating thin-film devices with high charge carrier mobilities[12,19].

2.3 Crystal Structure

The following chapter will briefly describe the basics of crystallography and the way it is accessed in a diffraction experiment.

A crystal describes a periodic arrangement of atoms in three-dimensional space. A convenient way to describe it mathematically is the concept of the crystallographic unit cell, which is generally a parallelepiped with the side lengths a, b and c and the angles $\alpha, \beta \text{ and } \gamma$. Those values are summarized as unit cell parameters, which depending on their values can be classified into a specific crystal system, e.g. cubic. The parallelepipeds side lengths, together with the angles, form a basis set of vectors, which are describes as:

$$\boldsymbol{a} = \begin{pmatrix} a \\ 0 \\ 0 \end{pmatrix}; \boldsymbol{b} = \begin{pmatrix} b\cos(\gamma) \\ b\sin(\gamma) \\ 0 \end{pmatrix}; \boldsymbol{c} = \begin{pmatrix} \mathrm{c}\cos(\beta) \\ c\,[\cos(\alpha) - \cos(\beta)]/\sin(\gamma) \\ V/([ab\sin(\gamma))] \end{pmatrix} \qquad (2.3.1)$$

With V, the unit cell volume, defined as:

$$V = (\mathbf{a} \times \mathbf{b}) \cdot \mathbf{c} = abc\sqrt{1 - \cos^2(\alpha) - \cos^2(\beta) - \cos^2(\gamma) + 2\cos(\alpha)\cos(\beta)\cos(\gamma)} \qquad (2.3.2)$$

The parallelepiped of an exemplary unit cell is shown in Figure 3, together with the basis vector that span it.

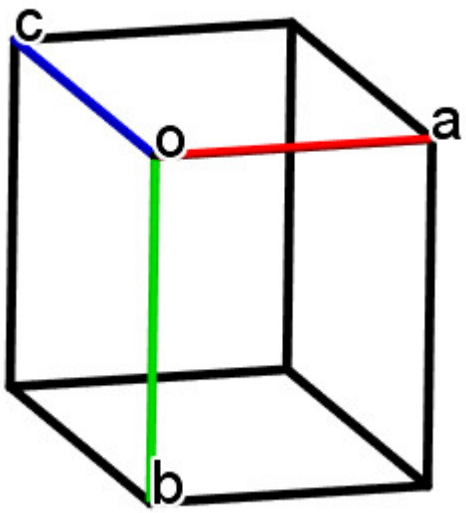

Figure 3: Crystallographic unit cell, constructed from basis vectors **a**, **b** and **c.**

In this unit cell, atoms are placed according to their basis, which describes on what position inside the unit cell which type of atom is sitting. Here the basis can be simple and describe only a couple of atoms (e.g. simple metals) but can get increasingly complex, e.g. when describing the position of individual atoms in a large protein. Once the unit cell and the basis are defined one can apply translational symmetry along integer multiples of the basis vectors **a**, **b** and **c** and thus describe a complete filling of three-dimensional space, i.e. any point $\boldsymbol{R}$ on the crystal lattice can be described as:

$$\boldsymbol{R} = u\,\boldsymbol{a} + v\,\boldsymbol{b} + w\,\boldsymbol{c} \quad u, v, w \in \mathbb{Z} \tag{2.3.3}$$

A useful concept, especially then using diffraction methods is the concept of reciprocal space, which is constructed by Fourier transform of the real space. In similar fashion to real space a crystal lattice can be constructed with reciprocal basis vectors $\boldsymbol{a}^*$, $\boldsymbol{b}^*$ and $\boldsymbol{c}^*$ defined as:

$$\boldsymbol{a}^* = 2\pi\,\frac{\boldsymbol{b} \times \boldsymbol{c}}{\boldsymbol{a} \cdot (\boldsymbol{b} \times \boldsymbol{c})} \tag{2.3.4}$$

$$\boldsymbol{b}^* = 2\pi \frac{\boldsymbol{a} \times \boldsymbol{c}}{\boldsymbol{a} \cdot (\boldsymbol{b} \times \boldsymbol{c})} \tag{2.3.5}$$

$$\boldsymbol{c}^* = 2\pi \frac{\boldsymbol{a} \times \boldsymbol{b}}{\boldsymbol{a} \cdot (\boldsymbol{b} \times \boldsymbol{c})}, \tag{2.3.6}$$

with the lattice vectors in reciprocal space now defined as:

$$\boldsymbol{G}_{hkl} = h\,\boldsymbol{a}^* + k\,\boldsymbol{b}^* + l\,\boldsymbol{c}^* \quad h,k,l \in \mathbb{Z} \tag{2.3.7}$$

With the knowledge of $\boldsymbol{G}_{hkl}$ one can now easily denote specific crystallographic planes with a set if indices *h*, *k* and *l*, describing one specific reciprocal lattice vector, that is perpendicular to the net plane *(hkl)*. The net plane distance d_{hkl} is also related directly to the length of the reciprocal lattice vector via:

$$d_{hkl} = \frac{2\,\pi}{|\boldsymbol{G}_{hkl}|} \tag{2.3.8}$$

The nomenclature via the set of indices *{hkl}* is as follows: a direction in reciprocal space is denoted with square brackets *[hkl]*, a plane with round brackets *(hkl)* and a diffraction peak with just the set of indices *hkl*.

With the knowledge of the reciprocal space the description of diffraction can now be made very elegantly and convenient.

2.4 Diffraction

Diffraction is a general phenomenon that is observed when a wave hits an object. The wave gets elastically scattered around the obstacle, which in terms can then be viewed as a new source for a propagating wave; an effect described as the Huygens-Fresnel principle. If in this picture the new sources for propagating waves are now arranged in a periodic fashion, their individual contributions can interfere with each other and produce a distinct so-called diffraction pattern. This effect occurs if the wavelength of the used light source is of similar order to the size of the objects that are illuminated. Looking at a molecular crystal the interatomic distances and the crystallographic net planes are of the order of 10^{-10} m = 1 Å,

which makes it necessary to use a light source with an X-ray wavelength to produce this effect in a molecular crystal, as typical X-ray wavelengths are of the same order of magnitude (e.g. one of the most used X-ray sources are from the Cu-Kα line at 1.54 Å).

An X-ray beam that illuminates a sample can be described with an incoming wavevector $\boldsymbol{k}_{in}$ that hits the thin film sample under an angle α_i and a diffracted beam with a wavevector $\boldsymbol{k}_{\boldsymbol{out}}$, that exits with an angle α_f. In the so-called specular condition, the incident angle equals the outgoing angle and both are labeled θ, resulting in the definition of the scattering angle as 2θ. Based on the wavevectors a scattering vector $\boldsymbol{q}$ is defined as $\boldsymbol{q} = \boldsymbol{k}_{out} - \boldsymbol{k}_{in}$, which can now be used to formulate the condition for constructive interference in a diffraction event to occur as in a very concise way:

$$\boldsymbol{G} = \boldsymbol{q}, \tag{2.4.1}$$

which is the so called Laue condition[20]. It describes that constructive interference will be observed if the momentum transfer $\boldsymbol{q}$ equals a reciprocal lattice vector $\boldsymbol{G}_{hkl}$. An equivalent description can be given in real space, the Bragg-condition of diffraction[21]. Here the additional path a beam travels when passing through the net planes of a crystal needs to be an integer multiple n of the beam's wavelength λ which is summarized as:

$$n\lambda = 2d_{hkl} * \sin\left(\frac{2\theta}{2}\right) \tag{2.4.2}$$

A sketch of the two diffraction conditions and the physical quantities that are used in the description is presented in Fig. 4.

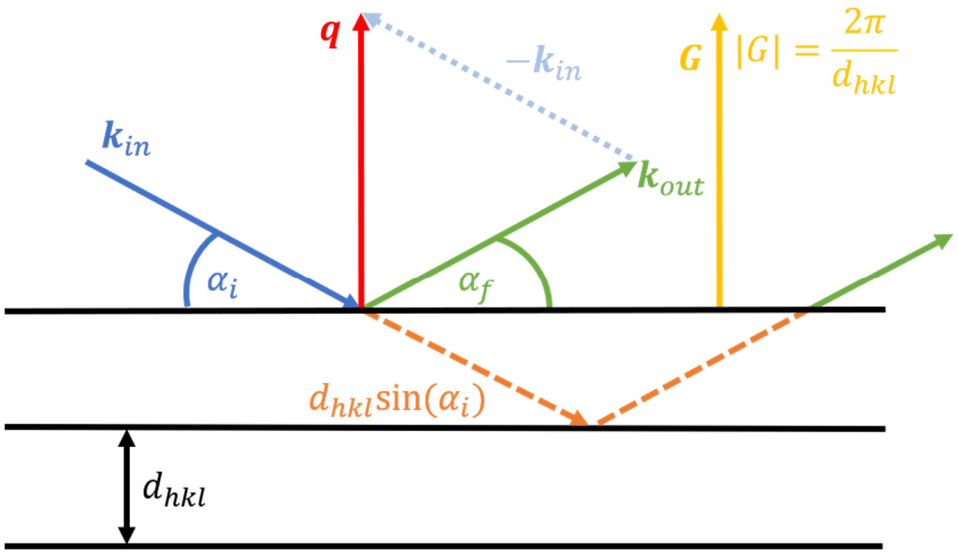

Figure 4: Schematic picture of the vectors and distances used in describing the Bragg- and Laue-conditions of diffraction.

The conditions above describe at what angles or scattering vectors the condition for constructive interference is satisfied and a diffraction peak will be observed. The intensity of the peak is dependent on the arrangement of the electrons within the crystallographic unit cell. The concept to describe this is the structure factor $F(\boldsymbol{q})$, which is defined as the Fourier transform of the electronic density $\rho(\boldsymbol{r})$ along the volume of the unit cell V_{UC}:

$$F(\boldsymbol{q}) = \int_{V_{UC}} \rho(\boldsymbol{r}) \exp(i\boldsymbol{q}\boldsymbol{r})\, d^3\boldsymbol{r}\,, \tag{2.4.3}$$

which can now be written by utilizing the Laue condition in the case of diffraction as:

$$F_{hkl} = \int_{V_{UC}} \rho(\boldsymbol{r}) \exp(i\boldsymbol{G}\boldsymbol{r})\, d^3\boldsymbol{r}\,. \tag{2.4.4}$$

The vector $\boldsymbol{r}$ is now split up into two parts, one as the basis vector of the ith atom within the unit cell $\boldsymbol{r_i}$ and one describing the position of neighboring cells $\boldsymbol{r'}$:

$$\boldsymbol{r} = \boldsymbol{r_i} + \boldsymbol{r'}. \tag{2.4.5}$$

We can now write the structure factor as a summation of the contributions of all the atoms within the unit cell and integrating smaller volumes of the individual atoms V_{A_i}:

$$F_{hkl} = \sum_i \int_{V_{Ai}} \rho(\boldsymbol{r}') \exp[i\boldsymbol{G}(\boldsymbol{r}_i + \boldsymbol{r}')] d^3\boldsymbol{r}'$$

$$= \sum_i \exp(i\boldsymbol{G}\boldsymbol{r}_i) \int_{V_{Ai}} \rho(\boldsymbol{r}') \exp[i\boldsymbol{G}\boldsymbol{r}'] d^3\boldsymbol{r}'. \quad (2.4.6)$$

The last integral describes the electronic density inside the volume of one individual atom and is the so-called atomic form factor f_i of atom i. Those values are tabulated[22] for all the elements and usually approximated as a sum of Gaussians functions. Here shall be briefly mentioned that the usual approach is to deduce F_{hkl} from measurements and therby gain insights into an unknown ρ. As will be presented later, the inverse problem is of interest as well, where one uses a model of ρ for a known structure to understand the features that are obtained in F_{hkl}. A further simplification of the structure factor for the diffraction peak hkl can now concisely be formulated as:

$$F_{hkl} = \sum_i f_i \exp(i\boldsymbol{G}\boldsymbol{r}_i)\,. \quad (2.4.7)$$

The detected intensity in a diffraction experiment is proportional to the absolute square of the structure factor:

$$I \propto |F_{hkl}|^2. \quad (2.4.8)$$

The fact that only the magnitude can be measured experimentally and the phase information is lost by squaring, complicates the inference of the structure based on the measured peak intensities; crystallographers call it the phase-problem, as crucial information, that it within the phase, is lost. Solving the phase-problem just from diffraction data without any additional information, usually relies on a huge number of collected peak intensities and statistical analysis of the data, and is thus only really possible when dealing with single-crystalline materials. A general approach in the case of thin-films, where diffraction data is sparse emphasizes the need for molecular modeling together with specialized diffraction techniques.

2.5 Grazing Incidence X-ray diffraction

A drawback in regular diffraction experiments is the fact that X-ray do only interact weakly with matter and thus penetrate through most materials, which is especially disadvantageous when dealing with thin films. One diffraction method that is frequently used for such films is the method of Grazing Incidence X-ray diffraction (GIXD). Here the incident wavevector $\boldsymbol{k}_{in}$ illuminates the sample under a very small incident angle α_i. If the angle is on the order of 1° it is close to the critical angle of total external reflection and theoretically no penetration into the material should happen. But due to the interface conditions of electric field vectors (i.e. the tangential components are continuous at an interface) the electric field does not decrease to zero as soon as the interface is hit, but instead a wave is formed that decreases exponentially into the substrate. This so-called evanescent wave is precisely localized at the interface and cannot penetrate further into the sample, so the observed diffraction data must stem from thin films directly at the surface. The penetration depth can be directly controlled by appropriate choice of the incidence angle α_i. This surface wave can propagate on the sample surface and thereby diffract on periodic structures in the plane of the substrate, resulting in a three-component scattering vector $\boldsymbol{q}$ that can satisfy the Laue-condition now in three-dimensional reciprocal space. Scattered intensity is usually collected on a large two-dimensional detector, which results in the usually way of presenting GIXD data as 2D-images with the in-plane component q_{xy} and the out-of-plane component q_z of the scattering vector. A sketch of the setup is presented in Fig. 5

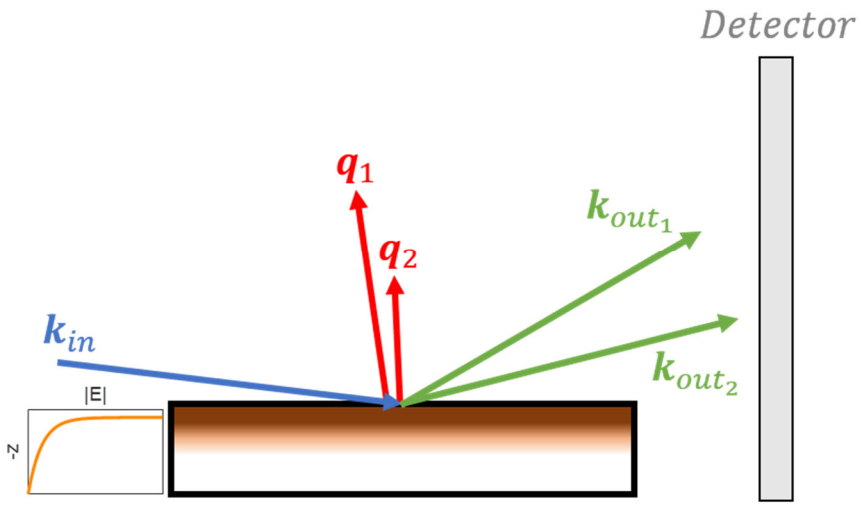

Figure 5: Wave- ($k_{in}, k_{out_1}, k_{out_2}$) and scattering vectors (q_1, q_2) in a grazing incidence diffraction setup and intensity of surface wave as a function of depth into the sample due to evanescence.

2.6 Liquid Crystals

Liquid crystals are a state of matter that shows properties that can be described as a mixture between the liquid state and a conventional solid crystal. They are prominent in industry as functional material in liquid crystal displays (LCDs) but also ubiquitous in nature. Different classes of liquid crystals can be distinguished, based on the amount of order that is present in the system but also in terms of the underlying mechanism for ordering. As such liquid crystals can be grouped into the class of thermotropic and lyotropic liquid crystals, whereas only the former will be discussed in this thesis.

In said class of liquid crystals, the order/disorder is a function of temperature. Thermotropic liquid crystals will usually form a conventional crystal at low temperature and will melt into an isotropic liquid at high temperatures, with distinctly different phases in-between.

The materials that can show liquid crystalline behavior are usually organic molecules with a certain asymmetry in shape that is described as either rod-like (calamitic) or disc-like (discotic). Examples for prototypical examples are given in Fig 6 with a sketch to visualize their overall shape.

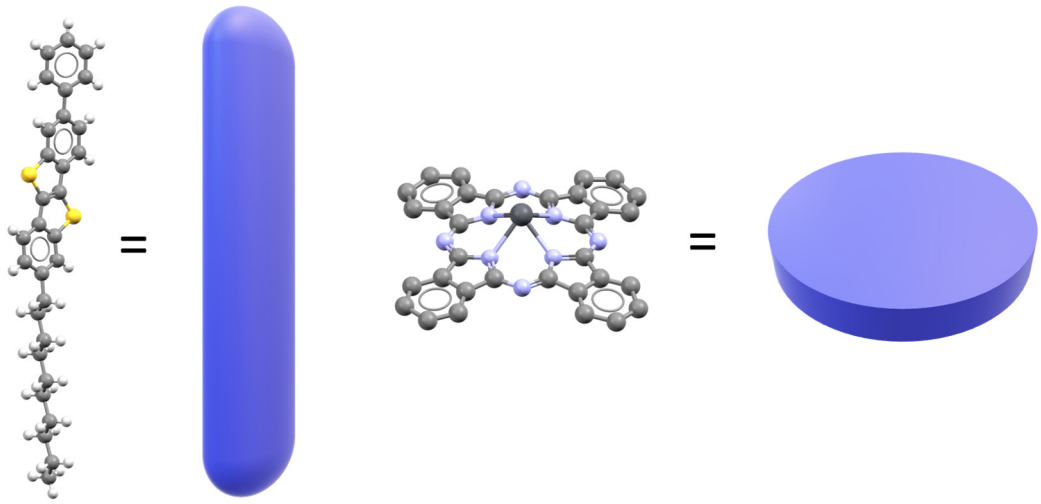

Figure 6: Ph-BTBT-10 and a phthalocyanine molecule together with their abstracted overall molecular shape.

The following description of order will be without loss of generality reduced to the calamitic system. As the overall behavior of the individual molecules is more liquid-like any order that is observed only extends to finite ranges; one thus is classifying it as more of a short-range order compared to the principally infinitely reaching long-range order in specific directions in a conventional crystal. In any liquid crystalline system, the degree of order can be quantified by introduction of an order parameter. For directional order (the first type of order that is present in so-called nematic systems) it describes the average orientation of the angle θ of the molecular axis with respect to a certain direction in space, specified by a director vector $\boldsymbol{n}$ as:

$$\Phi_d = \langle \frac{3}{2} \cos^2 \theta - \frac{1}{2} \rangle \qquad (2.6.1)$$

A value of $\Phi_d = 1$ would describe a perfectly ordered system whereas $\Phi_d = 0$ holds true for the completely isotropic case. Fig 7 shows a sketch of the directional ordering in a nematic phase.

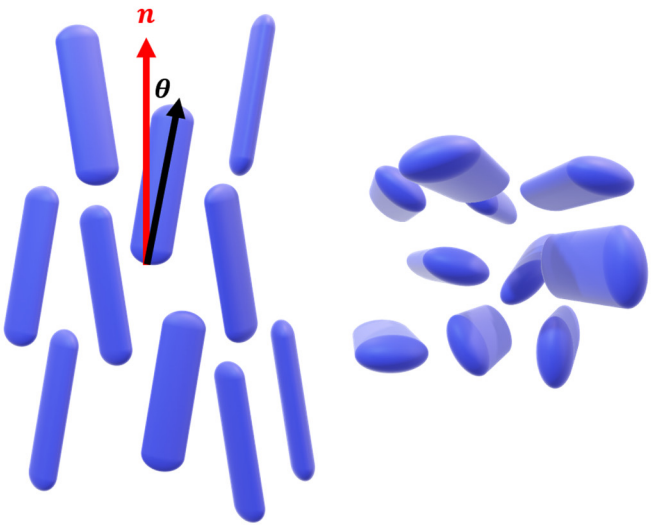

Figure 7: Nematic system with director $\boldsymbol{n}$ and orientation angle θ from side (left)- and top-view (right).

Additional to the directional order the molecules can also be arranged at specific points in space, i.e. positionally ordered. Usually this means a preferred occupation of molecular layers and can be similarly described with an order parameter. This positional order parameter Φ_p is used to relate the density $\rho(z)$ along a layer normal with an isotropic density and a periodic modulation with period $\frac{2\pi}{d}$ via:

$$\rho(z) = \rho_0 \left[1 + \Phi_p \cos\left(\frac{2\pi z}{d}\right)\right] \tag{2.6.2}$$

A system that shows one-dimensional positional order within layers is called a smectic system and a sketch is provided in Fig. 8

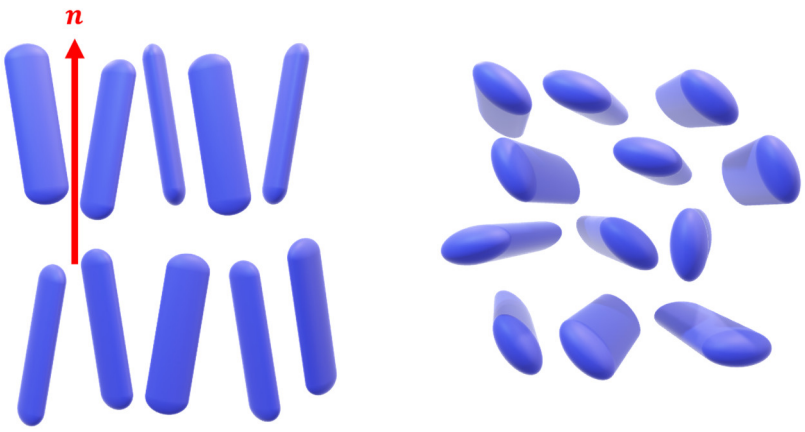

Figure 8: Smectic system with layered positional order from side (left)- and top-view (right).

Within the smectic layers the molecules can show additional directional order, and the smectic phases are classified depending on this interplay of the different order contributions. A detailed insight can be found in literature[23], here just a brief overview is provided. The smectic phases can be distinguished by their showing of either orthogonal or tilted directional order on the one hand and by their random or hexagonal positional order within the plane of the layer on the other hand. The hexagonal positional order is usually termed hexatic and is in-between short- and long-range order, where molecules form an approximately hexagonal packing but really only with their nearest neighbors. Those arrangements can then extend to distances larger than the classically short-range order or even the hexatic one and are then categorized as a so-called soft crystalline phase. As this distinction is not so straight-forward the nomenclature of soft crystal phases is usually still in terms of specific smectic phases (e.g. in literature the terms *Crystal E* and *Smectic E* to describe a specific phase are both used[24,25]). Table 1 shall provide an overview on the classification of smectic phases and Fig 9 a sketch of the Smectic E system, the most important case for the present work.

Table 1 Nomenclature of smectic phases with respect to the positional order and directional order

	Orthogonal directional order	Tilted directional order
Short-range positional order	Smectic A	Smectic C
Hexatic positional order	Smectic B	Smectic I/F
Long-range positional order	Smectic E	Smectic J/G/K/H

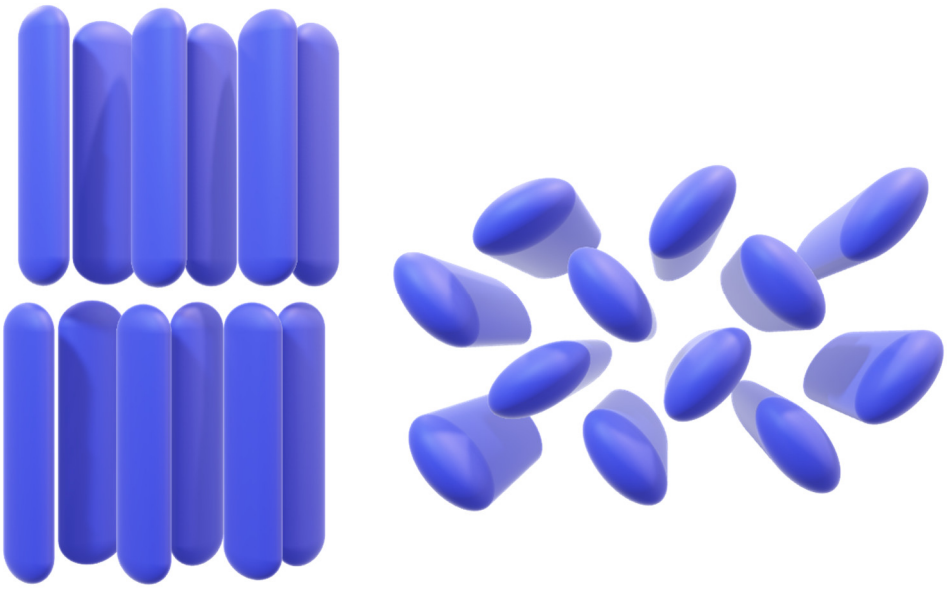

Figure 9 *Smectic E* system with layered positional order, orthogonal molecules and hexatic in-plane packing from side (left)- and top-view (right).

It can thus be concluded that, due to the presence of a certain degree of long-range order, smectic phases can be analyzed by diffraction methods, that reveal their periodicities and distinct diffraction peaks are to be expected.

3 Methods

In this section the employed methods will be discussed in more detail. It is split up into two parts. First a general introduction of the concept of Molecular Dynamics and how it is actually implemented to the general approach that is used in this thesis to solve structures. The second part deals with the topic of X-ray reflectivity and the way electron densities can be determined as well as modelled in terms of layered thin film samples.

3.1 Molecular Dynamics

This chapter shall give an overview on the technique of Molecular Dynamics (MD) simulations and how it can be used to solve crystal structures based on limited diffraction information. For a more detailed introduction further information can be found in literature[26].

3.1.1 Basics

On a very fundamental level, the general idea of MD is to get the time evolution of a system by integrating the equations of motion of the systems constituents. The starting point here is Newtons law:

$$\boldsymbol{F} = m\,\boldsymbol{a}, \tag{3.1.1.1}$$

which can be expanded towards a system of different interacting particles and their corresponding equation of motion:

$$\ddot{x}_{i\alpha}(t) = \frac{1}{m_i} F_{i\alpha}[\boldsymbol{r}(t), t]. \qquad (3.1.1.2)$$

Here $x_{i\alpha}$ describes the α^{th} coordinate of the particle with index i. The vector **r** represents the collection of different coordinates $\{x_{i\alpha}\}$. In an analogous fashion, one can collect the set of forces $\{F_{i\alpha}\}$ into a vector $\boldsymbol{f}$ and put the equations of motion into a very concise form:

$$\ddot{\boldsymbol{r}}(t) = \boldsymbol{f}[\boldsymbol{r}(t), t]. \qquad (3.1.1.3)$$

As this is not generally solvable analytically for systems with more than two particles, the idea now is to integrate the equation of motion in discrete time steps τ. Different algorithms for this exist and in the following the Verlet algorithm will be presented and adapted for better stability.

3.1.2 Verlet Algorithm

The solution of the equations of motion starts off by expanding the coordinates of a particle in a Taylor series:

$$\boldsymbol{r}(\tau) = \boldsymbol{r}(0) + \tau\, \dot{\boldsymbol{r}}(0) + \frac{\tau^2}{2}\ddot{\boldsymbol{r}}(0) + \frac{\tau^3}{6}\dddot{\boldsymbol{r}}(0) + O(\tau^4)$$

$$\boldsymbol{r}(-\tau) = \boldsymbol{r}(0) - \tau\, \dot{\boldsymbol{r}}(0) + \frac{\tau^2}{2}\ddot{\boldsymbol{r}}(0) - \frac{\tau^3}{6}\dddot{\boldsymbol{r}}(0) + O(\tau^4)$$

$$\rightarrow \boldsymbol{r}(\tau) + \boldsymbol{r}(-\tau) = 2\boldsymbol{r}(0) + \tau^2\, \ddot{\boldsymbol{r}}(0) + O(\tau^4), \qquad (3.1.2.4)$$

which can be rewritten utilizing Formula 5 and neglecting terms of $O(\tau^4)$ as:

$$\boldsymbol{r}(\tau) = 2\boldsymbol{r}(0) - \boldsymbol{r}(-\tau) + \tau^2\, \boldsymbol{f}[(\boldsymbol{r}(0), 0)]. \qquad (3.1.2.5)$$

At the very beginning the knowledge of $\boldsymbol{r}(-\tau)$ would be needed, which is mitigated by defining the position at the first timestep as:

$$\boldsymbol{r}(\tau) = \boldsymbol{r}(0) - \tau\, \boldsymbol{v}(0) + \frac{\tau^2}{2}\boldsymbol{f}[(\boldsymbol{r}(0), 0)]. \qquad (3.1.2.6)$$

One is left with a solution for the equations of motion at discrete timesteps ($t = \tau, 2\tau, \ldots$):

$$\boldsymbol{r}(t+\tau) = 2\boldsymbol{r}(t) - \boldsymbol{r}(t-\tau) + \tau^2\, \boldsymbol{f}[(\boldsymbol{r}(t), t)]. \qquad (3.1.2.7)$$

If one is interested in the velocities of the particles directly, they can be described as:

$$\boldsymbol{r}(t+\tau) - \boldsymbol{r}(t-\tau) = 2\tau\, \boldsymbol{v}(t) + O(\tau^3), \qquad (3.1.2.8)$$

and utilized in the algorithm directly by calculating both the positions and velocities, which results in an equivalent formulation to Equ. 3.1.2.7 that is more robust towards numerical errors and is termed the Velocity-Verlet Algorithm:

$$\boldsymbol{r}(t+\tau) = \boldsymbol{r}(t) - \tau\, \boldsymbol{v}(t) + \frac{\tau^2}{2}\, \boldsymbol{f}[(\boldsymbol{r}(t), t)] \text{ and}$$

$$\boldsymbol{v}(t+\tau) = \boldsymbol{v}(t) + \frac{\tau}{2}\{\, \boldsymbol{f}[(\boldsymbol{r}(t), t)] + \boldsymbol{f}[(\boldsymbol{r}(t+\tau), t+\tau)]\}. \qquad (3.1.2.9)$$

One is now left with an algorithm to solve the equations of motion of particles, given that all the forces $\boldsymbol{f}$ in the system are known. In that sense the situation can now go from a purely classical description of Newtonian mechanics to a proper description of quantum systems by introducing appropriate parameters for the forces between particles.

3.1.3 Force fields

Appropriate parameters for the forces between particles, as desired in the previous chapter, are described in the context of computational chemistry and physics in so called force fields. The interatomic forces between different atoms and molecules can then be directly extracted as the gradient of a potential energy surface. The parameters can be either measured experimentally and tabulated or calculated quantum mechanically, depending on the chosen force field, also both is possible. A logical extension can be made in chemistry, where one is not only parametrizing the interatomic interactions between single atoms, but whole

chemical groups (i.e. the torsion potential of a phenyl ring, attached on a C atom can be extracted from spectroscopic methods and does not need to be depending on the single atom interactions of seven C atoms).

The general form of the potential energy in a molecular system has the form:

$$E_{total} = E_{bonded} + E_{nonbonded}, \tag{3.1.3.1}$$

with the components consisting of:

$$E_{bonded} = E_{bond} + E_{angle} + E_{dihedral} \text{ and}$$

$$E_{nonbonded} = E_{electrostatic} + E_{Van\ der\ Waals}. \tag{3.1.3.2}$$

A visualization of the different bonded terms above is given in Figure 10.

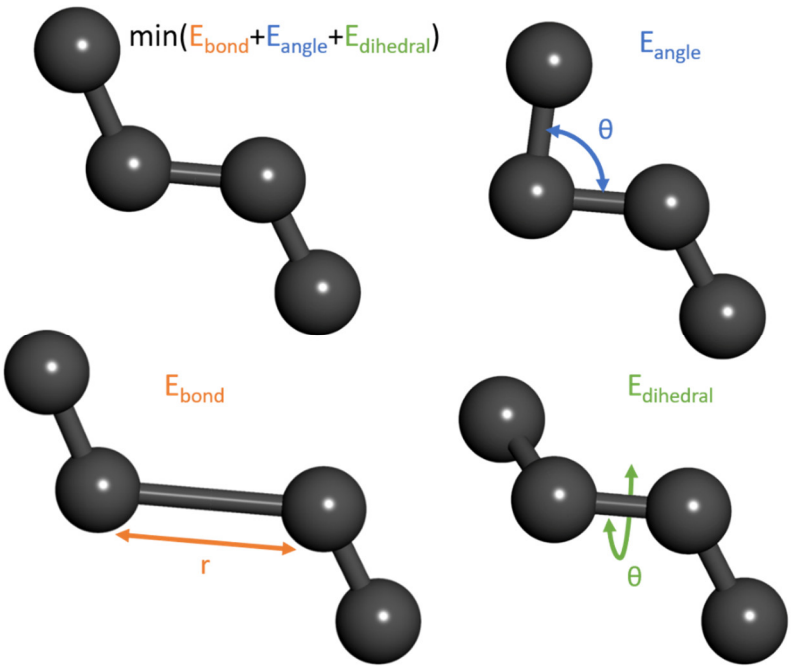

Figure 10: Schematic of the different bonded energy contributions in a molecular system and the resulting minimum energy configuration.

The nonbonded terms consist of an electrostatic part, described via Coulombs Law:

$$E_{electostatic} \propto \frac{q_i q_j}{r_{ij}} \tag{3.1.3.3}$$

and a Van der Waals Term, usually described with a Lennard-Jones Potential:

$$E_{Van\ der\ Waals} = \frac{a_{ij}}{|r_{ij}|^{12}} - \frac{b_{ij}}{|r_{ij}|^{6}}, \qquad (3.1.3.4)$$

with appropriate constants a_{ij}, b_{ij}.

3.1.4 Structure solutions

Now that the algorithm to solve the equations of motion are formulated and the forces in the system are defined one can proceed towards applying them to molecules to find their molecular packing motif. A recipe for it is shown in Figure 11.

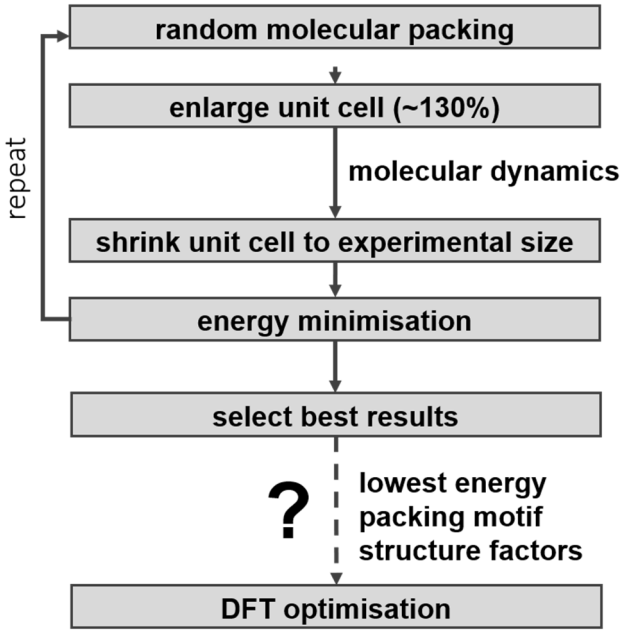

Figure 11: Algorithm for the structure solution based on MD simulations.

Hereby the starting values are the unit cell parameters, that have been measured from a diffraction experiment. This unit cell is then expanded by a well-defined value and the molecules are placed with a random orientation into this expanded cell. During the simulation run the unit cell is then shrunken down continuously, while the molecules can arrange themselves into a molecular packing with low

energy. At the end of the run the energy is minimized again and one is left with a candidate structure. As the process is computationally very cheap when the system is small, it can be repeated 1000s of times to, depending on the initial configuration, the whole space of possible packing motifs is probed. To then be able to compare the structures to some experimental values the candidate structures are clustered into distinctly different motifs. The basis for this is the molecular similarity based on the Hausdorff metric. Examples from each cluster are then used to calculate the squared structure factors for each diffraction peak, a value that is proportional to the measured peaks intensities. If all the measured intensities are explained with a candidate structure, optionally, more expensive methods like Density Function Theory (DFT) can be employed to get a more refined structural model of the solved phase.

3.2 X-ray reflectivity and electron density modeling

A technique to probe the electron density as well as the precise morphology of thin layers is X-ray reflectivity (XRR), where the optical properties of X-rays are used to characterize materials. The general principle is the refraction of electromagnetic waves, i.e. the change in the direction of a propagating wave when moving from one medium to another one, governed by the medias respective index of refraction n. Due to the high energy (and thus frequency) of X-rays the dispersion, upon passing a medium, lies in the anomalous regime as resonant interaction between the atoms and molecules cannot couple to the incident frequency of the wave. This results in an index of refraction smaller than unity, which is described in terms of the incident wavelength λ, the electron density of the material ρ_e, the linear absorption coefficient μ_x, and the constants for the classical electron radius r_e as:

$$n = 1 - \frac{\lambda^2}{2\pi} r_e \rho_e - i \frac{\lambda}{4\pi} \mu_x = 1 - \delta - i\beta. \qquad (3.2.1)$$

The real part of n describes the refractive interactions, whereas the imaginary part gives the absorption.

With the refractive index, the optics of an X-ray beam after transitioning through media can now be described. The incident wavevector $\boldsymbol{k}_{in}$ with amplitude a_{in} hits the surface under an angle α and is both reflected (wavevector $\boldsymbol{k}_r$ with amplitude a_r under the same angle α) and transmitted into the medium (wavevector $\boldsymbol{k}_t$ with amplitude a_t with a different angle α'). Fig 12 summarizes the involved values.

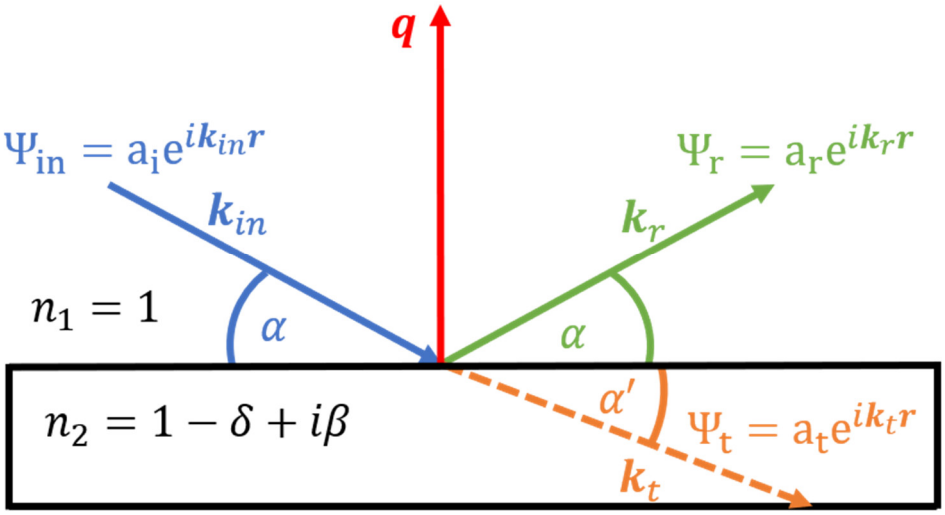

Figure 12: Schematic picture of the wavevectors ($\boldsymbol{k}_{in}, \boldsymbol{k}_r, \boldsymbol{k}_t$) with corresponding wavefunctions ($\Psi_{in}, \Psi_r, \Psi_t$), scattering vector ($\boldsymbol{q}$) and angles ($\alpha, \alpha'$) in a refractive and reflective system.

The Fresnel equations from optics can now be used to derive an amplitude reflectivity r and transmittivity t (for a detailed derivation of the following topics refer to literature[27]):

$$r \equiv \frac{a_r}{a_i} = \frac{\sin(\alpha) - \sin(\alpha')}{\sin(\alpha) + \sin(\alpha')} \text{ and } t \equiv \frac{a_t}{a_i} = \frac{2\sin(\alpha)}{\sin(\alpha) + \sin(\alpha')}. \tag{3.2.2}$$

An equivalent formulation in terms of the length of the scattering vector $\boldsymbol{q}$ is directly possible via $q = \frac{4\pi}{\lambda} * \sin(\alpha)$ resulting in a formulation of r and t in terms of q as:

$$r(q) = \frac{q - q'}{q + q'} \text{ and } t(q) = \frac{2q}{q + q'}. \tag{3.2.3}$$

The reflectivity and transmittivity value can now be used to formulate a description of the interaction in layered systems which is illuminated by an X-ray beam. Whereas for an infinitely thick material with a constant index of refraction the situation is fully described by Snell's law: $n_1 \cos(\alpha') = n_2 \cos(\alpha)$, it gets more complicated for finite sized slabs: Reflection can happen at the interface 0 (vacuum/air) to 1 (slab) with a contribution r_{01}; Transmission at the interface 0 to 1 with t_{01} followed by either reflection at the interface 1 to 2 with r_{12} or transmission out of the slab with t_{12}. The wave reflected at the interface 1 to 2 will then again be able to reflect or transmit at the interface 0 to 1 and so on, each time picking up an additional phase factor $\Phi = \left(e^{iqd}\right)^2$ with d the thickness of the slab. Fig 13 visualizes the different reflection and transmission events in a slab of finite thickness.

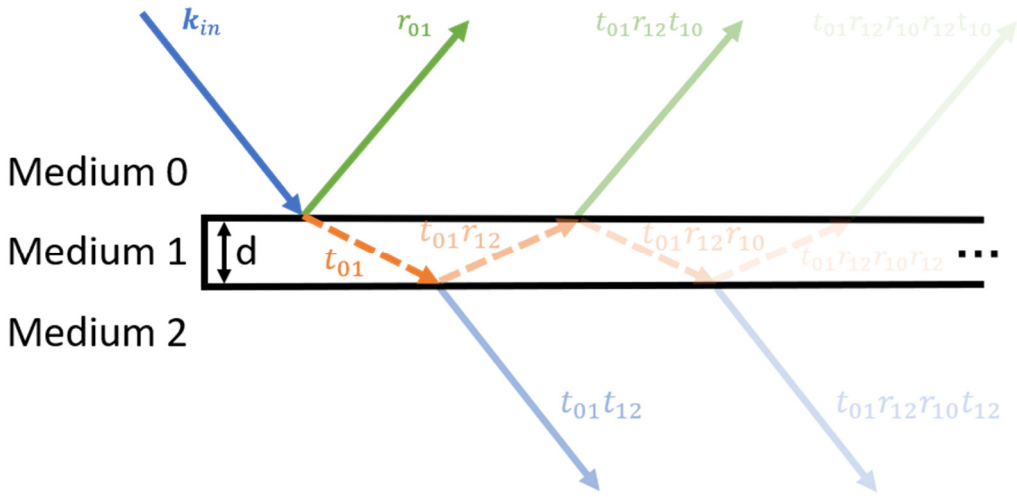

Figure 13: Schematic view of the infinite transmission/reflection event that can occur due to multi-scattering in a slab sample.

The resulting infinite sum for the reflectivity of a slab can be written as:

$$r_{slab} = r_{01} + t_{01}t_{10}r_{12}\Phi + t_{01}t_{10}r_{10}r_{12}^2\Phi^2 + t_{01}t_{10}r_{10}^2r_{12}^3\Phi^3 + \cdots,$$
$$= r_{01} + t_{01}t_{10}r_{12}\Phi \sum_{n=0}^{\infty} (r_{10}r_{12}\Phi)^n, \qquad (3.2.4)$$

which can be evaluated as:

$$r_{slab} = r_{01} + t_{01}t_{10}r_{12}\Phi\frac{1}{1 - r_{10}r_{12}\Phi}. \tag{3.2.5}$$

Simplification can be made by using Equation 3.2.3 and symmetry (i.e. the same media in 0 and 2) and the reflectivity of a single slab of finite thickness becomes:

$$r_{slab} = \frac{r_{01}(1 - \Phi)}{1 - r_{01}^2\Phi}. \tag{3.2.6}$$

The result can now be abstracted towards system with more layers of different electronic densities, where equivalent to the description above, the beam can either reflect or transmit at each interface and pick up a phase factor. A formalism developed by Parratt in 1954[28] allows for an iterative procedure to resolve the reflectivity of a multilayered system (with densities 1 to N) which is formed on a thick substrate (as a boundary). It starts off from the bottom most layer with the substrate, which is in principle infinitely thick and no multiple reflections can occur as:

$$r'_{N,\infty} = \frac{q_N - q_\infty}{q_N + q_\infty}, \tag{3.2.7}$$

and iteratively working up to the next layer with:

$$r_{N-1,N} = \frac{r'_{N-1,N} + r'_{N,\infty}\Phi_{\mathrm{N}}}{1 + r'_{N-1,N}r'_{N,\infty}\Phi_{\mathrm{N}}}. \tag{3.2.8}$$

Here the prime at the values r describes a reflectivity amplitude that does not consider multiple scattering directly from Equation 3.2.3. The reflectivity of all the layers can now be described recursively until one reaches the final interface of the vacuum with the top-layer:

$$r_{N-2,N-1} = \frac{r'_{N-2,N-1} + r'_{N-1,N}\Phi_{\mathrm{N}-1}}{1 + r'_{N-2,N-1}r'_{N-1,N}\Phi_{N-1}}. \tag{3.2.9}$$

In a last step, the thickness of the individual layers can be made infinitesimally small with a continuous change in the electron density and the description goes towards the generalized case of reflectivity from an electron density profile in

term of a master equation where the ratio between the actual reflectivity $R(q)$ and that of an ideal sharp interface with the Fresnel reflectivity $R_F(q)$ is gives as:

$$\frac{R(q)}{R_F(q)} = \left| \int_{-\infty}^{\infty} \left(\frac{df}{dz}\right) e^{iqz} dz \right|^2 . \qquad (3.2.10)$$

Here $f(z)$ describes the normalized electron density along the surface normal distance z into the material. A more intuitive picture can be provided by viewing the ratio as the Fourier transform of the electron density gradient. To visualize, Fig. 14 shows the electron density of four layers of Ph-BTBT-10 and the corresponding calculated reflectivity via Equ.3.2.10.

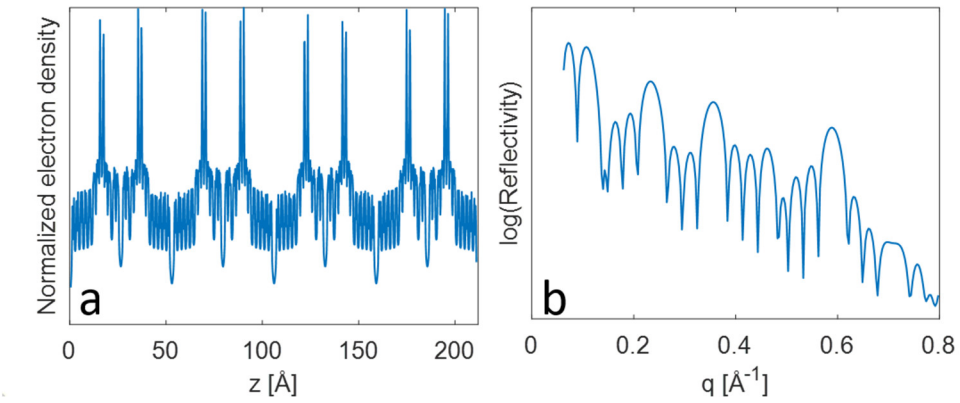

Figure 14: Normalized electron density of an example system of four layers of bulk Ph-BTBT-10 (a) and calculated reflectivity (b).

The modelling of an unknown electron density to measured reflectivity values is the basis of X-ray reflectometry. In contrast to the direct calculation of the reflectivity from one specific density the inverse problem cannot be solved unambiguously and is a complex problem. Several algorithms exist for both efficiently solving the Parratt system of equations for distinct multilayers[29,30] as well as for the master equation where one possible electron density profile is modelled[31,32].

4. Results

4.1 A Phase Transition Towards a Thermodynamically Less Stable Phase: Cross Nucleation due to Thin Film Growth of a Benzothieno-Benzothiophene Derivative

The following manuscript was submitted to *The Journal of Physical Chemistry C* in the present form. Main experimental work was done by Andreas Hofer in the group of Michael Ramsey. The material was synthesized by Alessandro Sanzone and Luca Beverina. Further data analysis and processing was done by the first author. Preparation and proof-reading of the manuscript was done by all authors.

A Phase Transition Towards a Thermodynamically Less Stable Phase: Cross Nucleation due to Thin Film Growth of a Benzothieno-Benzothiophene Derivative

Sebastian Hofer[a], Andreas Hofer[a], Josef Simbrunner[b], Michael Ramsey[c], Martin Sterrer[c], Alessandro Sanzone[d], Luca Beverina[d], Yves Geerts[e,f], Roland Resel[a]*

[a] *Institute of Solid State Physics, Graz University of Technology, 8010 Graz, Austria,*

[b] *Division of Neuroradiology, Vascular and Interventional Radiology, Medical University Graz, 8010 Graz, Austria*

[c] *Institute of Physics, Karl-Franzens University Graz, 8010 Graz, Austria*

[d] *Department of Materials Science, University of Milano-Bicocca, 20126 Milano, Italy*

[e] *Laboratoire de Chimie des Polymères, Faculté des Sciences, Université Libre de Bruxelles, 1050 Bruxells, Belgium*

[f] *International Solvay Institutes for Physics and Chemistry, Université Libre de Bruxelles (ULB), Boulevard du Triomphe, CP 231, 1050 Bruxelles, Belgium*

* roland.resel@tugraz.at

Abstract

The molecule 2-decyl-7-phenyl-[1]benzothieno[3,2-b][1]benzo-thiophene is an organic semiconductor, with outstanding properties in terms of molecular packing and its use in organic electronics. The asymmetric shape of the molecule causes a double layer crystal structure at room temperature. In this work we report its thin film growth by physical vapour deposition starting from the monolayer regime up to thick films. The films are studied in terms of their morphology, crystallographic properties and thermal stability by atomic force microscopy and X-ray diffraction methods. It is found that the known double layer crystal structure is formed at the initial thin film growth stage. After a thickness of one double layer, a transition into an unknown polymorph is observed which is of metastable character. The new phase represents a single layer phase, the crystal structure could be solved by a combination of X-ray diffraction and molecular dynamics simulations. The observed thin film growth is outstanding in terms of surface crystallisation: the formation of a metastable phase is not associated with the initial thin film growth, since the first growth stage represents the bulk crystal structure of this molecule. Its formation is associated to cross-nucleation of one polymorph by another which explains why a metastable phase can be formed on top of a thermodynamically more stable phase.

Introduction

Polymorphism in molecular crystals became an important issue, since application relevant properties depends highly on the type of phase [6,33]. The recent efforts of defined crystallisation within thin films reveals an additional source of polymorph phases due to the presence of a substrate surface during the crystallisation process [34,8]. Polymorphism with strong variation of molecular packing is possible, an important issue is the thermodynamic stability of the polymorph phases [7,35]. Thin film metastable phases appear for most of the well-studied organic electronic molecules like oligoacenes, oligothiophenes or benzothieno-benzothiophene based derivatives [36,37,38,39]. In some cases the metastable phase shows improved charge transport properties in comparison to the thermodynamic stable phase[8], e.g. in case of pentacene[40].

Metastable phases appear as a consequence of the growth kinetics: fast solidification processes together with weak non-directed interactions can cause changes in the molecular packing, improvable intermolecular arrangements, and restricted molecular conformation are possible[41,42]. Frequently, metastable phases appear as a result of a thin film deposition process[34]. Depending on the preparation method, the crystallisation process can be close to or far away from the thermodynamic equilibrium. On one hand, solution processing by drop casting leads rather to the equilibrium crystal structure if the solvent evaporation is slow. On the other hand, solution processing by quick solvent evaporation or even physical vapor deposition can result in crystalline phases far away from the thermodynamic equilibrium[35]. The presence of a surface during the crystallisation process plays an additional role, since the interplay between the intermolecular interaction and the molecule / substrate interaction are important parameters which determine the preferred crystallisation relative to the substrate surface[43,44]. The confinement of the molecular packing with the substrate surface can be the origin of specific polymorphs which is assigned to substrate-induced polymorphism[9,10].

The crystallisation process starts at the substrate surface. The molecular packing motifs within the initial crystal nuclei is a result of constraints determined by the substrate surface. The formed crystals do not necessarily induce a stable crystal structure for the entire film[45,37]. Generally, it is expected that a transition to the equilibrium bulk structure may take place for crystals sufficiently decoupled from the substrate surface[46]. However, metastable phases can be found also for thin films (e.g. of pentacene) with a nominal thickness of several hundred nm[47].

The present work represents a unique observation in that context. The known equilibrium bulk phase of the performing molecular semiconductor 2-decyl-7-phenyl[1]benzothieno[3,2-b][1]benzothiophene ($C_{30}H_{32}S_2$, abbreviated by Ph-BTBT-10) is formed directly at the substrate surface and subsequently an unknown metastable phase is formed at a later growth stage. This unprecedented effect of surface crystallisation has implications for the polymorphism of organic compounds at substrate surfaces.

The Molecule Ph-BTBT-10

The molecular semiconductor Ph-BTBT-10 is the focus of considerable attention as it shows excellent performance in thin film transistors[48,49]. The molecule is composed from a benzothieno-benzothiophene (BTBT) core with a phenyl ring at one terminal end of the BTBT core and with a decyl chain at the other terminal end. The molecule crystallizes in a layered structure with nano-segregation of the conjugated parts of the molecule from the decyl part[14]. The conjugated parts pack in a herringbone pattern, typical for rod-like conjugated molecular units[15]. Double layers are formed where two herringbone layers as well as two decyl layers are placed next to each other. The thickness of the double layer corresponds to the crystallographic (001) plane with an interplanar distance of 5.3 nm. The packing of the molecules within the bulk phase is depicted in Figure 1. The asymmetric nature of the molecule which is a composition of a rigid part and of a flexible part favours liquid crystalline states, the associated phase transitions are in discussion[17,18].

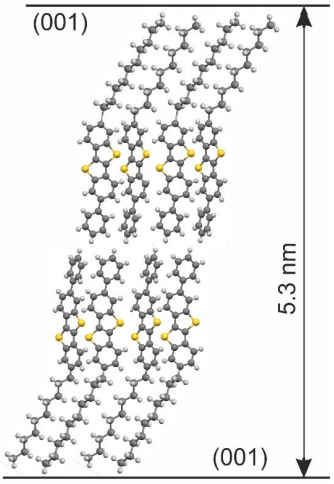

Figure 1: Packing of the molecules as a double layer structure present within the known bulk phase of the molecule Ph-BTBT-10. The crystallographic (001) planes are drawn and their interplanar distance is given.

Experimental methods

The molecule Ph-BTBT-10 was synthesized according to the strategy recently published[50]. The as-synthesised powder was purified via sublimation before use. Films with different thicknesses were deposited by physical vapor deposition onto 1 cm × 1 cm silicon substrates covered with a 150 nm thick layer of thermally grown silicon oxide. Substrates were chemically cleaned by isopropanol and acetone obtaining a surface energy of 49 mN/m with a polar part of 24 mN/m and a dispersive part of 25 mN/m (details are given in Fig. S1, Supporting Information). The substrates were inserted into a vacuum chamber and the molecule Ph-BTBT-10 was deposited from a Knudsen cell in a vacuum with a base pressure of about $2 * 10^{-8}$ mbar. Films with nominal thicknesses starting from sub monolayer coverages (1.5 nm) to a complete coverage of the substrate surface (6 nm) up to multilayer films with thicknesses of up to 80 nm were deposited. The nominal film thickness was determined during the deposition process using a quartz microbalance; the deposition rate was in the range of 1 nm/min.

The thin-film morphology was investigated via Atomic Force Microscopy (AFM). A Nanosurf Easycan 2 was used equipped with PPP-NCLR-50 silicon tips from Nanosensors. The investigations were performed in tapping mode, height images

as well as phase contrast images were taken. For AFM image analysis, the software Gwyddion was used[51].

X-ray reflectivity (XRR) was carried out with a PANalytical Empyrean reflectometer in θ - θ geometry using CuKα radiation. At the incident beam side, a parallel beam X-ray mirror was used for monochromatizating. At the diffracted beam side an anti-scatter slit as well as a 0.02 rad Soller slit were used together with a PIXcel3D detector operating as a point detector. Temperature dependent measurements were performed with a DHS 900 heating stage from Anton Paar Ltd. Graz[52]. The experiments were performed under nitrogen atmosphere. The data was converted into reciprocal space by the scattering vector q_z along the z-direction (perpendicular to the substrate surface) with $q_z = \frac{4\pi}{\lambda} sin\left(\frac{2\theta}{2}\right) = \frac{2\pi}{d_{hkl}}$ using λ as the wavelength of the primary X-ray beam, 2ϑ as the scattering angle and d_{hkl} as the interplanar distance of the (*hkl)* plane. XRR data of thick films (nominal thickness > 20 nm) were fitted with the software *X'Pert Reflectivity* (PANalytical) to obtain film thickness and average mass densities. XRR data of thin films (nominal thickness < 20 nm) were fitted with the software STOCHFIT to obtain the electron density distribution along the z-direction (perpendicular to the substrate surface) by a free model approach[32]. The results are scaled to the electron density of the amorphous silicon oxide layer which results in absolute values of the electron density of the organic layer[53].

Grazing incidence X-ray diffraction (GIXD) was carried out at the beamline XRD1 at Elettra Synchrotron Trieste with a wavelength of 1.4 Å using for the primary X-ray beam an incidence angle of α_i = 0.8° on a goniometer in Kappa geometry[54]. A PILATUS 2M detector was used to collect the diffracted intensity. To improve statistics, the sample was rotated during the measurement and the diffracted intensity was integrated over an exposure time of 30 s for a sample rotation of 60 degrees. Data from GIXD are presented as a function of the scattering vector *q*. The components of the scattering vector are determined for each detector pixel from the incident angle α_i and from the outgoing angle α_f in the sample coordinate system together with a calibration measurement on a LaB_6 film. Finally, reciprocal

space maps are drawn as a function of the q_z (component chosen perpendicular to the substrate surface) and of the q_{xy} (component chosen parallel to the substrate surface). The data was evaluated with the use of the in-house developed software package GIDVis[55]. The resulting reciprocal space maps are corrected based on geometrical correction factors, i.e. Lorentz and polarisation factors.

Determination of the molecular packing within the polymorphic phase was performed by an experimental / computational approach. In a first step the lattice constants were determined by indexing of the GIXD pattern using a recently developed indexing routine[56]. The crystallographic unit cell was used as input for Molecular Dynamics (MD) simulation for a determination of the molecular packing. These simulations were carried out with the LAMMPS software package[57] using the CHARMM general force field version 3.0.1[58]. Several thousand trial structures are generated, by placing randomly oriented molecules in an expanded unit cell (140%). During the simulation run the starting configuration was relaxed and reduced to the experimentally determined unit cell size. Resulting structures are clustered based on their packing motif and their energy. Final assignment of the obtained molecular packing to a crystallographic structure was performed on the basis of a comparison of the calculated structure factors of the Bragg peaks with the experimental intensities from the GIXD measurements.

Results

In a first step the morphology of the films was investigated by atomic force microscopy. The corresponding AFM micrographs are depicted in Figure 2, characteristic morphologies of sub-monolayer films with a nominal coverage of 3.0 nm, to a complete coverage of the substrate surface (6 nm) up to thick films with a thickness of 60 nm are shown.

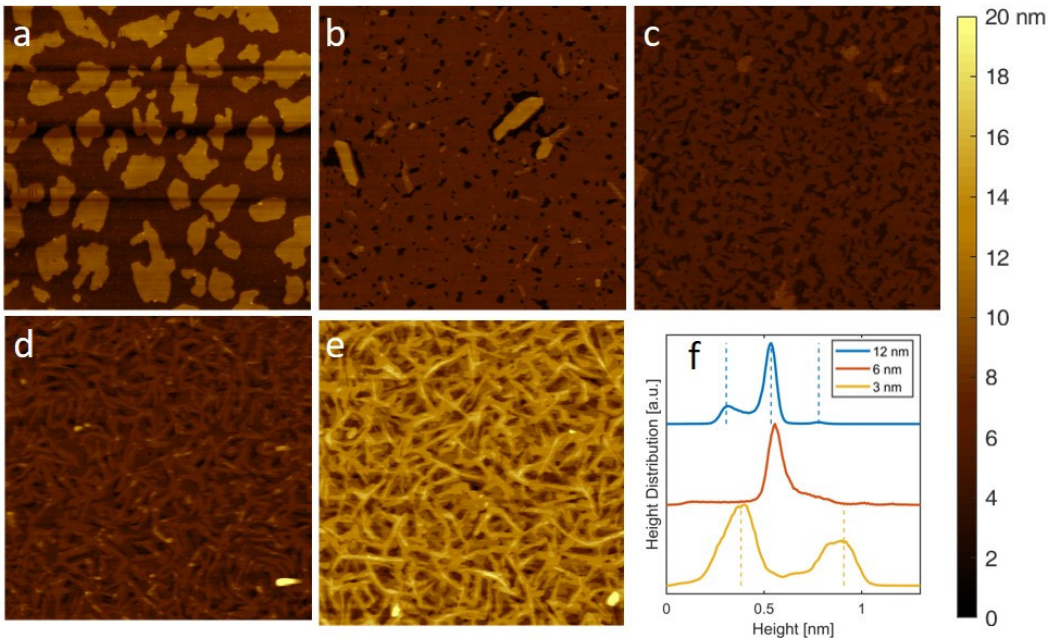

Fig.2: Atomic force micrographs (scan size 10 µm x 10 µm) of thin films of the molecule Ph-BTBT-10 deposited by physical vapour deposition with nominal film thicknesses of 3.0 nm (a), 6.0 nm (b), 12.0 nm (c), 20 nm (d) and 60 nm (e) as well as height distributions for films with thicknesses from 3 nm, 6 nm and 12 nm with dashed lines indicating step heights of 5.2 nm or 2.5 nm (f).

The first growth morphology are individual islands with a characteristic lateral size in the range of about 1 µm (Fig. 2a). The characteristic height of these islands is determined by line scans, a value of 5.2 nm is found (Supporting Information, Fig. S2). The height distribution function reveals an average height of the islands at 5.2 nm and a coverage of the substrate surface of about 42% (Fig. 2f) These results of the AFM studies agree with the nominal film thickness determined by the quartz microbalance during the deposition process.

With increasing film thickness, the islands coalesce and films with a closed layer appear (Fig. 2b). However, the film is not completely homogenous due to the presence of open pores. The typical height differences between the closed layer and the substrate surface (depth of the pores) are barely visible in the height distribution functions (Fig. 2f) but clearly observable by line scans, a typical value of 4.4 nm is found (Fig. S2). At a nominal film thickness of 12 nm a continuous layer

is formed with a large number of pores together with few islands on top (Fig. 2c). However, the height distribution function reveals levels of 2.5 nm which could be unambiguously assigned to the pore depth and island heights (Fig. 2f, Fig. S2).

On further deposition of thicker films, the morphology change significantly, at a thickness of 20 nm, elongated structures appear with ridge like character (Fig. 2d). This morphology is more pronounced at larger film thicknesses (60 nm) with highly branched ridges (Fig. 2e). No further change in the morphology is observed for films up to a thickness of 80 nm.

The characteristic heights observed in the AFM studies can be compared with unit cell dimensions of the crystallographic structure. The island height of the first growth stage with 5.2 nm is close to the interplanar distance of the (001) plane (d_{001} = 5.304 nm). We conclude that the initial growth stage represents a double layer structure as it is the case for the known crystallographic phase (compare Fig. 1). However, the change of the growth stage at a film thickness of between 6 nm and 12 nm is accompanied with a terrace height of 2.5 nm. This represents rather a single layer structure. In both cases the molecules are aligned with their long molecular axes perpendicular to the layer, i.e. perpendicular to the substrate surface. Please note, that the variation of the layer thickness depends on the exact tilt angle of the molecules within the layer as well as on the conformation of the molecules, i.e. the angle between the aromatic part and the alkyl part of the molecule.

Area integrated information about the thin film morphology together with crystallographic information is obtained by X-ray reflectivity. The results on a sample series starting with a nominal thickness of 3 nm up to thick films with a thickness of 80 nm are depicted in Figure 3. In all cases Kiessig fringes are clearly visible which reveal the presence of homogenous layers: Samples with higher coverages (larger than 20 nm) show additional Bragg peaks revealing the crystallographic order in the deposited films.

In a first step the initial thin film formation is discussed. Films with a nominal thickness of 1.5 nm, 3 nm, 5 nm and 6 nm are investigated and fitted in terms of layer thickness and average mass densities (Supporting Information, Tab. S1). Thicknesses between 5.4 nm and 5.6 nm are obtained, which reveal that a double layer structure is formed at the substrate surface. The electron density distribution is calculated for the film with a closed double layer, the corresponding fit is shown in the Supporting Information Fig. S3. The electron density distribution along the z-direction of the 6 nm film (Fig. 4) reveals the internal structure of the double layer. The difference in the total electron densities of the decyl side chains and of the conjugated parts of the molecule make a determination possible[59]. It is found that the two aromatic parts of the molecule points towards each other and the outer regions of the double layer are formed by the decyl chains. Please note, that another molecular packing within the double layer would be theoretically possible where the decyl chains form the central part.

In a next step the X-ray reflectivity curves of films with intermediate film thickness are considered. The electron density distributions cannot be explained by a double layer arrangement of the molecules, the variation of the electron density follows rather a single layer structure (Fig. 4). Three layers are found for the 9 nm film and four layers for the 12 nm film. The obtained repeating distance of the layer is in between 2.3 and 2.7 nm. The low number of repeating planes does not allow to observe the defined stacking of single layers by a Bragg peak. The superposition of Bragg diffraction and Kiessig fringes from X-ray reflectivity does not allow a clear assignment of an observed intensity maximum to a defined interplanar distance[60]. However, starting at film thicknesses of 20 nm defined Bragg peaks appear at q_z = 2.37 nm^{-1}, together with higher order reflections at q_z = 4.71 nm^{-1} and q_z = 7.07 nm^{-1} arising from a crystallographic net planes with an interplanar distance of 2.64 nm.

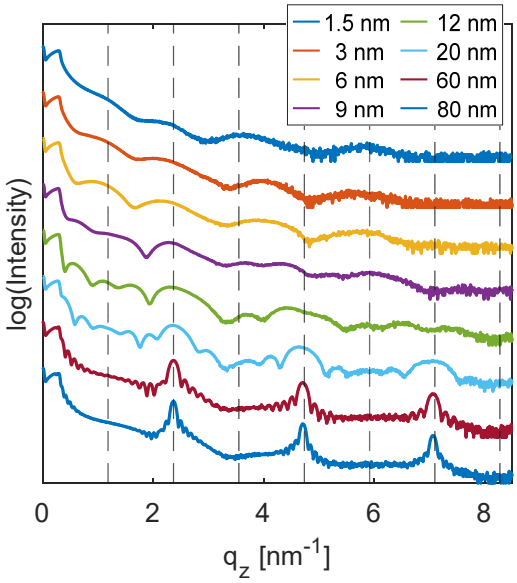

Figure 3: Specular X-ray reflectivity curves of thin film with varying nominal thickness. Vertical dotted lines indicate peak positions of the 00L diffraction peaks calculated on basis of the known crystallographic bulk of Ph-BTBT-10.

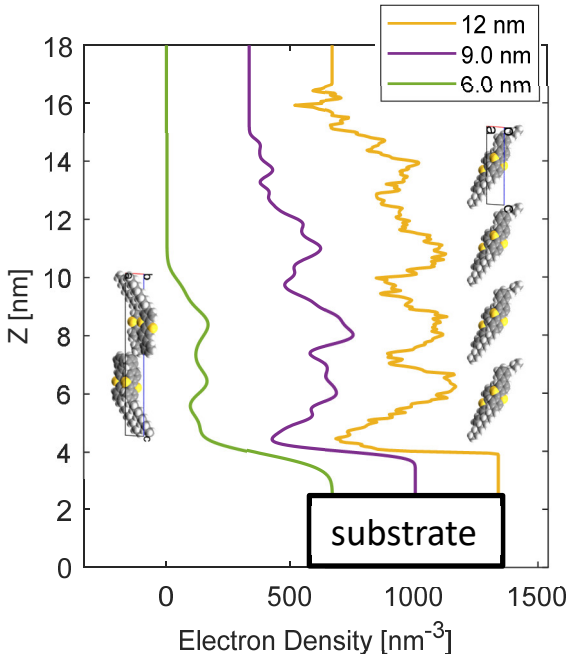

Figure 4: The z - dependence (perpendicular to the substrate) of the electron density of three selected X-ray reflectivity curves with nominal thicknesses of 6 nm, 9 nm and 12 nm, the curves are shifted for clarity. The electron density of the substrate is set to the value of 670 nm^{-3} for SiO_2[61]. The molecules are drawn in scale with their respective orientation relative to the substrate.

The presence of diffraction peaks reveals a crystalline state of the molecule Ph-BTBT-10. The width of the Bragg peaks reveals the z - height (perpendicular to the substrate surface) of the crystallites. The height of the crystallites is in good agreement with the nominal film thickness, the values are given in the Supporting Information, Tab. S1. Defined Laue fringes are observed around the Bragg peaks, revealing the homogeneity of the crystal height; the defined Kiessig fringes at low q_z values (0.3 nm^{-1} … 1 nm^{-1}) reveal the homogeneity of the overall film.

The observed peak positions cannot be explained by the known bulk phase of the molecule Ph-BTBT-10. The expected 00L peak positions of the bulk phase are shown by vertical dashed lines in Figure 3 arising from an interplanar distance of 5.30 nm. But we observe a crystal structure with an interplanar distance of 2.64 nm. In contrast to the double layer structure of Ph-BTBT-10 present in the known bulk phase, a new phase is found which represents a crystallographic structure composed of single layers. This phase is denoted in the following text as a “thin-film phase”.

To study the thermodynamic stability of this unknown phase, XRR investigations are performed as a function of temperature. A sample with a nominal thickness of 80 nm is heated with a rate of 1°C/min, while recording the diffraction signal. Figure 5 shows X-ray diffraction curves in a waterfall plot.

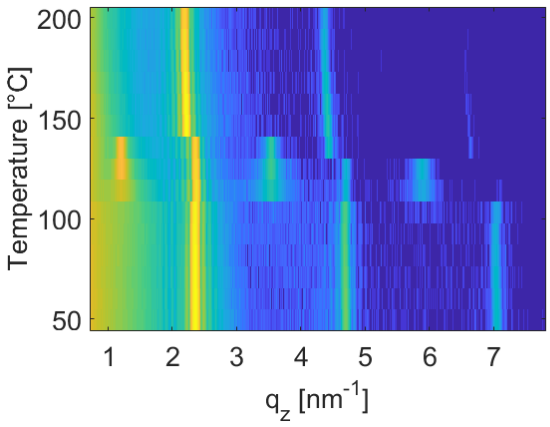

Figure 5: In-situ temperature dependent X-ray reflectivity measurements of a Ph–BTBT–10 thin film with a nominal film thickness of 80 nm in a waterfall plot.

At low temperatures three diffraction peaks are observed which are at the characteristic peak positions of the thin-film phase representing a single layer structure (see above). At a temperature of 115°C a phase transition happens. The appearance of a diffraction peak at q_z = 1.18 nm^{-1} together with higher order reflections represents the characteristic fingerprint of the double layer structure (bulk phase). Please note that the bulk phase is reported to be the thermodynamic stable phase of the molecule Ph-BTBT-10 with stability up to 143°C [48], at that temperature a transition to a liquid crystalline state is confirmed. In our measurements this transition is observed at a temperature of 146°C. Again, a single layer structure appears. Based on the exact peak positions, these phases can be assigned to a *crystal smectic E* phase of the molecule Ph-BTBT-10[62]. This phase is stable in a temperature regime up to 210°C[48]. The diffraction pattern of the thin-film phase and the *crystal smectic E* phase shows strong similarities, but a small and significant shift in the peak position is noticeable which reveal that separate phases of Ph-BTBT-10 are present.

To study the crystallographic structure of the thin-film phase, GIXD investigations were performed. Figure 6 shows the reciprocal space map for a film with a thickness of 60 nm. A large number of diffraction peaks are visible indicating a high degree of crystallographic order. The diffraction pattern was indexed including the Bragg peak observed in the specular diffraction experiment (Fig. 3)[56]. A crystallographic unit cell with lattice constants of a = 0.600 nm, b = 0.786 nm, c = 2.673 nm α = 90°, β = 93.24° and γ = 90° was found. The calculated peak positions are given by the centre of the circles within Fig. 6. Assuming that the unit cell accommodates two molecules results in a mass density of 1.212 gcm^{-3}. Based on the crystallographic unit cell, the diffraction peaks of the specular diffraction measurements could be assigned to Laue indices 00L (Fig.3).

The molecular packing within the crystal structure was determined by Molecular Dynamics simulations, the geometry of the crystallographic unit cell is used as an input parameter. The finally selected crystal structure explains the strongest intensities of our GIXD pattern reasonably well. The main diffraction peaks are

along q_{xy} = 13.2 nm^{-1}, 16.0 nm^{-1} and 19.1 nm^{-1}, this arrangement is a fingerprint for herringbone packing of the aromatic units of the molecules[37]. Additionally, the alternating peak intensities along q_{xy} (e.g. 112, -113, 113, -114) reveal that even fine details of the molecular packing are explained reasonably well.

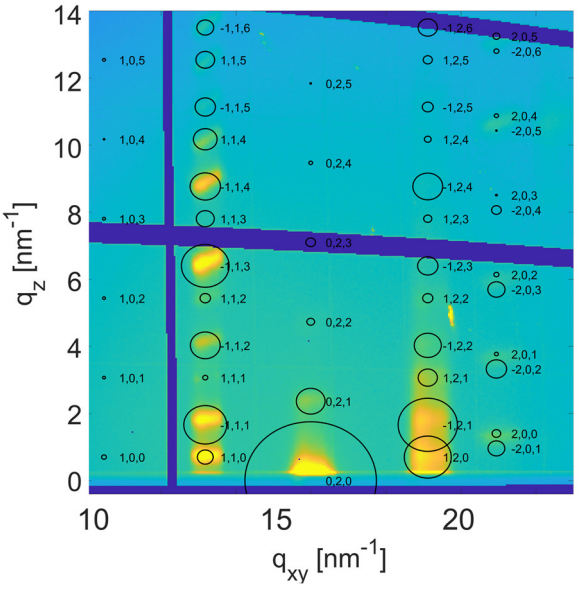

Figure 6: Reciprocal space maps of a thin film with a thickness of 60 nm, intensities are plotted in logarithmic scale. Peak positions are based on the crystallographic unit cell of the thin-film phase; the area of the circles is proportional to the structure factor of the diffraction peaks.

The packing of the molecules within the crystal structure is depicted in Fig. 7. We found that two molecules represent the asymmetric unit, both molecules are antiparallel to each other. The BTBT cores are in herringbone arrangement with a herringbone angel of 34.6°. Moreover, it is important to mention that the terminal ends of the molecules (alkyl chains on one side and phenyl rings at the other side) do not form a continuous plane. This means the individual (single) layers within the crystal structure are not fully separated from each other, a minor interdigitation of neighbouring layers is observed within the crystal structure of the thin-film phase.

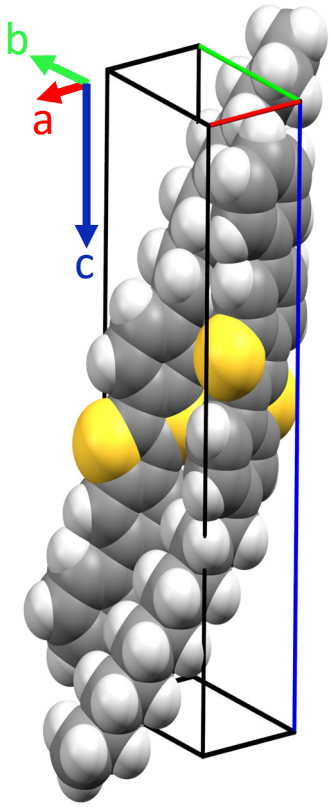

Figure 7: Molecular packing of Ph-BTBT-10 molecules within the thin-film phase, representing a single layer structure with antiparallel molecules.

In a final step, we discuss the GIXD data of films as a function of film thickness. Figure 8 presents the intensity distribution as a function of q_z at fixed q_{xy} = 13.2 nm^{-1}. This particular direction is chosen, since the diffraction pattern of the two crystal structures of Ph-BTBT-10 show clear differences along this particular ±11L Bragg peak series. The calculated diffraction patterns of both phases (of the bulk phase and of the thin-film phase) are plotted by bars. For the thin-film phase strong diffraction peaks are expected at 1.77 nm^{-1}, 4.16 nm^{-1} and 6.51 nm^{-1}. The experimental result on the 20 nm and 60 nm film are plotted and good agreement is found. For the bulk crystal structure strong diffraction peaks are expected at 3.04 nm^{-1} and 6.60 nm^{-1}. A comparison is possible with the diffraction features of a thick Ph-BTBT-10 film obtained by solution processing [62,63] and with the 6 nm thin film prepared. In both cases excellent agreement is found in terms of peak position as well as in terms of peak intensities. This result reveals that the crystal structure of the bulk phase is present in the sample where a double layer is formed directly at the substrate surface.

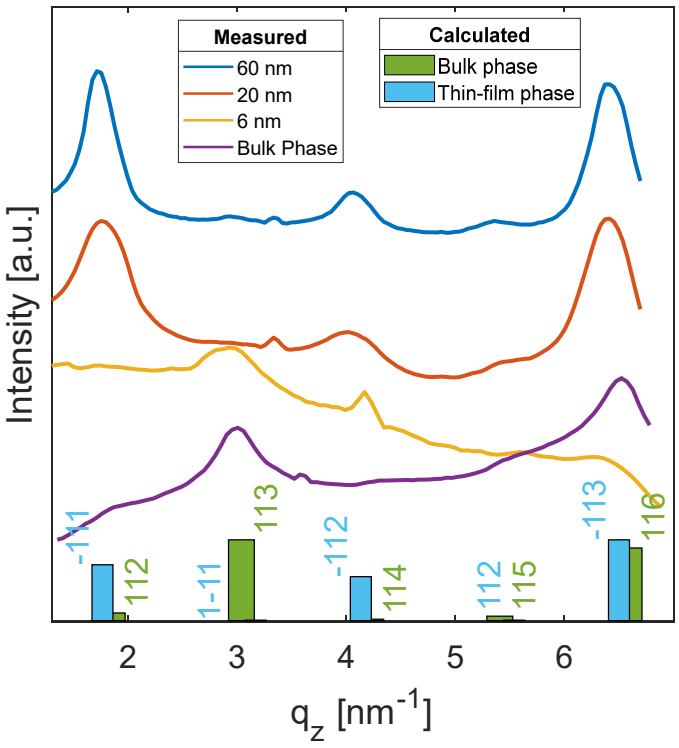

Figure 8: Intensity of diffraction peaks along the 11L Bragg-rod (qxy = 13.2 nm-1) for films of different thicknesses. Bars give calculated peak positions and peak intensities for the thin-film phase and of the bulk phase.

Interestingly, the resulting electron density fits (Fig. 4) hint that a re-arrangement towards a single layer structure appears, when thicker films are grown. This might be because the molecules don't have time to arrange themselves into their energetically more favourable double layer bulk packing before another layer is deposited onto them, thereby stabilizing the single layer structure. Whether this really happens already in the first layer or if a fully covered double layer needs to be present to support the thin film structure formation cannot be definitely answered at this point.

Discussion

The thin film growth of organic materials is important for fundamental understanding of the crystallization process at surfaces, but also more broadly for the polymorphism of organic compounds, which is essential for applications. Specific morphologies as well as new polymorph phases can appear. This work presents a thin film growth study of an asymmetric molecule consisting of two segments: a conjugated part on one side and a decyl part on the other side. AFM studies reveal a double layer structure at the initial thin films formation (up to a film thickness of 6 nm) and a transition to a single layer structure at larger thicknesses. This microscopic observation could be confirmed by X-ray reflectivity and grazing incidence X-ray diffraction. It is shown that the molecular packing within the initial film growth represents the known crystal structure of the bulk phase while an unknown new phase is formed at larger film thickness. The new phase – denoted as thin-film phase – is a single layer structure with a different molecular packing in comparison to the known bulk phase. While the bulk phase represents a double layer structure with head-to-head arrangement of the molecules, the thin-film phase is a single layer structure with antiparallel molecules. A transition from the thin-film phase to the bulk phase is possible as a diffusionless transformation, since both phases are composed by molecules with antiparallel orientations. The observation of this transition at a temperature of 120°C reveals that the thin-film phase is in a metastable state.

Theoretical investigations of the molecular packing are based on the transitions from double layer structures (as present in the bulk phase) to single layer structures[17,18]. Two different types of single layer structures are predicted. One of the predicted single layer structures is represented by separation of the conjugated parts from the decyl parts (so called nano-segregation) showing strong interdigitation of the decyl chains from neighbouring layers. This structure is found in the *crystal smectic E* phase at temperatures above 143°C[62]. The second predicted single layer structure is a mixed layer system with antiparallel molecules. This type of structure is found in the work presented here. All three

cases – the bulk phase as well as the two nanosegregated phases – show herringbone arrangement of the conjugated units of the molecule.

An outstanding observation is that the known bulk phase is formed at the initial growth stage, a double layer structure with a thickness of about 5.5 nm is formed. The molecules are in a head-to-head arrangement, so that the conjugated parts are located at the centre of the double layer and the decyl chains forming the outer regions (Fig.1). XRR as well as GIXD investigations reveal that this double layer structure shows the same molecular packing as known from the crystallographic structure of the bulk phase. In a subsequent step a new phase appears which is in a metastable state. This observation is reversed in comparison to other known examples of thickness induced polymorphism in organic films. Normally, metastable phases are formed at the initial growth stage directly at the substrate surface and a transition to stable bulk phases appears at later growth stages[64,65,37].

The effect observed here – the nucleation of a new polymorph by another one - can be understood in relation to cross-nucleation. A phenomenon encountered in the melt growth of polymers [66,67] but also for molecular crystals [68,69]. New polymorphs form in the case that the new polymorph grows faster than the initial one, independent on their thermodynamic stability [68,70]. Crystallisation of molecules by physical vapour deposition involves different processes like adsorption and migration of single molecules at surfaces and changes of the orientation and conformation of the molecules due to crystallisation. For our situation two distinct situation are present for the orientation of the molecules: the double layer structure (located directly at the substrate surface) consists of two separated layers with either head-down and head-up orientation. While the metastable thin-film phase possesses both orientations of the molecules combined in a single layer. This means that the crystallisation kinetics may differ fundamentally for both types of crystal structures.

A further role may play confinement of the molecular packing with the substrate surface[37,10]. In our case the double layers of the bulk phase exhibit the possibility

of surface confinement, while the molecular packing within the thin-film phase requires interdigitation of the neighbouring decyl layers. The initial 5.5 nm layer represents a soft matter surface which can compensate the interdigitation while a hard matter surface (e.g. silicon oxide) does not provide any flexibility.

Conclusion

Thin-films of Ph-BTBT-10 were grown via physical vapour deposition onto silicon substrates. The film thickness was varied between 1.5 nm and 80 nm. In the regime up to 6 nm the film morphology and diffraction data indicates the growth of the well-known bulk structure of the molecule, while thicker films begin exhibiting a new polymorphic phase. An unknown phase is found by indexing of GIXD patterns, which is used in a subsequent step to solve the structure with a computational approach. Although quite similar in peak position, the bulk phase and the thin-film phase, clearly differ in their peak intensities which reflects the strong difference in the molecular packing. While the bulk phase shows a double layer structure with head-to-head arrangement of the molecules and nano-segregation of the conjugated core and the decyl chains, the thin-film phase shows a single layer system where aliphatic and aromatic residues are intertwined. It is found that the thin-film phase is stable up to a temperature of 120°C where a transition to the bulk phase appears. The outstanding observation of this work is that the thermodynamically more stable bulk phase represents the initial growth state of the thin film and that the metastable phase is formed at a later growth stage. These results are assigned to cross-nucleation, since a change of polymorph phase appears after nucleation during the thin film growth process

The surface energy of the used oxidised silicon substrates was determined by contact angle measurements. The total surface energies γ_L of four different solvents (diiodomethane, benzyl alcohol, glycerole and water) are used together with their separated polar and dispersive parts γ_L^p and γ_L^d, respectively. Figure S1 shows the experimental data plotted by the method by Owens and Wendt[71]; the polar and dispersive component of the surface energy was determined from the linear regression.

Figure S2 gives atomic force microscopy images of thin films in the thickness regime with nominal coverages of 3 nm, 6 nm and 12 nm, respectively. Height profiles are given along selected lines.

Figure S3 gives the respective fits of the X-ray reflectivity curves for the determination of the electron density distribution across thin films as depicted in Figure 4. The fits are performed with the software STOCHFIT[32].

Table S1 gives numerical values of layer thickness and average mass density of films with a nominal thickness in the range from 1.5 nm up to 12 nm obtained by X-ray reflectivity fits with a single layer model using the software *X'Pert Reflectivity* (PANalytical). The vertical crystal size is obtained by analysing the Laue fringes (peak broadening) for films in the thickness range from 20 nm to 80 nm.

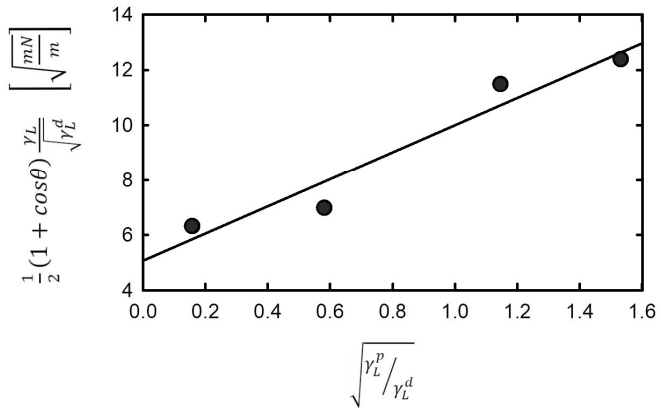

Figure S1: Contact angle θ plotted by the method of Ownes and Wendt together with a linear regression for the determination of the surface energy of the used silicon oxide surfaces.

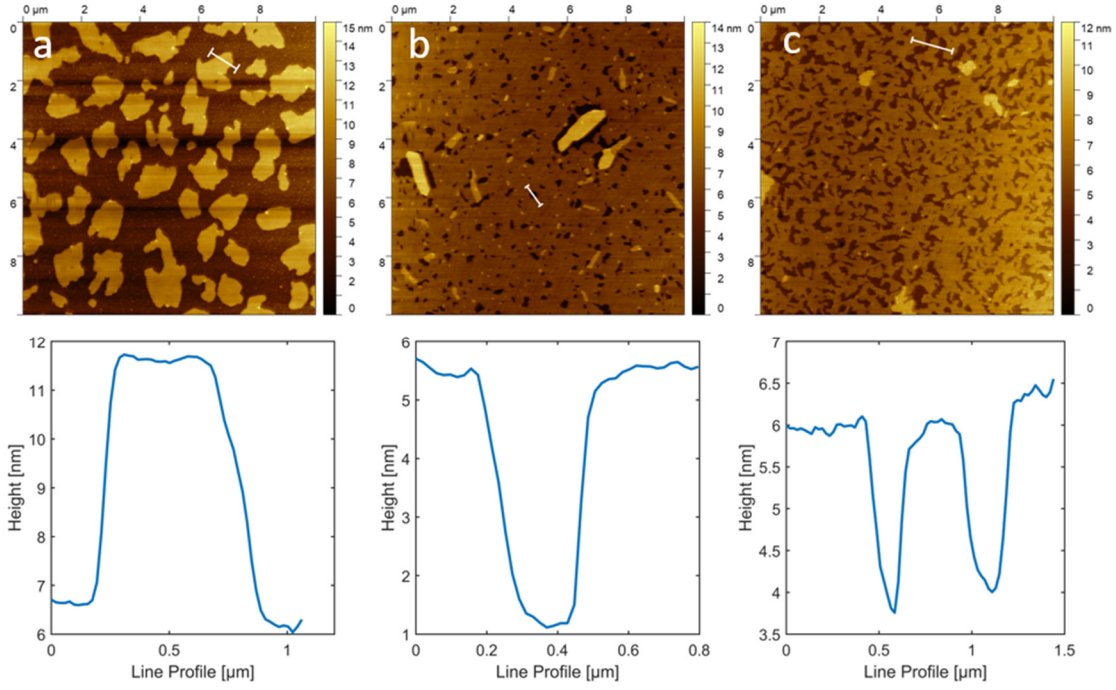

Figure S2: Atomic force microscopy micrographs with a (scan size 10 µm x 10 µm) of thin films of the molecule Ph-BTBT-10 deposited by physical vapour deposition with nominal film thicknesses of 3.0 nm (a), 6.0 nm (b) and 12.0 nm (c) with height profiles along marked lines.

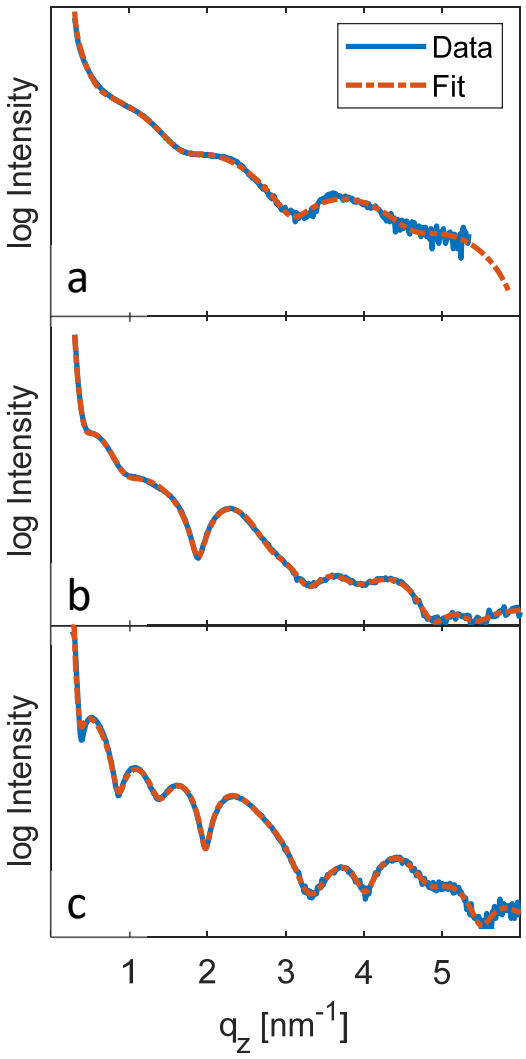

Figure S3: X-ray reflectivity data and resulting fits based on the electron density distribution by a free model approach for films with a nominal thickness of 6.0 nm, 9.0 nm and 12 nm (a-c)

Table S1: Thin film morphology (film thickness and mass density converted from the average electron density) of films in the thickness range from 1.5 nm to 12 nm as determined by fits of the X-ray reflectivity curves. Vertical size of the crystallites obtained from the Laue fringes of the Bragg peak at q_z = 2.38 nm^{-1}.

nominal thickness [nm]	thickness [nm]	mass density [g/cm^3]	vertical size [nm]
1.5	5.5	0.36	
3.0	5.7	0.64	
5.0	5.6	0.79	
6.0	5.6	0.74	
9.0	8.4	0.80	
12	11.4	1.06	
20			20
60			50
80			78

Associated content

Accession Codes

CCDC 2097887 contains the supplementary crystallographic data for this paper. These data can be obtainedfree of charge ia www.ccdc.cam.ac.uk/data_request/cif, or by emailing data_request@ccdc.cam.ac.uk, or by contacting The Cambridge Crystallographic Data Centre, 12 Union Road,Cambridge CB2 1EZ, UK; fax: +44 1223 336033.

Author information

Corresponding Author

Roland Resel - *Institute of Solid State Physics, Graz University of Technology, 8010 Graz, Austria; orcid.org/0000-0003-0079-3525*

Authors

Sebastian Hofer - *Institute of Solid State Physics, Graz University of Technology, 8010 Graz, Austria; orcid.org/0000-0002-8958-6815*

Andreas Hofer - *Institute of Solid State Physics, Graz University of Technology, 8010 Graz, Austria*

Josef Simbrunner - *Division of Neuroradiology, Vascular and Interventional Radiology, Medical University, Graz, 8010 Graz, Austria; orchid.org/0000-0002-7207-9622*

Michael Ramsey - *Institute of Physics, Karl-Franzens University Graz, 8010 Graz, Austria;*

Martin Sterrer - *Institute of Physics, Karl-Franzens University Graz, 8010 Graz, Austria; orcid.org/0000-0001-9089-9061*

Alessandro Sanzone - *Department of Materials Science, University of Milano-Bicocca, 20126 Milano, Italy*

Luca Beverina - *Department of Materials Science, University of Milano-Bicocca, 20126 Milano, Italy; orchid.org/0000-0002-6450-545X*

Yves Geerts - *Laboratoire de Chimie des Polymères, Faculté des Sciences, Université Libre de Bruxelles, 1050 Bruxells, Belgium; International Solvay Institutes for Physics and Chemistry, Université Libre de Bruxelles (ULB), Boulevard du Triomphe, CP 231, 1050 Bruxelles, Belgium; orcid.org/0000-0002-2660-5767*

Notes

No potential conflict of interest was reported by the authors.

Acknowledgments

The work was supported by the Austrian Science Foundation (FWF) under the Grant P30222, by the Belgian National Fund for Scientific Research (FNRS) for financial support through research projects Pi-Fast n° T.0072.18, and 2Dto3D n° 30489208, by the French Community of Belgium (ARC n°. 20061), and by the European Union's Horizon 2020 research and innovation programme under the Marie Skłodowska-Curie grant agreement No 811284 (UHMob). The authors acknowledge the synchrotron Elettra, Trieste for allocation of synchrotron radiation and thank Luisa Barba and Nicola Demitri for assistance in using beamline XRD1.

4.2 Molecular Packing Analysis of the Crystal Smectic E Phase of a Benzothieno-benzothiophene Derivative by a Combined Experimental / Computational Approach

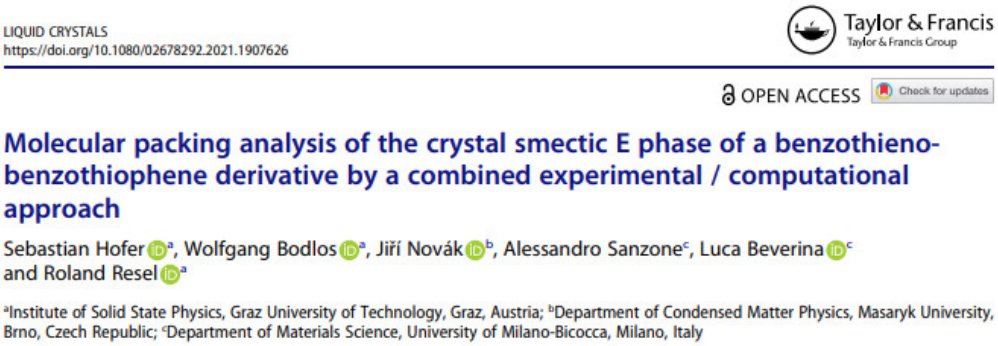
LIQUID CRYSTALS
https://doi.org/10.1080/02678292.2021.1907626

Taylor & Francis
Taylor & Francis Group

OPEN ACCESS Check for updates

Molecular packing analysis of the crystal smectic E phase of a benzothieno-benzothiophene derivative by a combined experimental / computational approach

Sebastian Hofer[a], Wolfgang Bodlos[a], Jiří Novák[b], Alessandro Sanzone[c], Luca Beverina[c] and Roland Resel[a]

[a]Institute of Solid State Physics, Graz University of Technology, Graz, Austria; [b]Department of Condensed Matter Physics, Masaryk University, Brno, Czech Republic; [c]Department of Materials Science, University of Milano-Bicocca, Milano, Italy

This work was carried out in collaboration with Jiří Novák, who provided the possibility of in-situ GIXD experiments. Sample preparation was carried out by Alessandro Sanzone under supervision of Luca Beverina. The measurements and the following data analysis, together with the computational study was performed by the first author. Preparation and proof-reading of the manuscript was done by all authors.

The article is available at: https://doi.org/10.1080/02678292.2021.1907626

Molecular Packing Analysis of the *Smectic E* Phase of a Benzothieno-benzothiophene Derivative by a Combined Experimental / Computational Approach

Sebastian Hofer[a]*, Wolfgang Bodlos[a], Jiří Novák[b], Alessandro Sanzone[c], Luca Beverina[c], Roland Resel[a]*

[a]*Institute of Solid State Physics, Graz University of Technology, Austria;* [b]*Department of Condensed Matter Physics, Masaryk University, Brno, Czech Republic,* [c]*Department of Materials Science, University of Milano-Bicocca, Milano, Italy*

* roland.resel@tugraz.at

* sebastian.hofer@tugraz.at

Molecular Packing Analysis of the *Crystal E* Phase of a Benzothieno-benzothiophene Derivative by a Combined Experimental / Computational Approach

Abstract

The molecule 2-decyl-7-phenyl[1]benzothieno[3,2-b][1]benzothiophene has gained a lot of attention, since high charge carrier mobility are observed in thin film transistors. The thermotropic liquid crystalline states may play an important role in the thin film formation, since the *smectic A* and the s*mectic E* phase (SmE) are claimed to be pre-stages of the final bulk structure. Structural characterisation of solution processed thin films are performed by specular X-ray diffraction and grazing incidence X-ray diffraction (GIXD) in the complete temperature range up to the isotropic state at 240°C. The GIXD pattern of the SmE phase is analysed in detail. Peak broadening analysis based on the paracrystalline model reveals that the crystallographic order across the smectic layers is larger than the order along the smectic layers. A combined experimental and computational approach is used to determine the molecular packing within the SmE phase. A number of different packing motifs are found which can be divided into i) alkyl / aromatic mixed layers and ii) two types of nano-segregation of the aromatic part from the alkyl chains with parallel stacking or herringbone packing of the aromatic units. Comparison of the calculated diffraction pattern with the experimental results reveals that nano-segregation is present within the SmE phase. Energy consideration clearly favours herringbone arrangement of the aromatic units. In summary, we found nano-segregation within the SmE phase of the molecule Ph-BTBT-10 with herringbone packing of the aromatic units and interdigidation of sidechains from neighbouring smectic layers.

Keywords: organic semiconductors, grazing incidence X-ray diffraction, thin films, crystal structure solution, crystal E, smectic E

Introduction

The class of alkyl substituted benzothienobenzothiophene type molecules gained a lot of attention due to high charge carrier mobilities in organic thin film transistors, values of up to 9 $cm^2V^{-1}s^{-1}$ are observed [72,73]. The presence of alkyl chains symmetrically attached at the terminal ends of the molecule provides overall flexibility in device fabrication, since thin films can be prepared by solution processing [74,59] as well as by physical vapour deposition [75,76]. Moreover, the thermotropic liquid crystalline state can be used in the thin film preparation procedure to obtain a defined structure within thin films [77,78].

Recently, a new asymmetric derivative of BTBT – the molecule 2-decyl-7-phenyl[1]benzothieno[3,2-b][1]benzothiophene (Ph-BTBT-10) - was introduced[48]. The asymmetry of this molecule with the aromatic part of the molecule (a phenyl ring and the BTBT unit) at one end and a decyl chain at the other end results in a more divers phase behaviour[79]. Liquid crystalline states with high structural order appear. It is reported that these states can be used as pre-stages of the final bulk crystallisation so that crystals with extended size can be prepared within thin films[80].

The asymmetry of the molecule causes crystallisation with a bilayer herringbone structure [48,79]. The structure is formed by stacking of individual layers built by herringbone layers formed by the aromatic units of the molecule and a decyl layer formed by the terminal alkyl chains. Two herringbone layers stack directly on top of each other so that double layer stacking of the herringbone layers appear. The crystal structure can be described by a sequence of double herringbone layers followed by double layers of the decyl chains. The lattice constants of this structure is $a = 6.047$ Å, $b = 7.757$ Å, $c = 53.12$ Å and $\beta = 93.14°$ where the lattice constant *c* span over two herringbone layers and two alkyl layers[81]. In summary the molecules show a *head-to-head* arrangement (along the c-axis), since the aromatic units of molecules from neighbouring herringbone layers are antiparallel to each other. A phase transition to a *smectic E* (SmE) with a *head-to-tail* arrangement of the molecules is observed at temperatures of 144°C[12,79]. A SmE

phase was concluded by polarized optical microscopy investigations[82]. Analysis of the molecular packing at elevated temperatures is performed by molecular dynamics simulations, a structure built by stacking of single molecular sheets in *head-to-tail* arrangement is obtained, however the arrangement of the molecules within the SmE phase is still unclear [16,17,18].

Recent developments in the field of crystal structure determination from thin films allow the determination of the molecular packing within unknown crystal structures exclusively present within thin films [37,36]. Grazing incidence X-ray diffraction in combination with specular X-ray diffraction is used. Despite the limited information of only few diffraction peaks, a combination of experimental performance and theoretical calculations can be suitable to determine the molecular packing[83]. Here we will apply our knowledge on the crystal structure solution from thin film to the SmE phase of the molecule Ph-BTBT-10.

Experimental

Thin film preparation

The molecule Ph-BTBT-10 was synthetized according to the strategy shown in Scheme 1 some of us recently published[50]. The commercially available [1]benzothieno[3,2-b][1]benzothiophene (BTBT) core was regioselectively acylated at the 2 position via a with a Friedel Crafts reaction with decanoyl chloride. The thus obtained ketone was converted in the 2-decyl-[1]benzothieno[3,2-b][1]benzothiophene (C10-BTBT) by reduction with a $NaBH_4/AlCl_3$ mixture in good yield. Bromination of the latter with bromine in chloroform afforded 2-decyl-7-bromo-[1]benzothieno[3,2-b][1]benzo-thiophene (Br-BTBT-10) after multiple chromatographic purification. Finally, a Suzuki-Miyaura coupling between Br-BTBT-10 and phenyl boronic acid in a Kolliphore EL 2 wt%: toluene emulsion (9:1 v/v) in the presence of triethyl amine as the base and [1,1'-Bis(di-tert-butylphosphino)ferrocene]dichloropalladium(II) $Pd(dtbpf)Cl_2$ as the catalyst gave 10-BTBT-Ph in essentially quantitative yield.

Thin film samples were prepared via spin-coating or drop-casting from toluene solutions of varying concentrations and spin speeds (0.2 g/l up to 5.0 g/l and 500 rpm up to 3000 rpm) onto thermally oxidised silicon wafers. Powder samples were prepared by transferring a small amount of about 1mg of polycrystalline material onto a silicon substrate and a subsequent flattening procedure.

Analytical methods

Specular X-ray diffraction was carried out with a PANalytical Empyrean diffractometer in θ-θ geometry using CuKα radiation. On the incident side a parallel beam X-ray mirror was used for monochromatisation. At the diffracted beam path an anti-scatter slit as well as a 0.02 rad Soller slit was used together with a PIXcel3D detector operating in either receiving 0D-mode or scanning 1D-mode. Temperature dependent in-situ measurements were performed with a DHS 900 heating stage from Anton Paar Ltd. Graz[52]. The experiments were performed under nitrogen atmosphere. The data are converted into reciprocal space by $q = \frac{4\pi}{\lambda} sin\left(\frac{2\theta}{2}\right) = \frac{2\pi}{d_{hkl}}$ with λ as the wavelength of the primary X-ray beam, 2θ the scattering angle and d_{hkl} the interplanar distance of the (*hkl)* plane. In case of a specular scan the total length of the scattering vector q has a contribution only in z-direction (perpendicular to the substrate surface).

Grazing incidence X-Ray diffraction (GIXD) at ambient temperatures was carried out at the beamline XRD1 at Elettra Synchrotron Trieste with a x-ray radiation wavelength of 1.4 Å using an incidence angle of α_i = 0.8° on a goniometer in Kappa geometry[54]. A PILATUS 2M detector was used to collect diffracted intensity. To improve statistics, the sample was rotated during measurement and 6 images with an exposure time of 30 s each were collected during one full sample rotation. Temperature dependent in-situ grazing incidence X-ray diffraction was performed using a Rigaku SmartLab 9 kW equipped with a Cu rotating anode, collimating parabolic multilayer mirror and pinhole optics. A HyPix 3000 2D detector was utilized for collecting GIXD measurements. Because of low signal a series of 40 images was measured for 1 hour each and summed up to improve the signal to

noise ratio. A DHS 1100 commercial high temperature stage from Anton Paar, covered by a carbon dome and filled with a nitrogen atmosphere was used during heating[84].

Data from GIXD are presented as reciprocal space maps with the out-of-plane (q_z) and in-plane component (q_{xy}) of the scattering vector q as an orthogonal basis, with the q_z component parallel to the surface normal and the q_x / q_y plane parallel to the substrate surface. The scattering vector components are determined for each detector pixel from the incident angle α_i and the outgoing angle α_f in the sample coordinate system and from a calibration measurement on an LaB_6 film, to determine additional parameters, e.g. the distance from the sample to the detector. Resulting data was evaluated with the use of the in-house developed software package GIDVis[55]. The resulting reciprocal space maps are corrected based on geometrical correction factors, i.e. Lorentz and polarisation factors.

For analysing the films in terms of paracrystallinity, the peaks were fitted with a Gaussian function in both in-plane (q_{xy}) and out-of-plane (q_z) direction. For the resulting peak widths Δq_{xy} and Δq_z a linear regression based on $(\Delta q)^2 = 4\left[\left(\frac{\pi}{D_{hkl}}\right)^2 + \left(\frac{\pi^3 g^2 m^2}{d_{hkl}}\right)^2\right]$ is calculated, where m and d_{hkl} denote the order of the diffraction peak in terms of its Laue index (*h, k* or *l*) and the inter-planar spacing of the diffraction peaks, respectively. This allows determining the crystallite size D_{hkl} and the amount of paracrystallinity *g* of the sample in two individual directions. No correction for the instrumental peak broadening was used.

Computational method

Determination of the molecular packing within the SmE phase was performed by an experimental / computational approach. In the first step the lattice constants were determined by indexing of the GIXD pattern. The crystallographic unit cell was used as an input for Molecular Dynamics (MD) simulation revealing the molecular packing. These simulations were carried out with the LAMMPS software package[57] using the CHARMM general force field version 3.0.1[58]. Several thousand

trial structures are generated, by placing two randomly oriented molecules in an expanded (120%) unit cell. During the simulation run the starting configuration was relaxed and reduced to experimentally determined unit cell size. The resulting structures are then clustered based on similarities of the packing motifs. Each selected packing motif appeared multiple times at the respective total energy. The obtained packing motifs are judged by a comparison of observed (F_{obs}) and calculated structure factors (F_{calc}) taken from the diffraction intensities on basis of a reliability factor $R = \frac{\sum||F_{obs}|-|F_{calc}||}{\sum|F_{obs}|}$.

Experimental results

A series of specular X-ray diffraction measurements were performed on a spin coated (5 g/l, 3000 rpm) film in the temperature range from room temperature up to 240°C. Figure 1a shows XRD scans at selected temperatures. At room temperature (25°C) a dominant peak series at $q_z = (0.118 * l)$ Å^{-1} (with *l* as the Laue index) is observed which can be assigned to the *00l* diffraction peaks of the bulk crystal phase of the molecule Ph-BTBT-10[81].

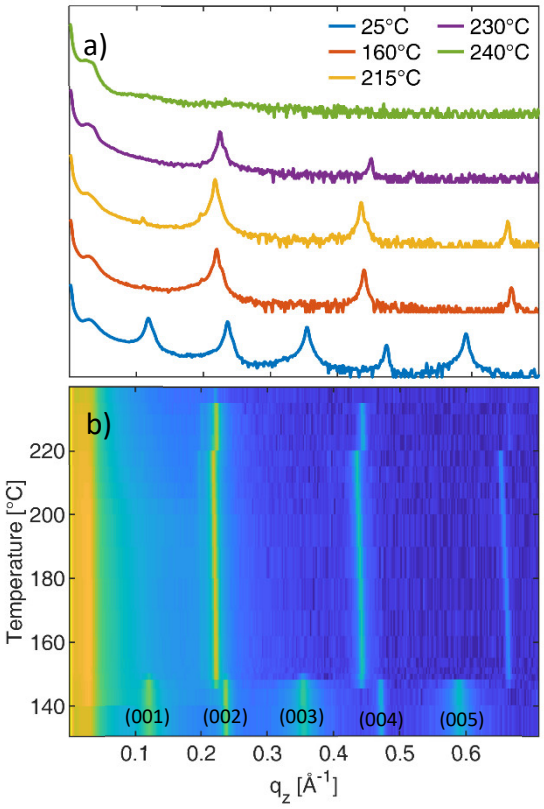

Figure 1: Specular X-ray diffraction of a Ph–BTBT–10 thin film as a function of temperature. Single scans of a film at selected temperatures (a) and a series of scans in the region between 120° and 240°C in a waterfall plot including the three phase transitions: bulk phase / SmE at a temperature of 149°C, SmE / SmA at 220°C and SmA / isotropic state at 235°C (b).

The interplanar distance of the *001* plane at 52.3 Å clearly reflects the bilayer structure of the known bulk phase. The absence of *hkl* reflections with $h \neq 0$ or $k \neq$

0 reveals a strong preferred orientation of the crystallites with the (001) plane parallel to the substrates surface. At a temperature of 149°C the peak sequence changes to $q_z = (0.216 * l)$ Å^{-1} which corresponds to the characteristic 00*l* peak series of the SmE phase with an interplanar distance of 29.1 Å of the (001) plane. With increasing temperature up to 215°C the peak position gradually shifts to lower q_z values due to thermal expansion. A sudden shift in the peak positions as well as in the peak intensities is observed at 220°C. This peak series is observed at q_z = (0.223 * *l*) Å^{-1} corresponding to an interplanar distance of 28.1 Å and is assigned to the *smectic A* (SmA) phase [48,82]. At 240°C, the diffraction peaks disappear which is assigned to a transition to the isotropic state. Figure 1b shows a waterfall plot of the specular diffraction pattern in the temperature range from 130°C to 240°C. Each scan was measured for 10 min at a fixed temperature which was increased in steps of 2°C in the vicinity of the phase transition temperature and in steps of 10°C at more remote temperature ranges. The phase transition temperatures between the bulk phase and the SmE phase is observed at 149°C, the transition to the SmA at 220°C and the final melting at 235°C. These phase transition temperatures are in quite good agreement with the literature [48,79].

The phase transition at the temperature of 149°C exhibits vanishing of odd-numbered (*00l*) peaks of the bulk phase and a shift of the leftover even-numbered peaks to smaller q-values. The doubling of peak distances in q-space indicates a reduction of the interplanar distance approximately by a factor of two which means that the bilayer structure changes to a single layer structure [17]. Please note, that the molecular layer thickness corresponds approximately to the length of a single molecule which means that a single molecular sheet is composed by upright standing molecules. Therefore, we can conclude that the SmE phase as well as the SmA phase are formed by single sheets which are stacked up on each other parallel to the substrate surface.

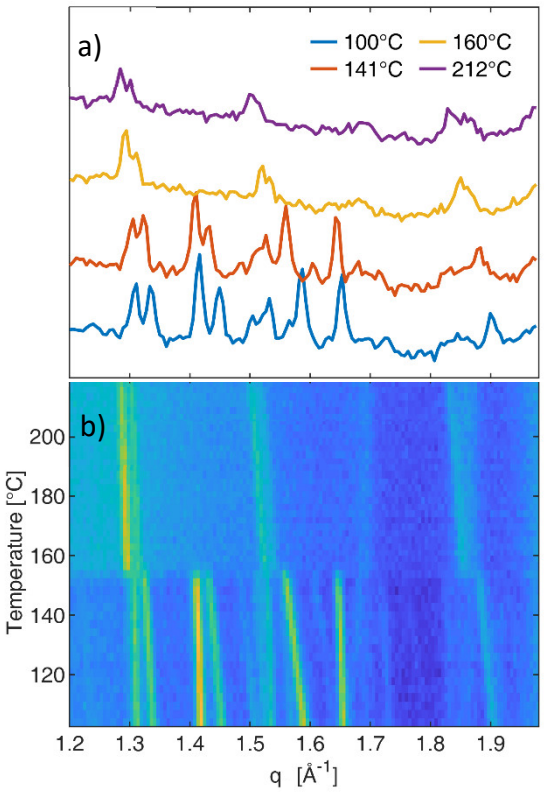

Figure 2: Selected powder diffraction scans at different temperatures (a) and the complete series of X-ray powder diffraction scans in the temperature region 100°C to 220 °C in a waterfall plot (b). The phase transition from the bulk phase to the SmE phase is around 153°C.

Figure 2 shows a series of diffraction patterns as a function of temperature measured on a powder sample at higher values of *q*. Selected diffraction pattern are depicted in Figure 2a, while a waterfall plot in a selected temperature range is given in Figure 2b. A clear phase transition is visible at 153°C, a temperature slightly larger than observed at thin films. A continuous shift of the peak pattern is visible also before and after the phase transition due to thermal expansion. To study the evolution of the lattice constants as a function of temperature, the exact peak positions of all observed peaks of the bulk phase (T < 153°C) were determined (namely *00l, 010, 011, 100, 101, 110, 111, 020, 021, 120, 012, 102, 112*). The lattice constants *a, b, c* and the monoclinic angle *ß* were determined as a function of temperature, the result is depicted in Figure 3. Within the bulk structure

(temperature range from 60°C to 153°C) the lattice constants *a* and *c* does not change significantly, but the lattice constant *b* increases and the monoclinic angle *ß* decreases.

The diffraction pattern at elevated temperatures (T > 153°C) are characteristic for a SmE phase with dominant peaks at 1.29 $Å^{-1}$, 1.52 $Å^{-1}$ and 1.85 $Å^{-1}$ [85,86]. The refinement of the unit cell parameters after the phase transition resulted in a monoclinic angle very close to 90°, independent of temperature. An orthorhombic unit cell was concluded, which is comparable to other SmE phases [87].

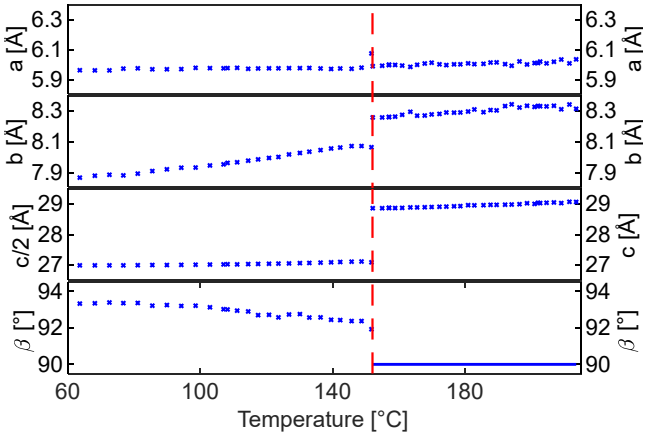

Figure 3: Lattice constants as a function of temperature of the bulk phase below a temperature of 153°C and of the smectic E phase between 153°C and 215°C. In case of the lattice constant c the half of the lattice constant (c/2) is plotted for the bulk phase, while for the SmE phase the full length (c) is plotted.

At the transition temperature of 153°C a clear shift in the lattice constants *b, c* and *ß* are observed, while a roughly continuous behaviour is observed for the lattice constant *a*. The volume of the crystallographic unit cell changes discontinuously from 2488.1 $Å^3$ (corresponding to 622 $Å^3$ per molecule) for the bulk crystal phase to 1462.0 $Å^3$ (731 $Å^3$ per molecule) for the SmE phase.

A more detailed crystallographic study was performed by GIXD. In the first step the bulk structure of Ph-BTBT-10 was investigated for a drop casted film at room temperature. Figure 4a presents an experimental diffraction pattern taken at room temperature, calculated peak positions are given by green spots and peak intensities by the area of the surrounding circles. The characteristic diffraction features of the bulk structure can be clearly identified as enhanced intensities along the *11l*, *02l* and *12l* rod. Moreover, characteristic packing features of the individual bulk structure of Ph-BTBT-10 can be identified by the enhanced intensities of the *112* and *115* peaks.

In a subsequent step the SmE phase was investigated by GIXD at a temperature of 160°C. A spin coated thin film from a 5 g/l solution was used. The corresponding result is shown in Figure 4b-d. A quite different diffraction pattern is observed in comparison to the bulk phase. Only few diffraction peaks are observed, they are arranged in two sequences at different q_{xy} values. Peaks along q_z = 0 (in-plane direction) reveal crystallographic order along the substrate surface, these peaks represent crystallographic order within a single smectic plane. The peak series at q_z ~ 0.22 Å^{-1} reveals onset of long range (positional) order perpendicular to the substrate surface (z-direction); these peaks reveal crystallographic order due to stacking of smectic planes. This diffraction pattern is in agreement with previous studies of SmE phases of other molecular materials: clear absence of peaks, corresponding to *10l* and *01l* peak series, six dominant peaks between at q = 1.3 Å^{-1} and 1.9 Å^{-1} (with Laue indices *110, 111, 020, 021, 120, 121*) [88]. Additionally, small intensities are found for the *200, 201* and *112* peaks (compare Fig. 4b-d). Indexing of the diffraction peaks is based on the results presented in Figure 3, following lattice constants of the orthorhombic unit cell are used at a temperature of 160°C: *a = 6.051 Å, b = 8.303 Å* and *c = 29.10 Å*.

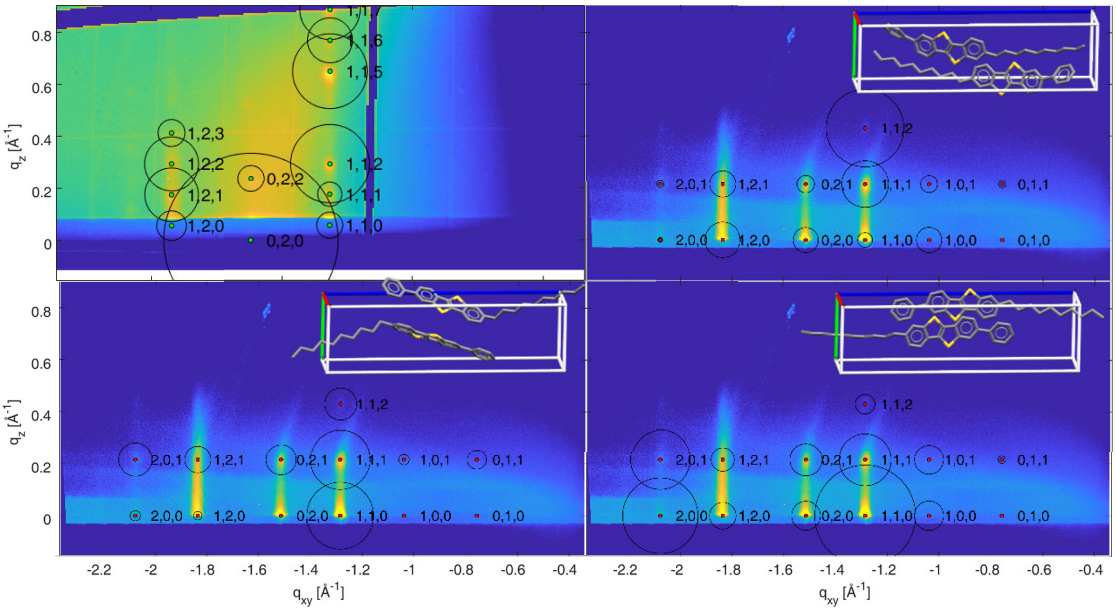

Figure 4: Grazing incidence X-ray diffraction pattern of Ph-BTBT-10 thin films at room temperature (a) and at a temperature of 160°C (b-d) with logarithmic scaling of the intensity. Additionally, calculated diffraction patterns are shown with points and circles representing positions and intensities of the calculated Bragg peaks, respectively. Different packing motifs are selected: the crystallographic bulk phase (a), Sm*E* with mixed layers (b), Sm*E* with nano-segregated layers with herringbone arrangement (c) and with stacked arrangement (d). The insets give the different packing motifs relative to the crystallographic unit cell.

The long-range order of the molecules within the SmE phase is far to be perfect, since only a limited number of peaks are observed. But in several cases a higher order diffraction peaks are observed, so that an analysis in terms of a paracrystalline model can be applied [89]. Figure 5 shows fits of the paracrystalline model for five families of diffraction peaks (*11l, 02l* and *20l, h20, 1k0*) in terms of their in-plane peak widths Δq_{xy} and out-of-plane peak widths Δq_z, respectively, with a summary of the fit parameters in Table 1. Although the number of data points is limited (two or three), the complete set of data gives a clear trend for the

two different directions. A crystallite size of about D_z = 100 Å and a paracrystallinity g =10% is found for the out-of plane direction while values D_{xy} = 50 Å and g= 4% is found for the in-plane direction. A g-value of smaller than 10% is classified as diffuse scattering from a disordered state [90].

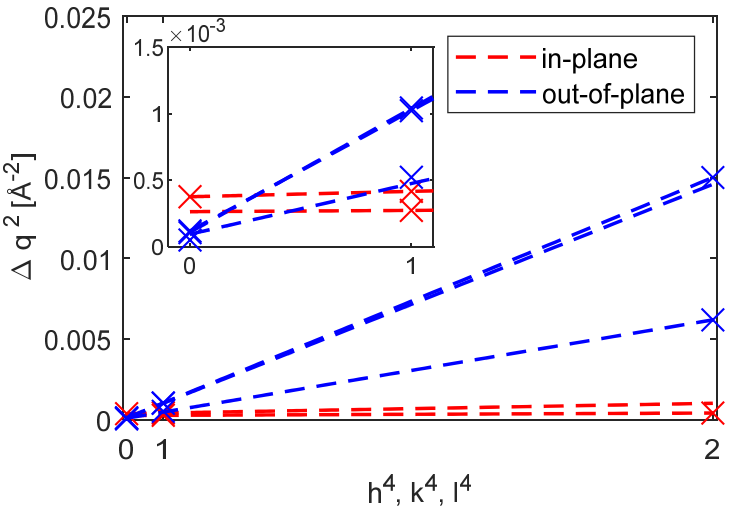

Figure 5: The square of in-plane peak width (Δq_{xy}^2) and of the out-of-plane peak width (Δq_z^2) plotted as a function of the fourth order of the Laue indices *h,k,l*. The linear regression is based on the paracrystalline model. The inset shows the range between *h,k,l* = 0 and *h,k,l* = 1.

Laue indices	D_z [Å]	D_{xy} [Å]	g_z [%]	g_{xy} [%]
1 1 l	96.7	-	12.3	-
0 2 l	103	-	9.01	-
2 0 l	91.8	-	11.2	-
h 2 0	-	51.5	-	5.6
1 k 0	-	61.5	-	3.5

Table 1: Crystallite sizes D_z and D_{xy} and degrees of paracrystallinity g_x and g_{xy} for five sets of diffraction peaks determined on basis of the paracrystalline model for the *smectic E* phase of Ph-BTBT-10. The respective values for the in-plane direction (along the smectic layers) and for the out-of-plane direction (across the smectic layers) are denoted by the superscripts *z* and *xy*, respectively.

In a next step the molecular packing within the SmE phase is analysed. The sudden change of the lattice constant *c* at the phase transition temperature from 54.2 Å for the bulk phase to 28.9 Å in the SmE phase (compare Fig.3) reflects the transition from a bilayer structure with *head-to-head* arrangement to a single layer structure with *head-to-tail* arrangement. The transition can happen by lateral and vertical displacements of the molecule by avoiding an energy demanding complete flip of the whole molecule [17,18]. As a consequence, the single sheet structure is formed by anti-parallel molecules where the aromatic parts of neighbouring molecules in one molecular sheet are alternatively oriented with alkyl chains pointing parallel and antiparallel to the c*-axis (perpendicular to the smectic layers).

The molecular dynamics simulations are based on the crystallographic unit cell with a content of two molecules. A number of different packing motifs are found.

Three of them show anti-parallel molecules, they were selected for further considerations. Their respective molecular packings are shown as insets of Figure 4b-d. In case of the first packing motif (denoted as mixed layers, Fig. 4b), the individual layers are composed by blended decyl chains and aromatic units. In case of the second and third packing motif (denoted as nano-segregated), the structure shows separation of the molecular parts into layers formed by aromatic units and layers formed by decyl chains. Within the nano-segregation further differentiation is found for the packing of the aromatic units i) tilting relative to each other (herringbone arrangement, Fig. 4c) or ii) parallel stacking upon each other (stacked arrangement, Fig. 4d). The respective crystallographic information files (cif - files) of these three packing motifs are given in the Supporting Information of this paper.

In a subsequent step, the three different packing motifs were used to calculate structure factors and comparisons of calculated and experimental structure factors are made. In the first step R-factors were calculated for all observed Bragg peaks (compare Fig.4b-d), the results are shown in Table 2. The largest R-factor is found for the mixed layer system, both nano-segregated structures show considerably smaller R-values. From this point of view, the mixed layer motif seems to be the least favourable molecular packing within the SmE phase. However, it cannot be decided which type of nano-segregated structure is present.

packing motif	R	energy
mixed layer	1.53	130.7%
nano-segregated herringbone	0.67	100%
nano-segregated stacking	0.65	159.5%

Table 2: Comparison of the reliability factors for X-ray diffraction (R-factors) and of the total energies obtained from Molecular Dynamics calculations for the three different packing motifs. The energies are given relative to the lowest obtained energy.

Our molecular dynamics simulations reveal that the three different packing motifs are associated with characteristic energies. Therefore, we use these energies as a criterium for assignment of a specific packing motif to the SmE phase. Since the obtained total energies are less meaningful, we decided to give fractional values relative to the lowest energy state (Tab.2). Our calculation reveal that the herringbone packing is the lowest energy state and the difference to the other two packing is comparable large. Please note, that the considerable higher energies for the two other packing motifs (mixed layer / nano-segregation with parallel stacking) is a consequence of squeezing the molecules into a given crystallographic unit cell. Therefore, the given energy values are not representative for a relaxed state of these two packing motifs.

Based on the comparison of the experimental and the calculated diffraction pattern together with energy considerations of the Molecular Dynamics simulations, we conclude that nano-segregation with herringbone packed aromatic units is present within the SmE phase of the molecule Ph-BTBT-10. The result that herringbone packing is present within the SmE phase is in accordance

with the literature [24,86]. Please note that the negligible intensities of the *10l* and *01l* peaks in the experimental diffraction pattern (compare Fig. 5c) is a characteristic feature of herringbone packing frequently observed even for alkyl terminated conjugated molecules[37,91].

Analysing the molecular packing of the nano-segregated herringbone packing in terms of molecular conformation reveal that a planar confirmation of the aromatic unit is obtained. This can be expected, since the anti-parallel alignment of the molecules cause that the phenyl unit and the BTBT unit are next to each other and an integration of both units into an intermolecular herringbone arrangement makes a planarization reasonable. A herringbone angle of 54° is obtained which is comparable with an angle of 50° observed for the bulk phase. The tilt angle of the decyl side chain relative to the aromatic unit is 40°, this value is comparable to the 35° tilt angle observed within the bulk phase.

Discussion

Asymmetric molecules which are composed of aromatic units and aliphatic chains show often combined SmE and SmA phases [85,87]. In the case of the molecule Ph-BTBT-10 we found a stacking distance of 28.1 Å for the SmA phase which is in quite good agreement with atomistic modelling by molecular dynamics[16].

The previous analysis of the molecular packing within the SmE phase of the molecule Ph-BTBT-10 is based on the transition from the bulk phase to the SmE phase. A bilayer structure showing *head-to-head* arrangements of the molecules is transferred to the SmE phase with a single layer structure with *head-to-tail* arrangement. A mechanism for a defined transition from a *head-to-head* arrangement to a *head-to-tail* arrangement is possible by collective translational movement of the molecules [17,18].

Our approach of molecular dynamics simulation is based on the experimentally observed crystallographic unit cell of the SmE phase. Starting from random arrangements of the molecules, the system is reduced to the actual unit cell size.

The obtained packing motifs are analysed in terms of energy and in accordance with the experimental diffraction pattern. Please note that the presented results consider fixed aromatic units and fixed alkyl chains. Thermal movements, molecular disorder and displacement of the molecules is not included. It is stated in the literature that the alkyl chains are in a molten state within the SmE phase and the molecular packing is determined by the rigid character of the aromatic units[24,92]. We found that the packing of the aromatic units appears in herringbone arrangement.

Our results reveal that the molecular packing of the molecules is rather nano-segregated which means that the phenyl-BTBT units and the decyl units form separated layers within a molecular sheet. This contradicts the classical view of a SmE phase but in agreement with more recent concepts [93,94]. The nano-segregated structure of the SmE phase together with the anti-parallel alignment of the molecules results in an interdigidation of the decyl chains originating from two aromatic layers of neighbouring layers. Interdigidation of alkyl chains within sheet structures may be favoured from thermodynamic state, but may be hindered by growth kinetics as discussed in detail for the polymer poly(3-hexylthiophene) [95,96]. It is found also for another BTBT based molecule, e.g. 2,7-dioctyloxy[1]benzothieno[3,2-b]benzothiophene that polymorph phases with and without interdigidated side chains exists[97].

Conclusion

Thin films of the molecule Ph-BTBT-10 are investigated in terms of their molecular packing as a function of temperature. A phase transition from the bulk state to a SmE phase and finally to a SmA phase is observed by X-ray diffraction experiments. Sharp transitions from the bulk crystal phase to the SmE phase and further to SmA phase are observed at 149°C and 220°C, respectively. The transition to the SmE phase is associated with a change from a monoclinic to an orthorhombic unit cell with a discontinuous change of the lattice constants. The available space of a single molecule increases substantially from 622 $Å^3$ in the bulk phase to 731 $Å^3$ in the SmE phase. Analysis of the peak width by a paracrystalline model reveal that

the in-plane order is reduced (crystal size of 50 Å and 4% paracrystallinity) in comparison to the out-of plane order (100 Å / 10%). Based on the crystallographic lattice constants, obtained from GIXD analysis, molecular packing analysis was performed by molecular dynamics calculations. Three different packing motifs with antiparallel alignment of the molecules are found. A comparison of calculated and experimental diffraction pattern reveals that the “mixed layer” packing motif is unlikely while the nano-segregation of decyl chains from the aromatic units is more probably present within the SmE phase. Considering the two different types of aromatic packing within nano-segregation (“parallel stacking” and “herringbone arrangement”), the lowest energy of the molecular dynamics simulations is found for herringbone arrangement of the aromatic units.

Associated Content

Crystallographic information files for the three considered different molecular packings. Structures formed by i) sheets of blended decyl chains and aromatic units (mixed_layer.cif), sheets of nano-segregated decyl chains and aromatic units with ii) herringbone arrangement of the aromatic units (nanoegregated_herringbone.cif) and iii) with parallel stacking of the aromatic units (nano-segregated_stacking.cif).

Acknowledgments

The authors acknowledge the synchrotron Elettra, Trieste for allocation of synchrotron radiation and thank Luisa Barba and Nicola Demitri for assistance in using beamline XRD1.

Disclosure statement

No potential conflict of interest was reported by the authors.

Funding

The work was supported by the Austrian Science Foundation (FWF) under the Grant P30222. The measurements at CzechNanoLab Research Infrastructure were financially supported by MEYS CR (LM2018110).

4.3 Molecular Disorder in Crystalline Thin Films of an Asymmetric BTBT Derivative

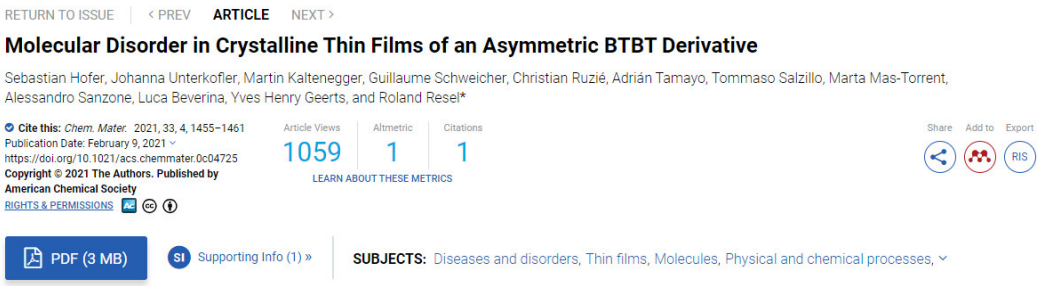

This manuscript was prepared in collaboration with Johanna Unterkofler, who prepared most of the samples in the group of Yves Geerts. A further batch of samples was prepared by Adrián Tamayo in the group of Marta Mas-Torrent and material synthesis was done by Alessandro Sanzone in the group of Luca Beverina. The main batch of the samples was measured by Johanna Unterkofler together with the first author who did the data analysis and modelling of the results. Preparation and proof-reading of the manuscript was done by all authors.

The article is available at: https://doi.org/10.1021/acs.chemmater.0c04725

Molecular Disorder in Crystalline Thin Films of an Asymmetric BTBT Derivative

Sebastian Hofer, Johanna Unterkofler, Martin Kaltenegger, Guillaume Schweicher, Christian Ruzié, Adrián Tamayo, Tommaso Salzillo, Marta Mas-Torrent, Alessandro Sanzone, Luca Beverina, Yves-H. Geerts, Roland Resel*

Abstract

The molecule 2-decyl-7-phenyl-[1]benzothieno[3,2-b][1]benzo-thiophene (Ph-BTBT-10) is an organic semiconductor with outstanding performance in thin film transistors. The asymmetric shape of the molecule causes unusual phase behavior which is a result of a distinct difference in the molecular arrangement between head-to-head stacking of the molecules versus head-to-tail stacking. Thin films were prepared at elevated temperatures by crystallization from the melt under controlled cooling rates, thermal gradient crystallization and bar coating at elevated temperatures. The films are investigated by X-ray diffraction techniques. Unusual peak broadening effects are found which cannot be explained by standard models. Modelling of the diffraction pattern with statistic variation of the molecules reveal that a specific type of molecular disorder is responsible for the observed peak broadening phenomena: the known head-to-head stacking within the crystalline phase is disturbed by statistic integration of reversed (or flipped) molecules. It is found that 7% to 15% of the molecules are integrated in a reversed way, these fractions are correlated with cooling rate during the sample preparation procedure. Temperature dependent in-situ experiments reveal that the defects can be healed by approaching the transition from the crystalline state to the *smectic E* state at a temperature of 145°C. This work identifies and quantifies a specific crystalline defect type within thin films of an asymmetric rod-like conjugated molecule which is caused by the crystallization kinetics.

Introduction

The crystal structure is of fundamental importance to understand the properties of organic semiconductors. The long-range order of the molecules is a defined way to describe the molecular packing so that electronic and phonon band structures can be calculated. The distribution of the electrons in terms of their energies and their apparent momenta is the basis to understand charge transport in these

materials[98]. However, also the deviation from the ideal crystal lattice is important to understand application relevant properties of organic semiconductors[99]. There exists a variety of structural defects which cause a further variation from the ideality[100]. Chemical defects arise from substitutional molecules[101] or physical defects due to the distortion of the periodic lattice like vacancies, dislocation lines or stacking faults[102,103]. Optical properties as well as charge transport within organic semiconductors are highly affected by defects[104,105,106]. Structural defects at considerable larger length scales are crystal size and crystal mosaicity associated with grain boundaries between single crystalline domains[107].

The solution of crystal structures is a widely used and highly developed technique mainly based on X-ray diffraction[108]. The characterization of structural defects is considerably more difficult, direct observations by microscopy methods are the most successful techniques[109]. But microscopy methods are often difficult to perform and give only selective results, therefore the use of integral methods is preferred. Thereof, x-ray scattering techniques are preferred, but the nature of the structural defects are often difficult to identify[34].

There are a number of effects in X-ray diffraction pattern which can be assigned to defects. Diffuse scattering (the scattering apart of Bragg peaks) appears, since defects breaks the long range periodicity of a crystal structure[110,111]. Peak broadening of Bragg peaks is one quite well-developed tool to characterize the deviation from the ideal infinitely extended perfect crystal. The two contributions for peak broadening are microstrains (root mean square of the variations in the lattice parameters) and crystal size (size of the ideal crystal in direction of the scattering vector). The separation of these two effects is possible by Williamson-Hall plots[112]. This method has successfully been applied to thin films of organic semiconductors[113,114].

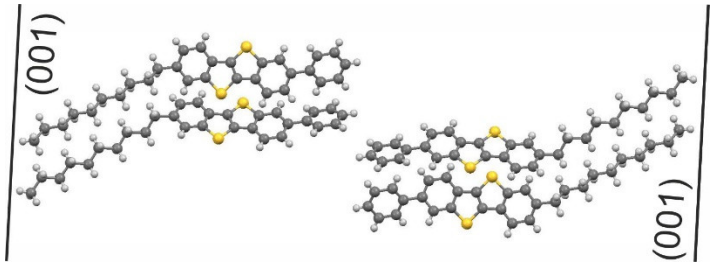

Figure 1: Packing of the molecule Ph-BTBT-10 within the crystalline state, bilayers are formed with head-to-head arrangement of the molecules. Additionally, the crystallographic (001) planes are drawn.

The molecule 2-decyl-7-phenyl-[1]benzothieno[3,2-b][1]benzo-thiophene (Ph-BTBT-10) is a recently developed organic semiconductor with excellent performance in thin film transistors [48,49]. The asymmetric nature of the molecule – there is a phenyl ring at one terminal end of the aromatic benzothieno-benzothiophene core and a decyl chain at the other terminal end – causes a specific phase behavior as a function of temperature. Starting from elevated temperatures, a phase transition from the isotropic liquid to the *smectic A* phase appears at 223°C and subsequently a transition to the *smectic E* phase at 210°C[48,82]. The transition between the liquid crystalline state and the crystalline state is accompanied with strong retardation effects: the onset of crystallization appears at around 100°C, while melting of the crystalline state happens at a temperature of about 143°C. Within the crystalline state the molecules form a double layer herringbone structure: layers are formed from separated alkyl chains and of the aromatic parts of the molecule (compare Fig.1)[81]. The molecules of neighboring layers are arranged in a head-to-head arrangement, so that the BTBT core together with the terminal phenyl ring points towards each other.

Thin film preparation for transistor applications is performed at elevated temperatures, since the moderately ordered *smectic E* phase is expected as a pre-stage of crystallization[77,78]. The present work here shows that molecular disorder is obtained when thin films of the molecule Ph-BTBT-10 are processed from elevated temperature. The obtained crystalline packing is substantially disordered

and the type of defect could be identified. The defects could be healed by heat treatment at temperatures close to phase transition to the liquid crystalline state.

Experimental section

One batch of the molecule Ph-BTBT-10 was synthetized according to the strategy recently published [48]. The first sample series was deposited on 20 x 20 mm^2 Menzel glass substrates by drop casting from an 8 g/l solution. Toluene was used as solvent. The thin film samples were heated up to 245°C, a temperature well above the melting point of the material[48]. In a subsequent step the samples were cooled down to room temperature, defined cooling rates between 0.8°C/min up to 30°C/min were chosen. The heat treatment was performed with the commercially available domed hot stage DHS900, Anton Paar[52].

The second sample series was also based on drop casted thin films from toluene solutions, but the heat treatment was performed by thermal gradient crystallization[115]. The setup consists of two independent heating stages (hot end and cold end) separated by a gap of 2.5 mm. A mechanical arm allows a displacement of the sample from the hot end to the cold one at a constant translation velocity, chosen in between 1 µm/s and 20 µm/s. For that purpose, the thin film was covered by an additional glass slide. The stack (substrate / thin film / top glass) was heated to 245°C for a complete melting of the thin film. Crystallization takes place by a translational movement towards the low temperature zone which was held at 75°C, a temperature well below the crystallization temperature of Ph-BTBT-10. The used system is a Linkam GS350 temperature gradient heating stage combined with a Nikon Eclipse 80i polarized light microscope.

The third sample series was prepared by shear crystallization[116] on oxidized silicon wafers by bar assisted meniscus shearing following the previously reported methodology[117]. Solutions of chlorobenzene and o-xylene were used with a concentration of 2% and 2.5% w/w, respectively. Also, solutions of blends of Ph-

BTBT-10 with polystyrene (PS) in a ratio Ph-BTBT-10:PS 2:1 and using the same solvents and concentrations were employed. The addition of a binding insulating polymer has been reported to promote the crystallization of the organic semiconductor and improve the thin film homogeneity[118]. The deposition was performed at elevated substrate temperatures of 105°C and 110°C for chlorobenzene and o-xylene, respectively.

Specular X-ray diffraction was performed with an PANalytical Empyrean system using a sealed copper tube together with a multilayer mirror for generating a parallelized and monochromatized primary X-ray beam. A wavelength of 1.542 Å was used. The scattered intensity was detected with a PIXcel detector operating as in one-dimensional mode for long range measurement and as point detector for short range measurements. The diffraction pattern was converted into reciprocal space by $q = \frac{4\pi}{\lambda} sin\theta$ with q as the length of the scattering vector, λ the used wavelength and 2θ the angle between the primary and the scattered X-ray beam. The peak parameters were evaluated by subtracting the experimental background and fitting a Gauss curve to determine peak positions and peak widths; the peak widths are given as full width at half maximum. *In-situ* temperature dependent measurements were performed by using the high temperature attachment DHS900[52], setting the temperature and waiting 10 minutes to let the system equilibrate before taking the measurement. Subsequently, the temperature is increased in steps of 2°C close to the phase transitions and with a step size of 10°C elsewhere.

Calculations of specular diffraction pattern were performed by Fourier transforms of the electron densities. The electron density was modeled by the number of electrons for each atom in a single molecule of Ph-BTBT-10 along the 001 direction, with a width based on the atomic form factor for each element. Based on the known crystal structure of Ph-BTBT-10 a layered structure was assumed with a defined layer distance of 26.5 Å. The thickness of the layer result from length of the molecule together with their molecular packing by a herringbone type. The electron density distribution across the layers was chosen as non-

periodic by molecular disorder. To include the disorder each layer is stacked on top of the previous layers with a certain probability of being either in head-to-head or head-to-tail fashion. The fraction of molecular disorder *p* is defined by the fraction of molecules with head-to-head orientation. A molecular disorder parameter *p = 0* appears, if the number of up-right standing molecules is equal to the downward oriented molecules. A number of repeating units is set at 30 to be in the best agreement with the experimentally prepared samples. This modelling is repeated up to 200 times and the resulting Fourier signal is averaged to generate a smooth calculated diffraction signal.

Grazing incidence X-ray diffraction was performed at the XRD1 beamline, Elettra, Trieste. The primary X-ray beam with a wavelength of 1.400 Å and a size of 500 x 500 μm^2 enclosed an incident angle of 1.5° with the sample surface. The diffracted beams were detected with a stationary Pilatus 2M detector. The diffraction pattern was converted into reciprocal space by using the software *GIDVis*[119], calculation of peak positions and peak intensities from the known crystal structure of Ph-BTBT-10 was performed by the module *crystal* available within the *GIDVis* package.

All three sample series were investigated by specular X-ray diffraction. The first sample series is based on drop casted thin films. The result of an untreated drop casted film is shown in Fig.2a.

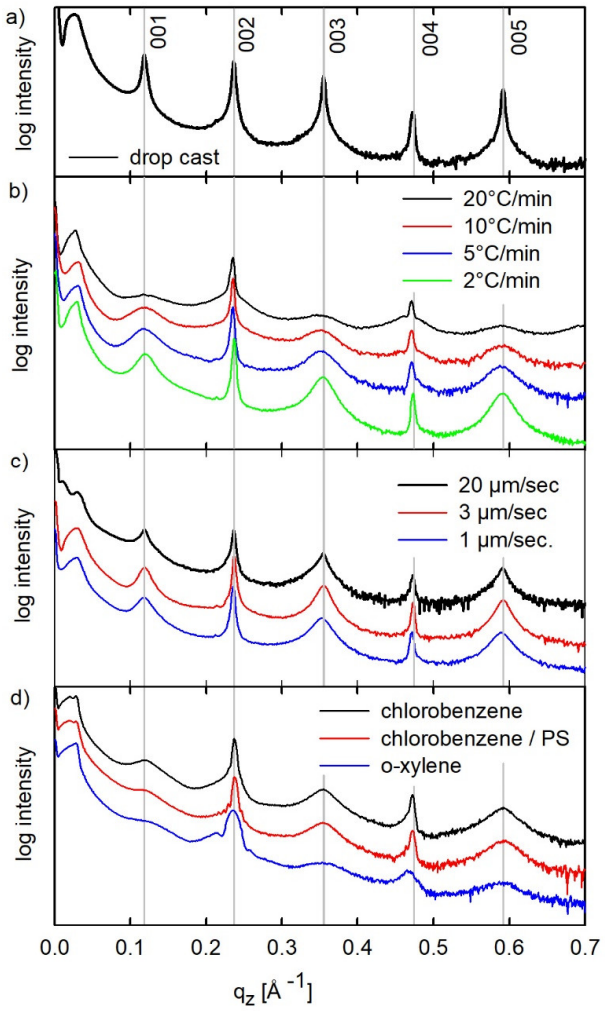

Figure 2: Specular X-ray diffraction of thin films of the molecule Ph-BTBT-10. (a) an untreated film, (b) films obtained from the melt by defined cooling rates, (c) thermal gradient crystallization from different withdrawal velocities and (d) shear crystallization using different solvents with and without using polystyrene (PS) as binding polymer.

The diffraction pattern reveals defined diffraction peaks which could be indexed on basis of the known crystal structure of Ph-BTBT-10[14]. The peak located at 0.118 $Å^{-1}$ can be assigned to the 001 Bragg peak and higher order reflections are observed up to the 5th order. The expected peak positions of the 00L (L = 1 …5) peaks are drawn by vertical lines.

Drop casted films were then thermally annealed above melting point and subsequent crystallization of Ph-BTBT-10 was performed at defined cooling rates (Fig.2b). Similarly, to drop casted films, all the 00L peaks from the annealed samples were clearly visible. However, an outstanding feature is the considerable broadening of the 001, 003 and 005 peaks, while the 002 and 004 peaks do not show broadening in respect to the untreated sample. The peak broadening is more enhanced at larger cooling rates. The largest peak widths of the odd-numbered 00L peaks is observed for the sample prepared using the highest cooling rate of 20 °C/min; in this particular case also the even-numbered 00L peaks starts to broaden.

The next sample series is prepared by thermal gradient crystallization; the results are depicted in Figure 2c. 00L Bragg peaks are observed at the expected positions of the known crystal phase. Even in this case the odd-numbered 00L peaks are broadened considerably in comparison to the even-numbered 00L peaks. No clear dependence of the peak broadening is observed as a function of the withdrawal velocity. The last sample series is prepared by bar coating at elevated temperatures from solution using different solvents. Similarly to the other treatments, odd-numbered 00L peaks are considerably broadened in comparison to even-numbered 00L peaks.

An observation of only 00L peaks within a specular diffraction pattern is a frequently observed case[48,120] and reveals a highly defined preferential out-of-plane orientation of the crystallites. In our case, the crystals grow with the (001) plane parallel to the substrate surface. The appearance of more than a single 001 Bragg peak is referred to higher order reflections arising from the (001) net plane. Peak width analysis can be performed with high accuracy on basis of a peak series

arising from a series of higher order reflections. Broadening due to crystallite size and due to microstrain can be clearly separated[121]. However, peak widths which alternate with the order of diffraction cannot be explained by classical diffraction models[122,123].

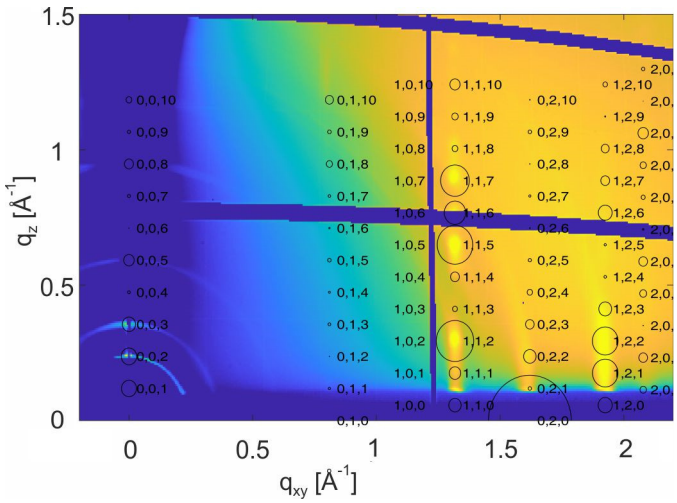

Figure 3: Reciprocal space map of a thermally gradient crystallized thin film (translation velocity 2.5 µm/sec.) together with indexation of the diffraction pattern based on the known bulk structure of the molecule Ph-BTBT-10. For the indexation only the strongest Bragg peaks are depicted by circles, where the center and areas of the circles give the peak positions and peak intensities, respectively.

In a next step, more comprehensive structural studies are performed to get more details on the crystallographic properties of Ph-BTBT-10 within thin films. GIXD diffraction patterns are measured in an extended range so that a characteristic peak pattern of the Ph-BTBT-10 is observable. Figure 3 shows a reciprocal space map of a thermally gradient crystallized film. The map shows the characteristic fingerprint of a herringbone packing typically for rod-like conjugated molecules: elongated intensity features are observed along the q_z direction at defined q_{xy} values at 1.31 Å^{-1}, 1.60 Å^{-1}, 1.91 Å^{-1} [39,37]. The reciprocal space map is indexed on basis of the known phase of Ph-BTBT-10, assuming a 001 preferred orientation of the crystallites. The comparison of the calculated diffraction peaks with the experimentally observed peak pattern reveals that the bulk phase of Ph-BTBT-10

is present within the thin film. The excellent agreement can be clearly seen for the strongest diffraction peaks like 112, 115, 117 but also for 121 and 122. The known crystal structure could be confirmed also for the samples prepared by defined cooling rates and for the bar coated samples (compare Fig. S1).

The specular X-ray diffraction studies (Fig.2) as well as the GIXD investigations (Fig.3) reveal that the known crystal structure of Ph-BTBT-10 is present within our thin films. Based on the known molecular packing within the bulk structure a possible explanation of the outstanding peak broadening phenomena can be developed. We assume disorder of the molecules within the crystal structure as the reason for the unusual behavior. The molecular disorder breaks the crystallographic long-range order, therefore, it cannot be treated by classical diffraction theory. As a consequence, statistical simulations have to be performed. The simulation model starts with the crystal structure of Ph-BTBT-10 using double herringbone layers with head-to-head arrangements of the molecules. The molecular disorder is implemented by inverted molecules as deviation from the crystallographic periodicity. The molecular disorder parameter *p* describes the fraction of head-to-head aligned molecules; *p* = 0 represents molecules only with head-to-head arrangement while *p* = 1 represents a molecular packing based on head-to-tail arrangements.

The results of the simulations are depicted in Figure 4. Specular diffraction patterns are plotted as a function of the disorder parameter *p* in a waterfall plot.

No peak broadening is observed for *p* = 0, but a slight increase of the disorder parameter immediately causes a peak broadening of the odd-numbered 00L peaks, while even-numbered 00L peaks remain at their initial peak width. The peak widths on the odd-numbered 00L peaks increase by increasing the parameter *p* and disappears at about *p* = 0.4. Simulations are performed by random distributions as well as by systematic distributions of the inverted molecules; even random sequences of layers with identical molecular alignment have been considered. We found that the molecular disorder parameter *p* is a reasonable parameter to describe the observed effect on the peak broadening.

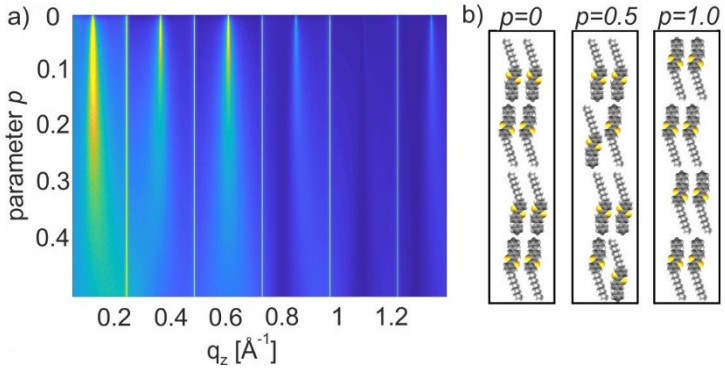

Figure 4: Simulation of a specular diffraction pattern of the (001) plane of Ph-BTBT-10 crystallites with different degree of random molecular disorder *p* presented in a color contour plot. The intensity scale is color coded from yellow for high intensity via green to blue for low intensity (a). The molecular disorder parameter *p* represents the deviation from the ideal head-to-head packing present within the known bulk structure (b).

In the next step, the influence of heat treatment to the observed peak broadening phenomena is investigated. Temperature dependent *in-situ* X-ray diffraction experiments are performed on a sample prepared by thermal gradient crystallization. Specular scans were started at 120°C and performed stepwise in temperature up to complete melting of Ph-BTBT-10 at 230°C. The temperature was increased in steps of 3°C close to the phase transitions and in steps of 10°C otherwise. After each increase of the temperature the system is held at the temperature for 5 minutes to equilibrate. A section of the measurements is presented by a color contour plot in Figure 5a. The 00L peak series is clearly visible together with their variable peak width (compare Fig.2). At a temperature of 147°C, the expected phase transition to a *smectic E* phase takes place, clearly visible by disappearance of the odd-numbered 00L peaks and a clear shift in the peak position of the even-numbered 00L peaks.

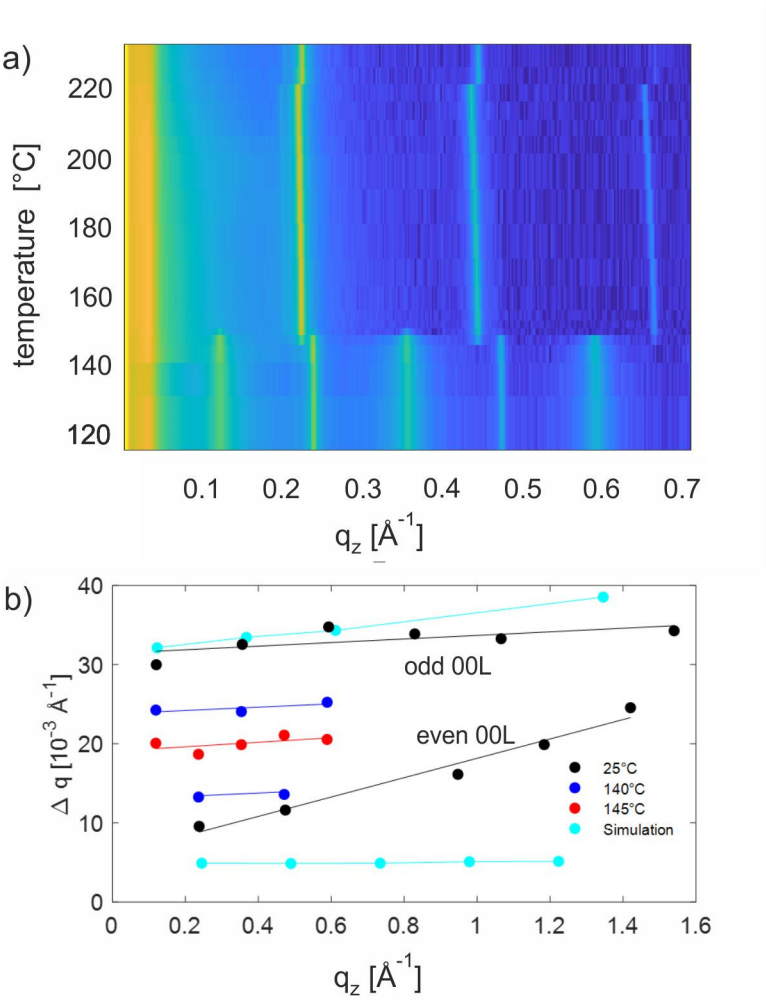

Figure 5: A series of *in-situ* specular X-ray diffraction of a thermal gradient crystallized thin film (translation velocity 2 µm/sec.) presented in a color contour plot. The measurements are given in the temperature range from 120°C to 180°C covering the phase transitions from the crystalline state to *smectic E* at 145 °C. The intensity scale is color coded from yellow for high intensity via green to blue for low intensity (a). Peak width analysis of specular diffraction peaks (Laue indices 00L) of a thermally gradient crystallized thin film (translation velocity 1.5 µm/sec.) as a function of temperature, additionally the peak widths from the simulation are given for a molecular disorder parameter *p = 0.15* (b).

The peak widths (Δq) of the *in-situ* studies are evaluated as a function of temperature and plotted in comparison to an *ex-situ* measurement at room temperature (25°C). The results are shown in Figure 5b. Plotting of the peak width

as a function of the length of the scattering vector q (Williamson-Hall plots) reveals linear behavior as it is expected from classical diffraction theory[122,123]. Considering the peak width at 25°C, the odd-00L peak series show a different dependence than the even-numbered 00L peak series. Here, the peak widths of the 00L peaks are plotted up to L = 14. In a next step, the peak widths are considered at elevated temperatures. Approaching the phase transition temperature for the *smectic E* phase, the peak width of the odd-numbered peaks decreases and the width of the even-numbered peaks increases. At a temperature just below the phase transition at 145°C the peak widths of all 00L peaks are arranged in one line. The variable peak width of the 00L peaks disappears just at the phase transition to the *smectic E* phase. For comparison, we plotted the peak width of our simulation with p = 0.15. In both cases – odd as well as even based 00L peaks - we observe linear behavior. The peak widths are comparable only in the low q-range (for the 001 and 002), since we do not include microstrains in our calculations. Please note that our calculations were performed for a stack of 30 repeating units.

In a final step, Williamson-Hall plots are prepared for the sample series prepared at defined cooling rates. A clear correlation between the cooling rates and the molecular disorder parameter p was found (Fig. S2). Cooling rates of 10 °C/min and 2 °C/min result in p = 0.15 and 0.07, respectively; intermediate rates result in disorder parameters in between.

Discussion

The thin films were prepared by a variety of methods; in all cases a heat treatment procedure was involved. In the first case the films were obtained by a defined cooling from the melt, in the second case the films were crystallized from the melt within a thermal gradient and in the third case, the films were obtained by bar coating at elevated temperatures with a subsequent cooling to room temperature. After full solidification, the films crystallize in the known bulk structure of Ph-BTBT-10, as shown by specular X-ray diffraction as well as by GIXD investigations.

The outstanding experimental observation is that the peak width of the specular diffraction shows a different peak broadening behavior for the odd-numbered and even-numbered 00L peaks. For an explanation of this effect molecular disorder was assumed. Simulations are started with layered structures of the Ph-BTBT-10 with a double herringbone structure with head-to-head oriented molecules. Gradually introducing defects by inverted molecules, the odd-numbered peaks start to broaden while even-numbered peaks remain at their initial peak width. This phenomenon starts already at small deviations from the ideal crystal structure. It is found that the fraction of head-to-head aligned molecules (molecular disorder parameter *p*) is a meaningful parameter which describes the observed effect. Different types of the molecular disorder are investigated. Systematic inversion of all molecules within one layer or inversion of random molecules lead to the same result. Assignment of the observed peak broadening to the disorder parameter *p* reveals values of 0.15 for a gradient crystallized sample and values in between 0.15 and 0.07 for samples prepared at defined cooling rates.

An interesting effect is that the peak broadening disappears as a function of heat treatment. A change of the peak width is observed when the thin film is heated (from room temperature) close to the phase transition temperature of the *smectic E* phase. The peak broadening disappears fully at the phase transition temperature which means that the molecular disorder is strongly reduced. Taking our disorder model into account, flip-flops of molecules have to appear close to the transition temperature to the *smectic E* phase, which can be explained by a pure translational movement of molecules across different layers[17,39].

The ability of the molecules to reverse its molecular orientation at elevated temperatures is a known phenomenon. Flip-flop motions of individual molecules are frequently observed in the liquid crystalline state[124]. Phase transitions (i.e. nematic to isotropic) are analyzed on basis of flip-flop motions together with the available space of the molecules within the liquid crystalline phases[125,126]. However, liquid crystalline states with higher degree of order provides less space

for molecular motion and as a consequence the molecules are less prone to flip-flop transitions[127,128]. Also in the solid state flip-flop motions becomes possible, but only close to the transition to a liquid state as observed for bilayers of phospholipids at the transition from the gel phase to the fluid phase[129].

Conclusion

A series of thin films were prepared from the molecule Ph-BTBT-10 using various heat-treatment-based methods and investigated via X-ray diffraction methods. At room temperature the bulk crystal structure of the material is observed, but a specific anomaly is observed in the peak widths of the 00L Bragg peaks. A model is set up to include molecular disorder, based on molecules which are embedded in a reversed manner (flipped molecules) into the bulk crystal structure. The unexplained peak broadening phenomena can be explained satisfactorily by a disorder parameter, which quantifies the fraction of disordered molecules. It was found that 7% to 15% of the molecules show a reversed molecular alignment due to crystallization from elevated temperatures. Temperature treatment close to the liquid crystalline state allows the molecules to orient into the expected molecular alignment determined by the crystal structure.

This Supporting Information complement the grazing incidence X-ray diffraction pattern presented in Figure 3 of the main manuscript. Additionally, a peak width analysis is performed for the sample series prepared at different cooling rates. The defined variation of the sample preparation conditions allows an assignment of the disorder parameter *p* to the cooling rate of the thin films during the solidification process.

Grazing Incidence X-ray Diffraction

GIXD pattern of the other two types of thin films are presented just to confirm that in all three different types of thin films the known crystal structure of the molecule Ph-BTBT-10 is present. Grazing incidence X-ray diffraction pattern are given for a sample prepared by defined cooling rates and of a sample prepared by bar coating. The results are shown in Figure S1. A stationary measurement was performed in case of the sample with a cooling rate of 5°C / min. The sample war rotated by 180° for the bare coated sample, since the bare coating technique induce azimuthal alignment of the Ph-BTBT-10 crystallites.

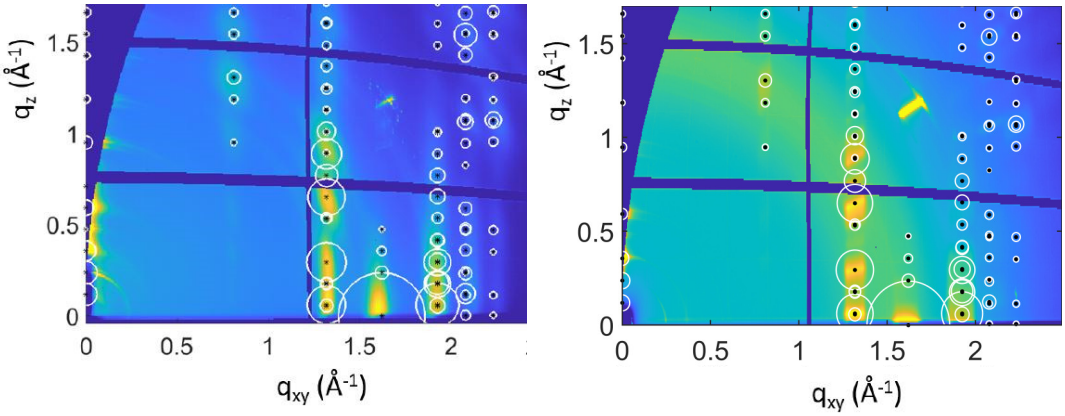

Figure S1: Grazing Incidence X-ray diffraction of a thin film prepared with a defined cooling rate of 5°C / min (left) and of a bar coated sample prepared from cholorobenzene solution at a temperature of 105°C (right). The circles give calculated peak position / peak intensities from the known bulk structure of Ph-BTBT-10.

Sample series at defined cooling rates - peak width analysis

The peak width of the sample series prepared by different cooling rates are compared with each other. This comparison should reveal the impact of the cooling rate to the molecular disorder parameter p. The parameter p is found in between 0.07 And 0.15 for the samples prepared at rates of 2°C/ min and 10°C / min, respectively.

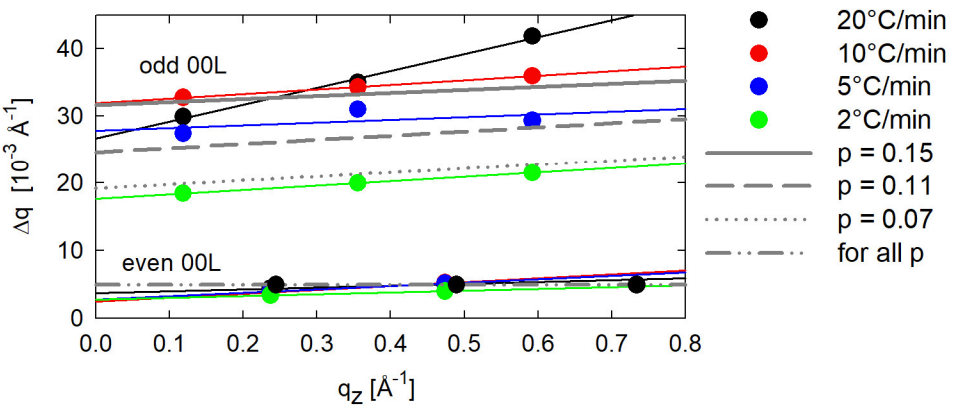

Figure S2: Peak width analysis of the sample series prepared at defined cooling rates. Grey lines indicate the peak width of the odd-numbered diffraction peaks at different molecular order parameters.

Author information

Corresponding Author

Roland Resel, Institute of Solid State Physics, Graz University of Technology, Petersgasse 16, 8010 Graz, Austria; orcid.org/0000-0003-0079-3525

Email: roland.resel@tugraz.at

Authors

Sebastian Hofer, Institute of Solid State Physics, Graz University of Technology, Petersgasse 16, 8010 Graz, Austria

Johanna Unterkofler, Institute of Solid State Physics, Graz University of Technology, Petersgasse 16, 8010 Graz, Austria

Martin Kaltenegger, Institute of Solid State Physics, Graz University of Technology, Petersgasse 16, 8010 Graz, Austria; Laboratoire de Chimie des Polymères, Faculté des Sciences, Université Libre de Bruxelles, Campus Plaine, CP206/01 - Boulevard du Triomphe, 1050 Bruxelles, Belgium

Guillaume Schweicher, Laboratoire de Chimie des Polymères, Faculté des Sciences, Université Libre de Bruxelles, Campus Plaine, CP206/01 - Boulevard du Triomphe, 1050 Bruxelles,, Belgium; orcid.org/0000-0002-6501-0790

Christian Ruzié, Laboratoire de Chimie des Polymères, Faculté des Sciences, Université Libre de Bruxelles Campus Plaine, CP206/01 - Boulevard du Triomphe, 1050 Bruxelles, Belgium

Adrián Tamayo, Institut de Ciència de Materials de Barcelona, ICMAB-CSIC,

Campus de la UAB, Carrer dels Til·lers, Bellaterra, 08193 Barcelona, Spain;

orcid.org/0000-0002-3911-6807

Tommaso Salzillo, Institut de Ciència de Materials de Barcelona, ICMAB-CSIC, Campus de la UAB, Carrer dels Til·lers, Bellaterra, 08193 Barcelona, Spain; orchid.org/ 0000-0002-9737-2809

Marta Mas-Torrent, Institut de Ciència de Materials de Barcelona (ICMAB-CSIC), Campus de la UAB, Carrer dels Til·lers, Bellaterra, 08193 Barcelona, Spain; orchid.org/0000-0002-1586-005X

Alessandro Sanzone, Department of Materials Science, University of Milano-Bicocca, Via Roberto Cozzi, 55, 20125 Milano, Italy

Luca Beverina, Department of Materials Science, University of Milano-Bicocca, Via Roberto Cozzi, 55, 20125 Milano, Italy; orchid.org/0000-0002-6450-545X

Yves –H. Geerts, Laboratoire de Chimie des Polymères, Faculté des Sciences, Université Libre de Bruxelles & International Solvay Institutes of Physics and Chemistry, Campus Plaine, CP206/01 - Boulevard du Triomphe, 1050 Brussels, Belgium; orcid.org/0000-0002-2660-5767

Acknowledgments

This work was supported by the Fonds de la Recherche Scientifique (FNRS) and the Fonds voor Wetenschappelijk Onderzoek – Vlanderen (FWO) under EOS project 30489208 and the Austrian Science Fund (FWF): [P30222]. YG is also thankful to FNRS for financial support through research projects BTBT n° 2.4565.11, Phasetrans n° T.0058.14, Pi-Fast n° T.0072.18, and 2D to 3D No. 30489208. Financial supports from the French Community of Belgian (ARC n° 20061) and by the Walloon Region (WCS No. 1117306, SOLIDYE n° 1510602) are also acknowledged. G.S. acknowledges postdoctoral fellowship support from the FNRS. MM thank the Spanish Ministry project GENESIS PID2019-111682RB-I00, the "Severo Ochoa" Programme for Centers of Excellence in R&D (FUNFUTURE, CEX2019-000917-S) and the Generalitat de Catalunya (2017-SGR-918). A.T. is enrolled in the Materials Science PhD program of Universitat Autònoma de Barcelona and acknowledges FPU fellowship from the Spanish Ministry. The large-scale facility Elettra, Trieste, Italy, provided synchrotron radiation for grazing incidence X-ray diffraction experiments at the beamline XRD1.

4.4 Mobility anisotropy in the herringbone structure of asymmetric Ph-BTBT-10 in solution sheared thin film transistors

Issue 22, 2021

Previous Article | Next Article

From the journal:
Journal of Materials Chemistry C

Mobility anisotropy in the herringbone structure of asymmetric Ph-BTBT-10 in solution sheared thin film transistors†

Check for updates

Adrián Tamayo, ‡[a] Sebastian Hofer, ‡[b] Tommaso Salzillo, §[a] Christian Ruzié,[c] Guillaume Schweicher,[c] Roland Resel *[b] and Marta Mas-Torrent *[a]

The paper was prepared in close collaboration with the group of Marta Mas-Torrent. The sample preparation and electrical characterization was carried out by Adrián Tamayo, whereas Sebastian Hofer analyzed the structural characteristics and crystallite orientation. Shared first-authorship was agreed upon the two. Preparation of the manuscript and proof-reading was done by all authors.

The article is available at: https://doi.org/10.1039/D1TC01288F

Mobility anisotropy in the herringbone structure of asymmetric Ph-BTBT-10 in solution sheared thin film transistors

Adrián Tamayo,[a,‡] Sebastian Hofer,[b,‡] Tommaso Salzillo,[a,d] Christian Ruzié,[c] Guillaume Schweicher,[c] Roland Resel[b] * and Marta Mas-Torrent [a] *

Abstract

Thin films of the organic semiconductor Ph-BTBT-10 and blends of this material with polystyrene have been deposited by a solution shearing technique at low (1 mm/s) and high (10 mm/s) coating velocities and implemented in organic field-effect transistors Combined X-ray diffraction and electrical characterisation studies prove that the films coated at low speed are significantly anisotropic. The highest mobility is found along the coating direction, which corresponds to the crystallographic a-axis. In contrast, at high coating speed the films are crystallographically less ordered but with better thin film homogeneity and exhibit isotropic electrical characteristics. Best mobilities are found in films prepared at high coating speeds with the blended semiconductor. This work demonstrates the interplay between the crystal packing and thin film morphology and uniformity and their impact on the device performance.

Introduction

The transport properties of small molecule organic semiconductors are strongly ruled by their crystal structure. Molecular crystals are characterized by weak non-directional van der Waals intermolecular interactions and hence, molecules are prone to polymorphism.[8,33,130] Many organic semiconductors such as rubrene,[131,132] acenes,[8,133,134] tetrathiafulvalenes[135–137] and oligothiophenes[138,139] have been reported to exhibit different polymorphs. Generally, the different polymorphs exhibit different charge transport behaviours when applied in organic field-effect transistors (OFETs) due to the differences in the overlap of the frontier orbitals (i.e., charge transfer integrals).[3,4] Additionally, the intrinsic anisotropy of organic crystals can also strongly influence the transport properties. Indeed, the different relative positions of neighbouring molecules in a crystal provides a variety of charge transfer integrals in the different crystallographic directions [140–

[142]. Generally, the direction that displays the strongest electronic overlap between the π-orbitals of the organic semiconductor determines the path of the maximum charge transport, although other factors such as the charge-phonons interactions play also a crucial role.[143–145] Noticeably, the crystal packing will strongly define the transport dimensionality and anisotropy in agreement with the directions where stronger intermolecular interactions are present. For instance, cofacial packings will tend to give one-dimensional (1D) electronic structures, whereas herringbone organisations will result in 2D structures.[146,147]

In organic semiconductor thin films, the conduction anisotropy is also closely connected to the morphological texture. Thin films are generally polycrystalline and depending on the experimental conditions employed to fabricate them, it is possible to prepare oriented crystal domains. While the charge transport in a polycrystalline film with randomly oriented domains will be isotropic, in a film with aligned crystallites, transport anisotropy will be expected accordingly to the molecular crystal packing.[148–153] The crystal arrangement and the morphology of organic semiconductor thin films have been found to be dependent on the substrate,[34,133] solvent and solution concentration,[154] temperature[48] and coating deposition parameters.[136,148,155–157]

The use of solution shearing deposition techniques has been shown to be a promising approach to obtain high performing thin film OFETs at low cost and on large areas. Recent studies have been devoted to the understanding of the influence of the ink formulation, temperature and deposition speed on the final thin film properties.[149,156,158–161] In particular, the latter parameter has an important impact on the crystallization and nucleation of the organic semiconductor, and hence, on its thin film morphology. At low speed the crystallization occurs in the convective regime and oriented nearly single-crystalline films can be produced because the crystallization takes place at the meniscus contact line as the solvent is evaporated. However, at higher speeds, the crystallization takes place thanks to nucleation and coalescence from a supersaturated solution and therefore more randomly oriented crystals are

formed.[136,162,163] Herein, we report on the influence of the solution shearing speed on the charge transport characteristics of thin film OFETs based on the asymmetric semiconductor 2-Decyl-7-phenyl[1]benzothieno[3,2-b][1]benzothiophene[48,164,165] (Ph-BTBT-10, Fig. 1a) and blends of this molecule with polystyrene (PS).

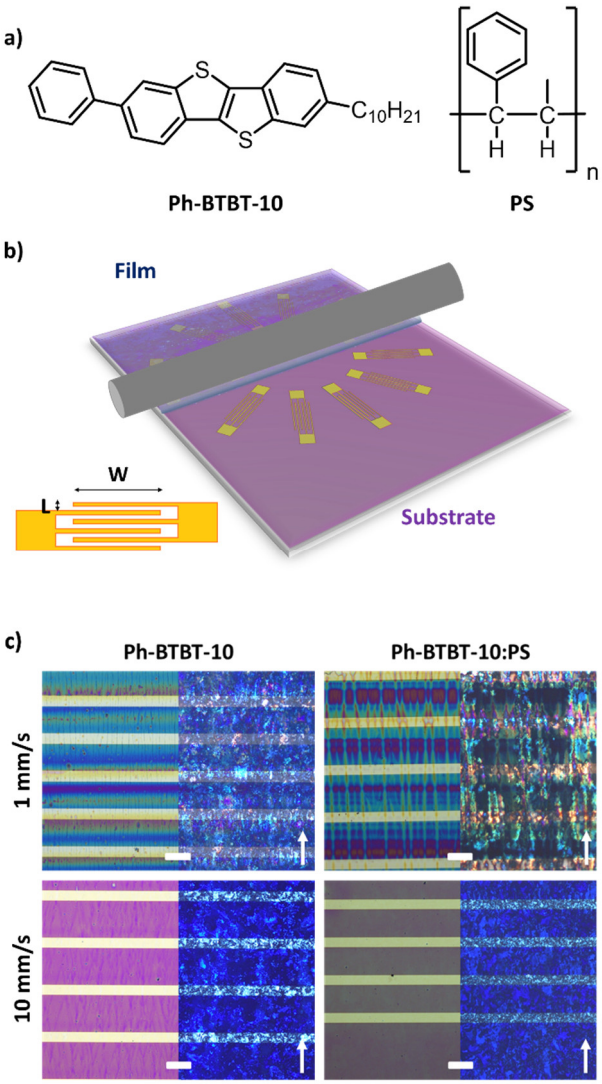

Fig. 1: a) Chemical structure of the molecule Ph-BTBT-10 and of polystyrene (PS). b) Schematic illustration of the BAMS technique together with the used electrode layout. c) Non-polarized (left) and polarized (right) microscopy images of the Ph-BTBT-10 thin films prepared from PhCl solutions. Scale bar: 100 µm. The white arrow indicates the shearing direction.

By combining in-depth X-ray diffraction studies and electrical transport characterization, we elucidate that at low coating speed the films crystallise with a preferential direction and a significant anisotropic transport is found despite the 2D herringbone packing of this semiconductor. However, electrically isotropic films are formed at high speed due to less ordered crystals. The optimum field-effect mobility is found with the blended films at high coating speed, which is attributed to the formation of more homogenous thin films.

Results and discussion

Ph-BTBT-10 has already been reported to display excellent performance as active material in single crystal and thin film OFETs.[48,164] Nevertheless, so far a post-processing thermal annealing has been reported to be essential to reach the thermodynamic bulk polymorph, also called bilayer structure, to reach a higher field-effect mobility.

In this work, thin films of Ph-BTBT-10 and blends of Ph-BTBT-10:PS were prepared by the Bar-Assisted Meniscus Shearing (BAMS) technique (Fig. 1b). This technique has previously been shown to lead to highly crystalline thin films with high throughput.[118,166] The use of polymeric blends has also been demonstrated to facilitate the processing of small molecule semiconductors and to promote an enhanced thin film crystallinity.[118,166–169] After an optimisation process of the ink formulation where different solvents, PS polymer weights and Ph-BTBT-10:PS ratios were tested (Table S1), the conditions selected were 2.0 % w/w chlorobenzene (PhCl) and 2.5 o-xylene based solutions and, in the case of blends, 280 kDa PS was chosen with a ratio Ph-BTBT-10:PS 2:1. In all the cases, the films were deposited at high temperature (i.e., 105°C) without performing a post-annealing step. Finally, to study the influence of the coating speed, the films were deposited at 1 and 10 mm/s. The polarized optical microscopy (POM) images of the films prepared from PhCl and o-xylene are shown in Fig. 1c and Fig. S1, ESI, respectively. In both cases, the films deposited at low shearing speed (1 mm/s) appear as well-oriented small stripe-shaped crystals aligned along the shearing

direction. In contrast, we observe that the films prepared at high shearing speed (10 mm/s) show a more uniform coverage without a clear preferential orientation. The only distinguishable feature between the films based on pristine Ph-BTBT-10 and Ph-BTBT-10:PS blends was the domain size, which was slightly larger for the pristine Ph-BTBT-10 film.

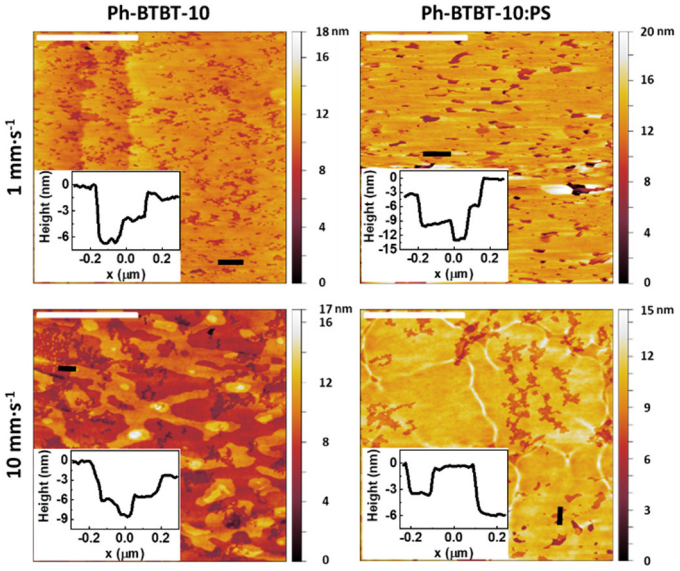

Fig. 2.: AFM topography images of Ph-BTBT-10 and Ph-BTBT-10:PS thin films deposited by BAMS using PhCl as solvent, at low and high coating speed. Scale bar: 2 µm. The insets are the high profiles along the black lines marked in the images.

The films were also characterized by atomic force microscopy (AFM) in order to determine the nanomorphology of the thin film surface (Fig. 2 and Fig S2, ESI). All the films show smooth mesoscopic areas, which exhibited a similar nanostructure. Analysing the films profile, we can observe the step edges of around 2.9±0.3 and 5.8±0.4 nm high, in agreement with Ph-BTBT-10 mono- and bilayers (the length of the molecule is ~2.6 nm), as it was previously reported by Iino et al.[48,78] Generally, the mesoscopic areas appear more uncompleted when the films are prepared at high speed, especially when the binding PS polymer is not used.

The crystallographic phase present within the films was identified by grazing incidence X-ray diffraction (GIXD) investigations. The result from a representative sample deposited from PhCl a solution is shown in Fig. 3 (see Fig. S3, ESI, for films prepared from o-xylene). The intensity distribution of the Bragg peaks within the reciprocal space map is compared to calculated structure factors of the known bulk crystal structure of Ph-BTBT-10.[147] A good agreement is found with the theoretically expected peak intensities, confirming the formation of the bulk phase of Ph-BTBT-10. Additionally, these GIXD investigations reveal that the crystallites show a preferred orientation with the crystallographic (001) plane parallel to the substrate surface. In terms of molecular packing, this means that the herringbone layers-formed by the aromatic BTBT molecular cores - are parallel to the substrate surface.

Fig. 4(top) show the specular X-ray reflectivity (XRR) curves for BAMS coated films, prepared from PhCl solutions, with and without added PS. Corresponding data for samples prepared from o-xylene solvent can be found in the Supporting Information (Fig. S4, ESI). The XRR curves show a significant dependence on the coating speed. Faster coated samples show Kiessig fringes in the range of q = 0.02 $Å^{-1}$ to 0.08 $Å^{-1}$, indicating the formation of layers with constant thicknesses. A characteristic layer thickness of 25 nm was determined. The slower coated samples do not show Kiessig fringes, which is a sign of thin films with high surface roughness. Furthermore, diffraction features are visible at q_z = 0.12 $Å^{-1}$, 0.24 $Å^{-1}$ and 0.36 $Å^{-1}$ which represent the first three orders of the 00L peak series. The alternating broadening of the 00L diffraction peaks can be explained by defects within the crystal structure.[63] The coating speed has a strong influence on the width of the diffraction peaks. The peak widths (Δq_z) of the 00±2 Bragg peaks were determined and analysed. We found values of around 0.0057 $Å^{-1}$ (0.0045 $Å^{-1}$ without PS) for the low coating speed samples, while a considerably larger peak width of 0.0170 $Å^{-1}$ (0.0185 $Å^{-1}$ without PS) is found for films prepared by high coating speeds. The peak width can be related to the vertical crystal size, values of 110 nm and 37 nm are found for the films based on blends deposited at low and high coating speeds, respectively. At low coating speeds, oscillations are observed

around the 00L Bragg peaks. Such Laue oscillations are a consequence of homogenous vertical size of the crystallites. Combining the results from the Kiessig fringes (thickness 25 nm) with the estimated length of the crystals (vertical size of 37 nm, 34 nm without PS) reveal that in case of large coating speeds the layers show homogenous thickness with continuous crystalline character.

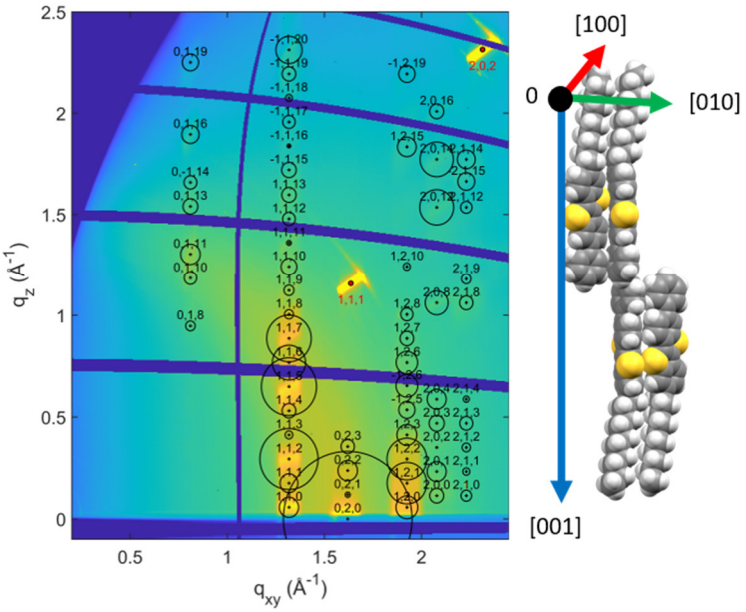

Fig. 3: Reciprocal space map of a Ph-BTBT-10 thin film prepared by BAMS from a PhCl solution without added PS using a coating velocity of 1 mm/s (left). Black markers designate peak positions of the known crystal structure, the area of the circles is proportional to the structure factor (square root of intensity) of the peaks. Red markers indicate peaks from the silicon substrate. Packing motif of the molecules relative to the crystallographic unit cell directions (right).

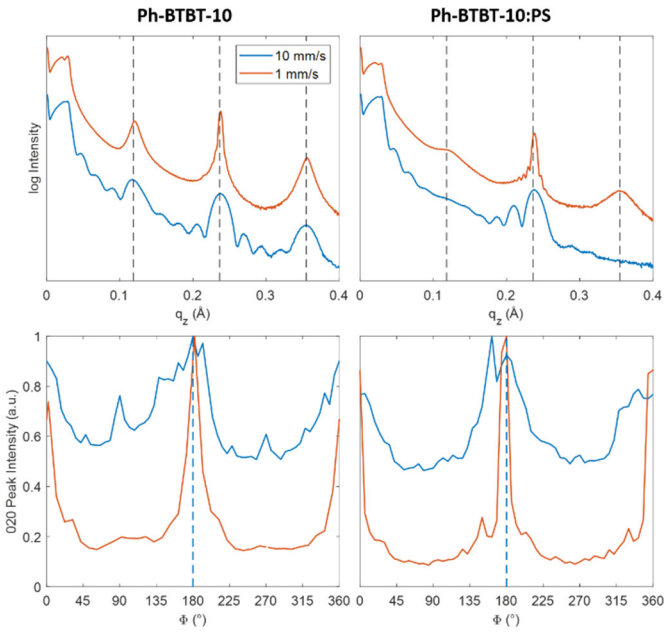

Fig. 4: X-Ray reflectivity curves of BAMS coated Ph-BTBT-10 thin films prepared from PhCl solution without (left) and with (right) PS binding polymer (top) and rotation-dependent intensity of the 0±20-peaks from GIXD with respect to the coating direction indicated by the dashed line (bottom) for different coating speeds.

For analysing the in-plane alignment of the Ph-BTBT-10 crystallites, the rotation (φ) dependence of the 0±20 peak intensities were extracted from the rotated GIXD measurements (Fig. 4 (bottom)). Two peaks can be detected, corresponding to a maximum intensity of the 0±20 peak at φ = 0° and 180° (i.e., with the primary X-ray beam parallel to the coating direction). As the scattering vector is about perpendicular to the primary X-ray beam for the 0±20 peak and diffraction occurs from crystallographic planes, where the surface normal vector has an equal direction to the scattering vector. This means for the present case that the crystals are aligned with the [010] direction perpendicular and the [100] direction parallel to the shearing direction. Additionally, these data are used to determine the influence of the coating speed on the in-plane alignment of the crystallites. For this analysis the widths (full width at half maximum) were used . Values of 9.8° and 8.4° were found at low coating speeds, for samples with and without PS,

respectively. At high coating speeds, the diffraction intensity of the 020 peak is present by a dominating constant contribution together with peaks of considerably larger peak widths of 36° and 42°, again for samples prepared with/without addition of PS. Therefore, it can be concluded that the samples prepared at the low coating speed of 1 mm/s show a considerably higher degree of crystal alignment (and thereby a smaller in-plane mosaicity) than the samples prepared at the high coating speed of 10 mm/s.

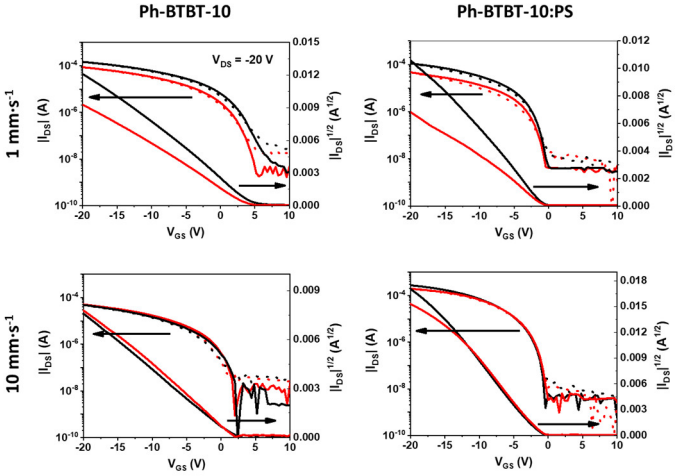

Fig. 5: Transfer characteristics in the saturation regime (VDS=-20 V) of typical Ph-BTBT-10 and Ph-BTBT-10:PS films prepared by BAMS from PhCl solutions at 1 and 10 mm/s. Continuous lines correspond to forward, while dotted lines correspond to reverse sweeps of gate voltages. Black lines correspond to devices with the channel length (L) parallel to the coating direction and red lines correspond to the perpendicular ones.

All the films were electrically characterized as active layers in OFETs under ambient conditions. Fig. 5 shows the transfer characteristics in the saturation regime for the devices based on thin films of Ph-BTBT-10 and Ph-BTBT-10:PS deposited from PhCl solutions at high and low coating speeds. In these plots the electrical characteristics of the devices measured with the channel length (L), that is the direction where the charge transport takes place, perpendicular (red) and parallel (black) to the coating direction are included. The corresponding output

characteristics are shown in Fig. S5, ESI and the electrical characteristics of devices prepared from o-xylene are displayed in Fig. S6, ESI and Fig. S7, ESI. All the devices exhibit p-type OFET characteristics with low hysteresis. In general, the devices based on films of Ph-BTBT-10 reveal threshold voltages (V_{TH}) positively shifted with respect to the ones based on the semiconductor blend (see Table S1, ESI). This can be indicative to some unintentional doping. Regarding the electrical anisotropy, we find that while no appreciable differences between the parallel and perpendicular devices are observed in the films coated at high speed, clearly the films coated at low speed display distinct characteristics depending on the measurement direction. In fact, the devices with L parallel with the solution shearing direction exhibit a higher source-drain current (I_{SD}). Such observed anisotropy at low coating speed is in agreement with the fact that aligned crystals are formed in these conditions.

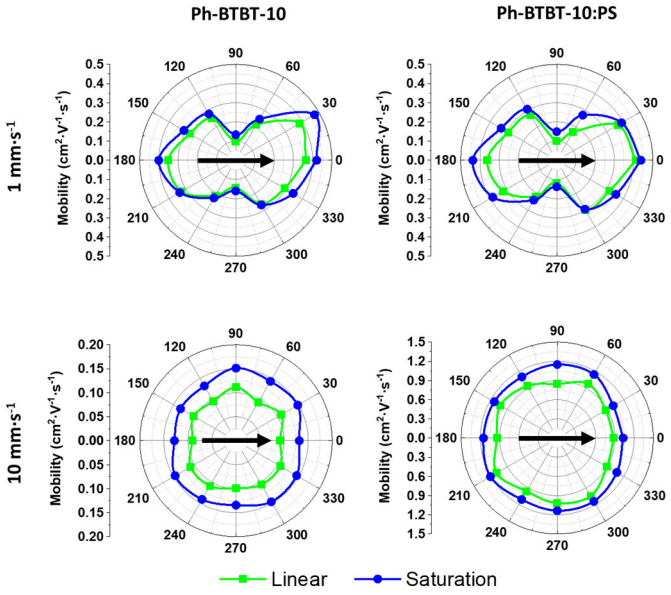

Fig. 6: Polar plot of the linear and saturation mobility of the Ph-BTBT-10 and Ph-BTBT-10:PS films prepared from PhCl solutions at low and high coating speed. The angle corresponds to the conducting channel L with respect to the coating direction. The direction of the solution shearing is indicated with a black arrow.

In order to better evaluate the field-effect mobility of the devices along different thin film directions, OFETs with electrodes with star-oriented layout were

fabricated (see Fig. 1b). In Fig. 6 (and Fig. S8, ESI for devices deposited from o-xylene) the mobility of the devices is plotted as a function of the angle between L (i.e., charge-transport path) and the coating direction. At low coating speed, the highest mobility is found when the device channel L is parallel with respect to the coating direction, achieving a mobility of 0.48 and 0.43 $cm^2/V{\cdot}s$ for Ph-BTBT-10 and Ph-BTBT-10:PS films, respectively. On the other hand, the lowest mobility value was found to be 0.14 $cm^2/V{\cdot}s$ for both films in the perpendicular direction. Thus, the anisotropy ratio was estimated to be in the range 3.3-3.7 for Ph-BTBT-10 films and 2.9-3.2 for the Ph-BTBT-10:PS ones. Taking into account the X-ray results, we can affirm that the maximum mobility is thus achieved along the a-axis of the crystal structure. This is fully in accordance with the theoretical work recently reported by Baggioli et al.[16] In this work the authors show that within the herringbone plane, the maximum mobility is found along the a-axis with an anisotropy ratio of around 2. The higher anisotropy ratio found here experimentally can be due to the influence of the intergrain boundaries.

Considering the devices deposited at high shearing speed, a quasi-ideal electrical isotropy was found (ratio $\mu_{||}/\mu_{\perp}$~1). Thin films of Ph-BTBT-10:PS displayed the highest mobility of 1.46 $cm^2/V{\cdot}s$ (1.3±0.1 $cm^2/V{\cdot}s$ on average), while the mobility of the films based on only the organic semiconductor was 0.22 $cm^2/V{\cdot}s$ (0.16±0.05 $cm^2/V{\cdot}s$ on average). It is worth noticing that the use of blends is significantly enhancing the device mobility of the films deposited at high coating speed to almost one order of magnitude. It is known that the viscosity of the ink solutions promotes the formation of more homogenous films, which is particularly important when the films are deposited at high shearing speed. Remarkably, the high isotropic mobility achieved with the blends at high speed is between 2 and 3 times higher than the best one found for the preferentially aligned crystallites obtained at low coating speed. This implies that not only the intermolecular interactions are playing a role but also the thin film morphology. This agrees with the XRR results which indicated that the films coated by high speed are homogenous with a constant film thickness.

The main difference observed between the films prepared from PhCl or o-xylene was the electrical isotropy/anisotropy. At low shearing speed, o-xylene films reveal a lower anisotropy ratio of 1.7-2.0 for Ph-BTBT-10 films and 2.0-2.3 for the Ph-BTBT-10:PS ones. Further, in the films prepared at high speed a small anisotropy ratio was found in the range 1.1-1.3 for both Ph-BTBT-10 and Ph-BTBT-10:PS films. Therefore, the ideal isotropy behaviour was only possible to obtain using PhCl as solvent.

Experimental

Solution Preparation: Ph-BTBT-10 and PS 10000 g/mol and 280000 g/mol (PS10 and PS280) were purchased from TCI Chemical Industry and Sigma-Aldrich, respectively, and used without further purification. Solutions of Ph-BTBT-10 and Ph-BTBT-10:PS were prepared in chlorobenzene and o-xylene with a final concentration of 2.0 and 2.5 % w/w, respectively. Before to solution deposition, the solutions were heated at the substrate temperature used for the coating process.

Materials and Device Fabrication. Interdigitated electrodes were patterned by photolithography on heavily n-doped Si wafer (Si-Mat) with a 200 nm thick layer of SiO_x. Subsequently, a Cr (5 nm)/Au (40 nm) layer was deposited by thermal evaporation. The channel lengths (L) varied from 25 to 200 µm and the channel width/length ratio was always set constant to 100. Substrates were cleaned by sonication in HPLC grade acetone and isopropanol and then dried under nitrogen. The gold electrodes were chemically modified with a self-assembled monolayer of 2,3,4,5,6-Pentafluorothiophenol (PFBT). For this, the gold electrodes were first activated with an ultraviolet ozone generator for 25 min and then immersing in a 15 mM solution of PFBT in isopropanol for 15 min. Finally, the substrates were washed with pure isopropanol to remove the PFBT excess. The Ph-BTBT-10 films were then deposited by Bar-Assisted Meniscus Shearing (BAMS) as previously reported.[63] The solution shearing deposition was carried out at a substrate temperature of 105 °C and with coating speed of 1 and 10 mm/s. Note that

all the fabrication process was carried out under ambient conditions and no post-thermal treatments were required.

Thin-Film Characterization. The optical microscopy images were taken using an Olympus BX51 equipped with polarizer and analyser. Surface topographies were examined by a 5500LS SPM system from Agilent Technologies and subsequent data analysis was performed by using Gwyddion 2.56 software.

X-Ray Reflectivity (XRR) measurements were carried out with a PANalytical Empyrean diffractometer in θ-θ geometry using CuKα radiation. On the incident side a parallel beam X-ray mirror was used for monochromatization. At the diffracted beam path an anti-scatter slit as well as a 0.02 rad Soller slit was used together with a PIXcel3D detector operating in receiving 0D-mode. The data is converted into reciprocal space by $q = \frac{4\pi}{\lambda} sin\left(\frac{2\theta}{2}\right) = \frac{2\pi}{d_{hkl}}$ with λ as the wavelength of the primary X-ray beam, 2θ the scattering angle and d_{hkl} the interplanar distance of the (hkl) plane. Crystal sizes was determined by the Scherrer equation using $D_z = \frac{2\pi}{\Delta q_z}$ with D_z as the vertical crystal size and Δq_z as the peak width.

Rotated grazing incidence X-Ray diffraction (GIXD) was measured at the beamline XRD1 at Elettra Synchrotron Trieste with an X-ray radiation wavelength of 1.40 Å using an incidence angles, varied between α_i = 0.2° up to 3.0° on a goniometer in Kappa geometry[54]. A φ – rotation of the samples was performed around the substrate surface normal. Care was taken to place every sample of the series with the coating direction along the X-ray beam, defining a defined azimuthal alignment of the samples (φ = 0°). The sample rotation was carried out with a step width of 6° integrating the intensity for 5 s for each image. A PILATUS 2M detector was used to collect the diffracted intensity. The experimental data were evaluated with the in-house developed software GIDVis[55]. The components of the scattering vector (q_x, q_y, q_z) scattering vector components are determined for each detector pixel from the incident angle α_i and the outgoing angle αf in the

sample coordinate system by using a calibration measurement from an LaB_6 film. Data from GIXD measurements are presented as reciprocal space maps by summing up the intensities of a full rotation of 360°. Finally, the intensity is plotted as a function of the out-of-plane (q_z) and in-plane component (q_{xy}) of the scatting vector with $q_{xy}^2 = q_x^2 + q_y^2$. A second method is used for presenting the GIXD data. The intensities of a selected area around the 020 peak of each individual reciprocal space maps are integrated and plotted as a function of the rotation angle φ.

Device Characterization. The transfer and output characteristics of the devices were measured with an Agilent B1500A semiconductor device analyser connected to the samples with a Karl SÜSS probe station, at ambient conditions. The characteristic field-effect mobility (μ) and threshold voltage (V_{TH}) parameters of the transistors were extracted in the lineal and saturation regime using the following classic MOSFETs equations:

$$\mu^{lin} = \frac{\partial I_{DS}}{\partial V_G}\frac{L}{W}\cdot\frac{1}{C}\cdot\frac{1}{V_{DS}} \quad (1) \qquad \mu^{sat} = \left(\frac{\partial\sqrt{I_{DS}}}{\partial V_G}\right)^2\frac{2L}{W}\cdot\frac{1}{C} \quad (2)$$

where W and L are the width and length of the channel, respectively, C is capacitance per unit area of the dielectric (C = 17.26 nF/cm^2), I_{DS} the measured source-drain current, V_{DS} the source-drain current and V_G the applied gate voltage.

Conclusions

To sum up, thin films of the organic semiconductor Ph-BTBT-10 and blends of it with PS have been prepared by a solution shearing technique at two deposition speeds: 1 mm/s (low) and 10 mm/s (high). Chlorobenzene as well as o-xylene were used as solvents. In all the cases, the organic semiconductor crystallised in the bulk phase following a 2D herringbone arrangement. Further, all the films exhibited a p-type field-effect behaviour when implemented in OFETs. However, clear

differences in the performance were observed due to influence of the coating speed on the crystallization and thin film morphology/uniformity.

At low coating speed, films grow with the a-axis aligned with the coating direction, where the maximum field-effect mobility is found. The thin film electrical anisotropy in the films is in the range 3 – 4 for chlorobenzene and 1.5 – 2.5 for o-xylene. This is larger than what was theoretically expected for a single crystal (especially in the films without PS) which can be explained by the impact of the intergrains. In sharp contrast, the crystals in the films coated at high speed are not aligned in the ab plane and, accordingly, they exhibit isotropic charge transport mobilities. Remarkably, the blended films reveal a high mobility of 1.3 $cm^2/V{\cdot}s$ and 1.0 cm^2/Vs when they were prepared from chlorobenzene or o-xylene solutions, respectively.

This work elucidates that the coating speed has a strong impact on the thin film crystallisation and thin film morphology, both features play a crucial role in determining the final device performance.

The Supporting Information gives an overview on the comprehensive approach of the experimental work. In a first step thin film transistors were fabricated by wide variation of the organic film preparation conditions. Five different solvents with and without blending of the Ph-BTBT-10 solution with polystyrene (with variation of blending ratios and molecular weight) were used; two different coating speeds were applied. The respective device performances are listed within **Table S1**. Based on these results we decided to perform detailed work on thin films prepared by solutions from chlorobenzene and from o-xylene.

The experimental results of both type of device series are discussed in the main paper. Due to limited space, only the results on chlorobenzene based system are depicted as figures in the main paper. The corresponding results on the systems prepared from o-xylene solutions are given here: **Figure S1** presents optical microscopy images with and without polarized light; **Figure S2** the mesoscopic morphology by AFM images; **Figure S3** a reciprocal space map of a representative sample calculated from GIXD experiments; **Figure S4** X-ray reflectivity (XRR) curves and φ-scans of the 0±20 peak; **Table S2** the observed peak widths of the specular diffraction peak measurements; **Figure S6** and **Figure S7** the transfer and output characteristics of the devices, respectively and **Figure S8** the orientation dependence of the charge transport mobility. The only result on chlorobenzene transistors within the Supporting Information are the output characteristics presented in **Figure S5**.

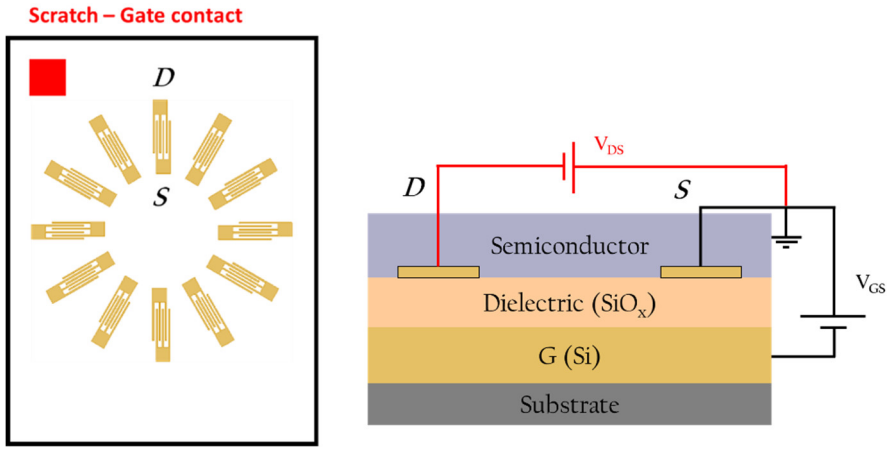

Scheme 1. OFET structure used in this work.

Table S1. Average of main OFET parameters measured and its standard deviation extracted from transfer characteristics for the fabricated devices. At least 42 devices were prepared for each specific experimental condition. The selected conditions are highlighted in bold.

			Coating speed: 1 mm/s		Coating speed: 10 mm/s	
Solvent	OSC:PS Ratio	PS Molecular Weight ($kg \cdot mol^{-1}$)	Mobility ($cm^2 \cdot V^{-1} \cdot s^{-1}$)	Threshold Voltage (V)	Mobility ($cm^2 \cdot V^{-1} \cdot s^{-1}$)	Threshold Voltage (V)
o-xylene	1:0	-	0.4 ± 0.2	4 ± 2	0.5 ± 0.2	2 ± 1
	4:1	10	0.4 ± 0.1	-1 ± 2	0.4 ± 0.2	0 ± 1.
	2:1	280	0.6 ± 0.3	-1.2 ± 0.8	1.0 ± 0.2	-0.7 ± 0.4
chlorobenzene	1:0	-	0.42 ± 0.09	2 ± 1	0.16 ± 0.05	0 ± 2
	4:1	10	1.03 ± 0.06	-1.9 ± 0.3	0.67 ± 0.07	-0.9 ± 0.2
	4:1	280	0.40 ± 0.08	-1.1 ± 0.2	0.9 ± 0.2	-0.8 ± 0.2

	2:1	280	0.4 ± 0.1	-1.5 ± 0.5	1.3 ± 0.07	-0.6 ± 0.3
	1:2	280	0.06 ± 0.05	-4 ± 2	0.04 ± 0.01	-10 ± 3
anisole	1:0	-	0.002 ± 0.001	2 ± 4	0.03 ± 0.01	0.4 ± 0.9
	4:1	10	0.04 ± 0.03	2 ± 2	0.9 ± 0.3	-1.1 ± 0.6
o-dichlorobenzene	1-0	-	0.23 ± 0.09	3 ± 1	0.012 ± 0.004	-9 ± 3
	4:1	10	0.31 ± 0.06	0.3 ± 0.9	0.32 ± 0.06	-1.1 ± 0.5
decalin	1:0	-	0.5 ± 0.2	7 ± 2	0.07 ± 0.03	8 ± 4
	4:1	10	0.3 ± 0.1	2 ± 3	0.35 ± 0.06	4 ± 3

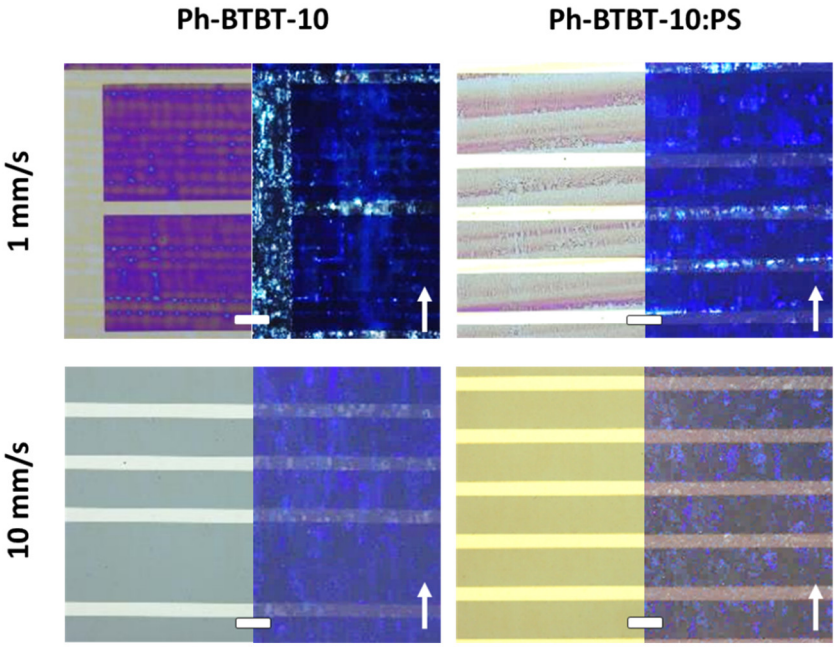

Fig. S1. Non-polarized (left) and polarized (right) microscopy images of the Ph-BTBT-10 thin films prepared from o-xylene. Scale bar: 100 µm. The white arrow indicates the shearing direction.

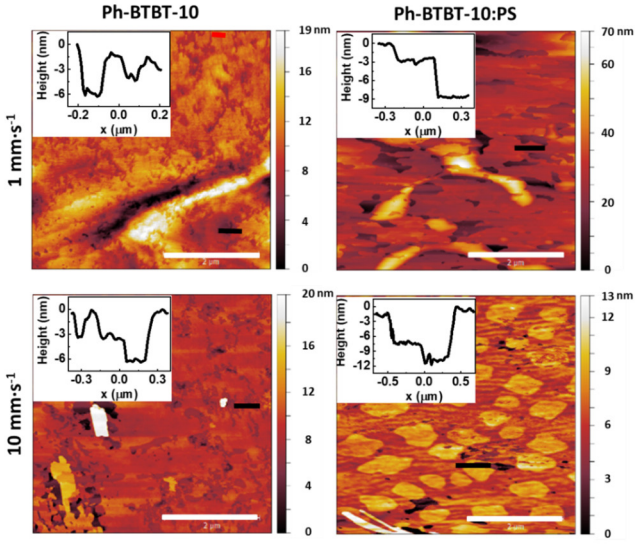

Fig. S2. AFM topography images of Ph-BTBT-10 and Ph-BTBT-10:PS blend thin films deposited by BAMS, using o-xylene as solvent, at low and high coating speed. Scale bar: 2 µm. Inset: high profiles extracted along the black line of the images.

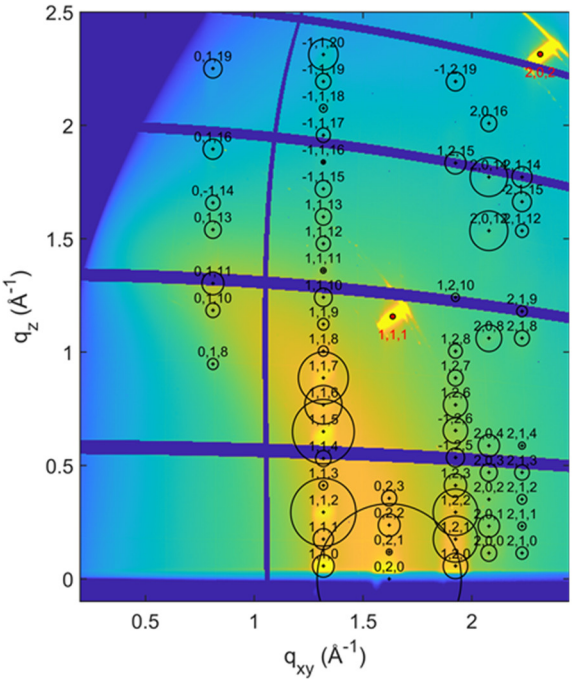

Fig. S3. Reciprocal space map of a Ph-BTBT-10 thin film prepared by bar assisted shear coating from o-xylene solution without added PS using a coating velocity of 1 mm/s. Black markers designate peak positions of the known crystal structure (bulk phase), the area of the circles is proportional to the structure factor of the peaks. Red markers indicate peaks from the Si substrate.

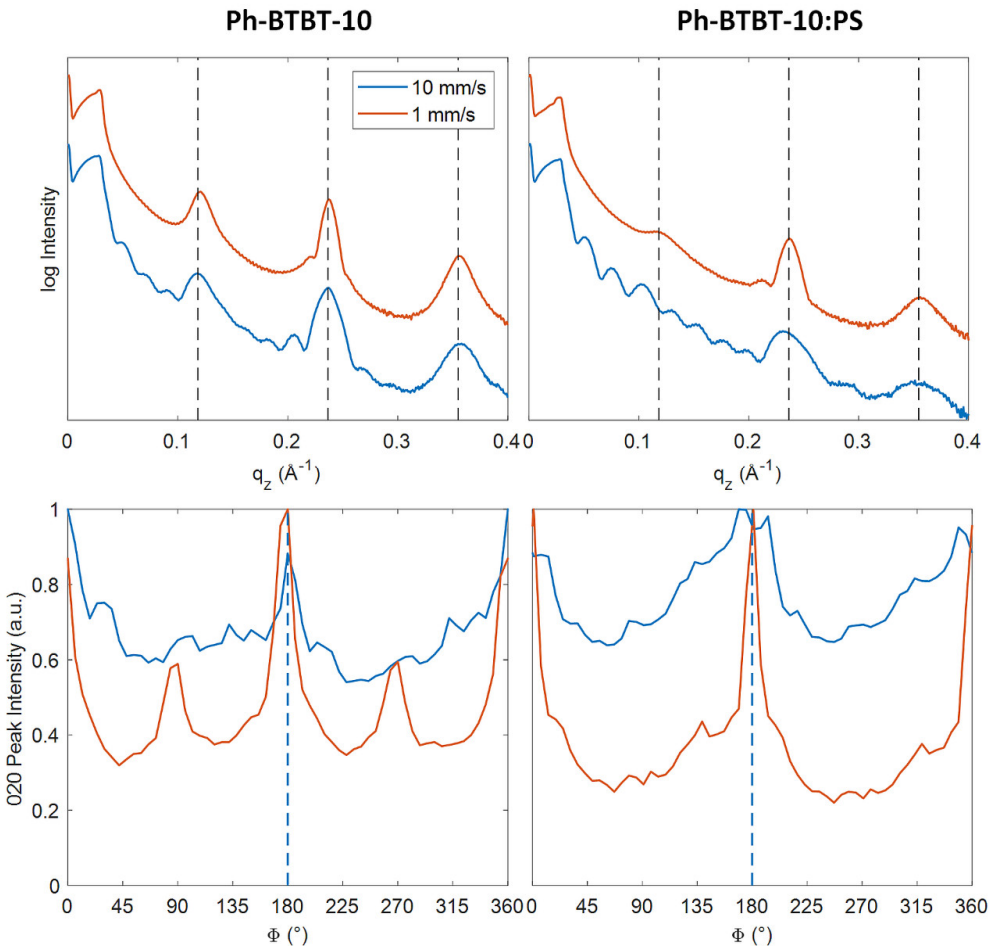

Fig. S4. X-Ray reflectivity curves of BAMS coated Ph-BTBT-10 thin films prepared from o-xylene solution without (left) and with (right) PS blend (top), Kiessig fringes reveal homogenous films with a constant film thickness of 25 nm. Rotation-dependent intensity of the 0±20-peaks from GIXD with respect to the angle measured between the coating direction axis and the conducting channel, indicated by the dashed line (bottom) for different coating speeds.

Table S2: Summary of 002 peak parameters and corresponding vertical crystal size for shear coated Ph-BTBT-10 thin films prepared from o-xylene solution, together with the in-plane mosaicity of the 020 Bragg peak.

	002 Peak Width [Å^{-1}]	Vertical Crystal Size [nm]	In-plane alignment FWHM [°]
10 mm/s Ph-BTBT-10	0.0145	43	50
1 mm/s Ph-BTBT-10	0.0091	69	18
10 mm/s Ph-BTBT-10:PS	0.0260	24	46
1 mm/s Ph-BTBT-10:PS	0.0123	51	16

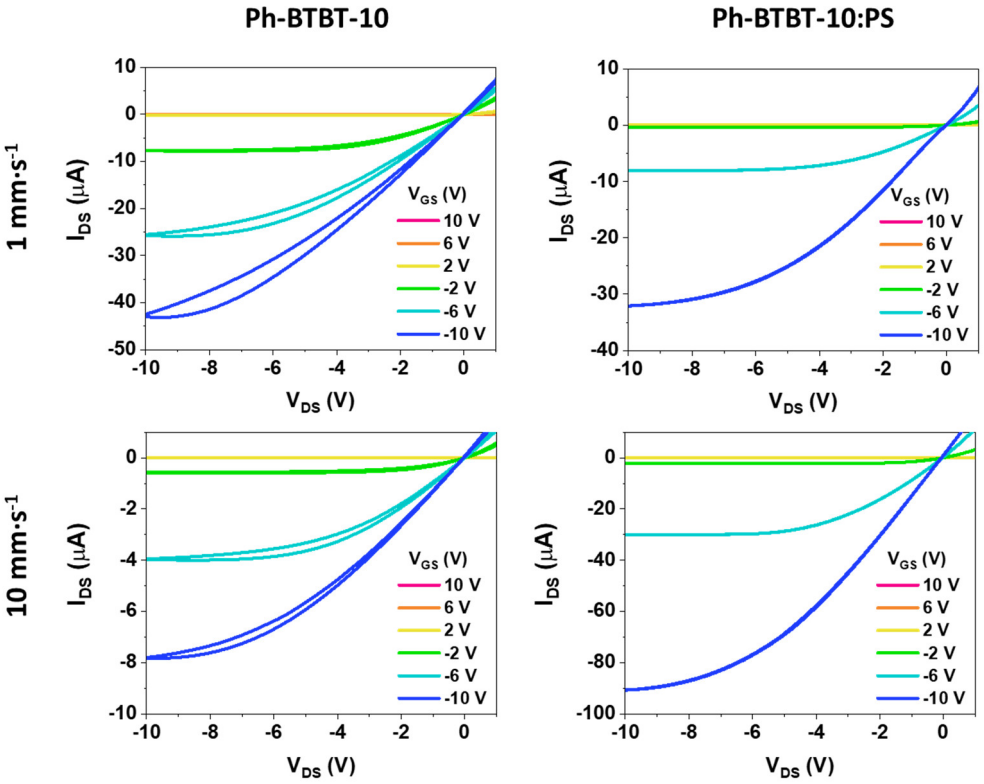

Fig. S5. Output characteristics of the OFETs based on Ph-BTBT-10 and Ph-BTBT-10:PS deposited from PhCl solutions at 1 mm/s and 10 mm/s.

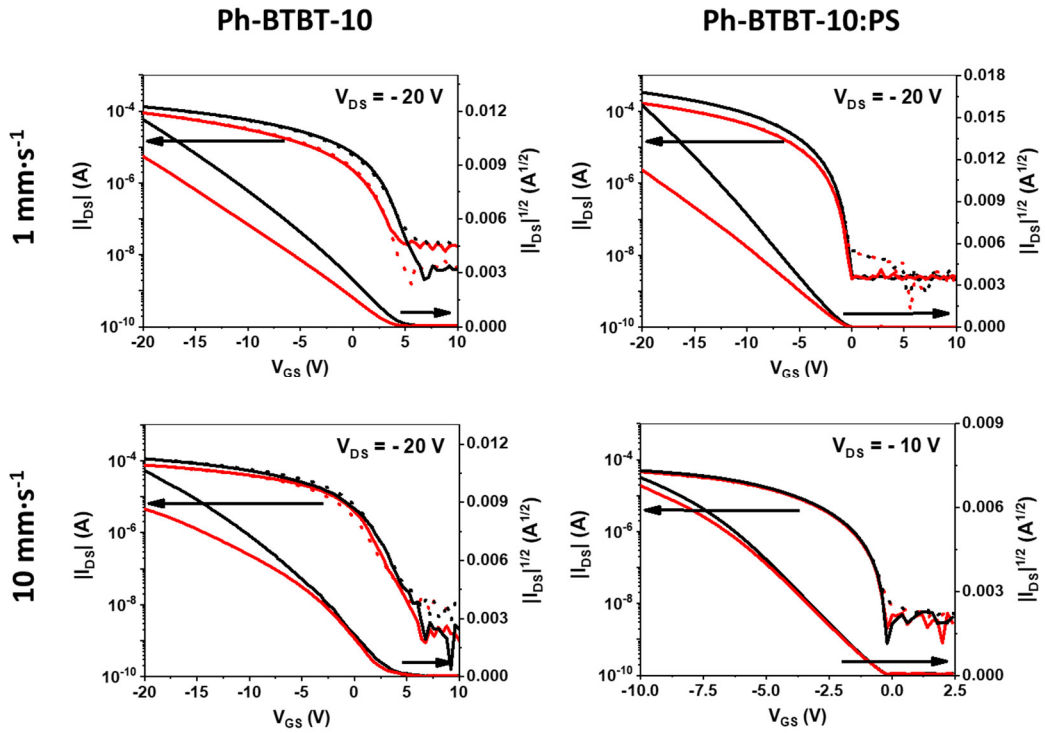

Fig. S6. Transfer characteristics in the saturation regime of typical Ph-BTBT-10 and Ph-BTBT-10:PS films prepared by BAMS from o-xylene solutions at 1 and 10 mm/s. Continuous lines correspond to forward, while dotted lines correspond to reverse sweeps of gate voltages. Black lines correspond to devices with the channel length (L) parallel to the coating direction and red lines correspond to the perpendicular ones.

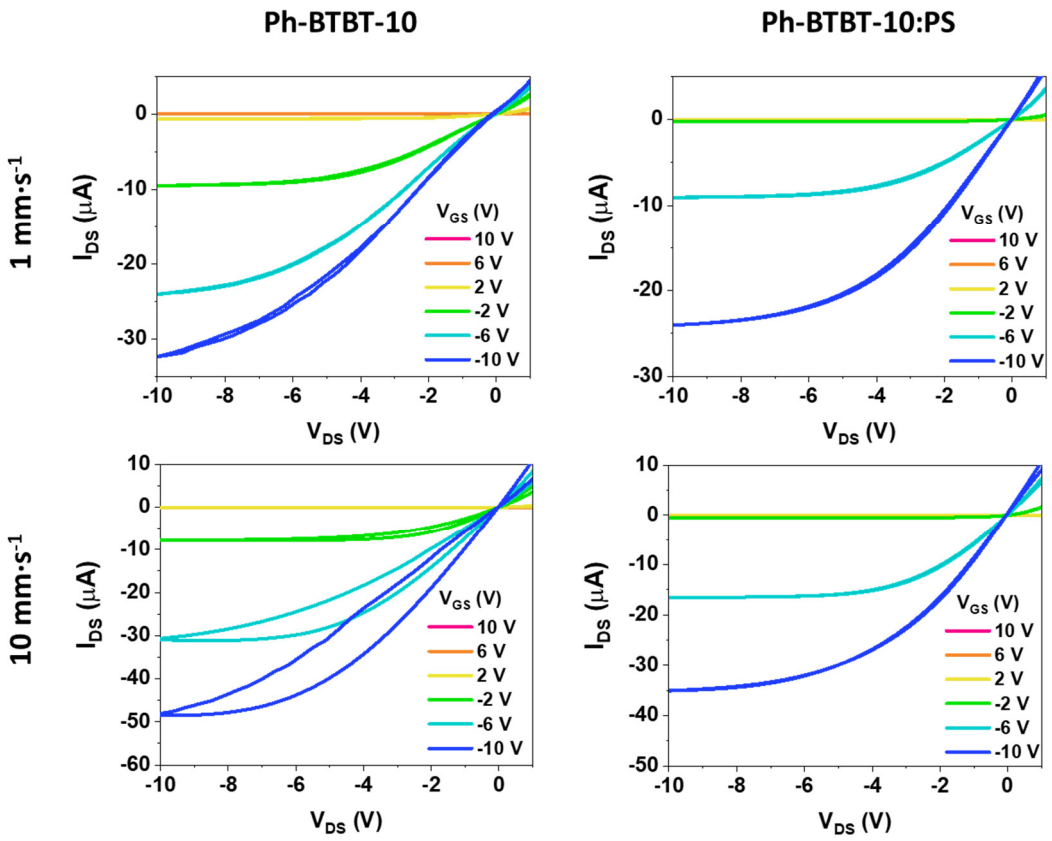

Fig. S7. Output characteristics of the OFETs based on Ph-BTBT-10 and Ph-BTBT-10:PS deposited from o-xylene solutions at 1 mm/s and 10 mm/s.

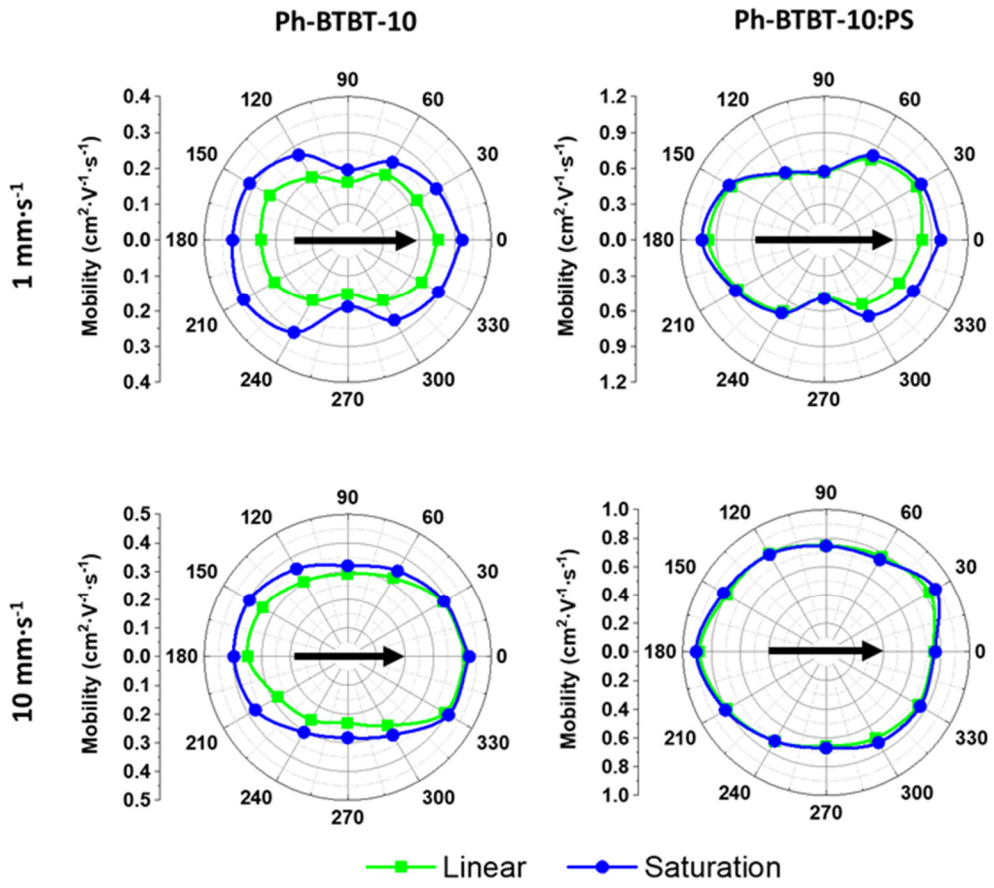

Fig. S8. Polar plot of the linear and saturation mobility of the Ph-BTBT-10 and Ph-BTBT-10:PS films prepared from o-xylene solutions at low and high coating speed (angle of the conducting channel L with respect to the coating direction). The direction of the solution shearing is indicated with a black arrow and the L of the devices were 100 µm.

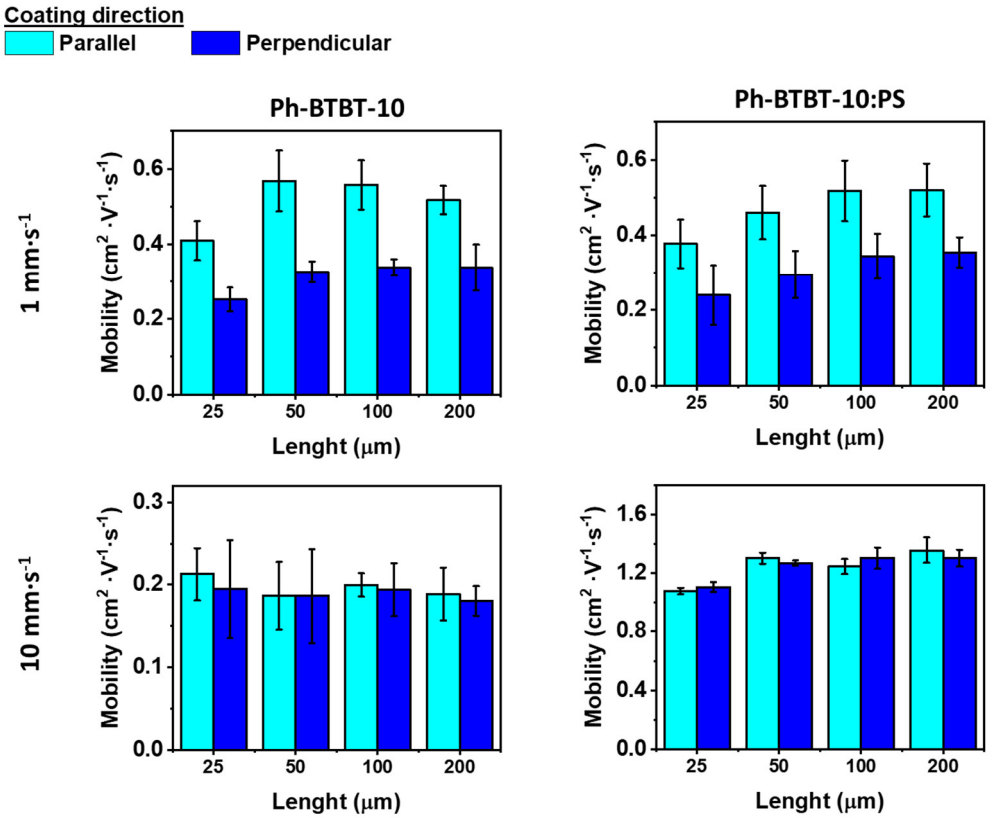

Fig. S9. Bar graph comparing the saturation mobility of Ph-BTBT-10 and Ph-BTBT-10:PS films in parallel and perpendicular orientations with respect to the coating speed. The films were prepared from chlorobenzene solutions at low and high coating speed.

Author Contributions

The manuscript was written through contributions of all authors. / All authors have given approval to the final version of the manuscript. / ‡These authors contributed equally.

Conflicts of interest

The authors declare no conflict of interest.

Acknowledgements

The authors also thank the European Union's Horizon 2020 research and innovation programme under the Marie Skłodowska-Curie grant agreement No 811284 (UHMob), the Spanish Ministry project GENESIS PID2019-111682RB-I00, the "Severo Ochoa" Programme for Centers of Excellence in R&D (FUNFUTURE, CEX2019-000917-S) and the Generalitat de Catalunya (2017-SGR-918) and the Austrian Science Fund (FWF): [P30222]. A. T. thanks his enrolment in the Materials Science PhD program of Universitat Autònoma de Barcelona and acknowledge FPU fellowship from the Spanish Ministry. We thank the synchrotron Elettra, Trieste for provision of synchrotron radiation and Luisa Barba for her support to use the beamline XRD1.

4.5 Other Publications

Further publication where the author of this thesis was involved in terms of using methods as described above or in the writing of the manuscript:

J. Simbrunner, S. Hofer, B. Schrode, Y. Garmshausen, S. Hecht, R. Resel & I. Salzmann, *Indexing grazing-incidence X-ray diffraction patterns of thin films: lattices of higher symmetry,* J. Appl. Cryst., (2019), 52, 428-439.

Available at: https://doi.org/10.1107/S1600576719003029

J. Simbrunner, B. Schrode, S. Hofer, J. Domke, T. Fritz, R. Forker & R. Resel, *Searching for New Polymorphs by Epitaxial Growth,* J. Phys. Chem. C., (2021), 125 (1), 618-626

Available at: https://doi.org/10.1021/acs.jpcc.0c10021

M. P. Kainz, L. Legenstein, V. Holzer, S. Hofer, M. Kaltenegger, R. Resel & J. Simbrunner, *GIDInd: an automated indexing software for grazing-incidence X-ray diffraction data, J. Appl. Cryst.,* Accepted: 24. June 2021

S. Bhagat, W. D. Leal, M. B. Majewski, J. Simbrunner, S. Hofer, R. Resel, I. Salzmann, *Aggregate formation in crystalline blends of α-sexithiophene and para-sexiphenyl, Accepted*

5. Conclusion

This thesis presents an in-dept study of the organic semiconductor Ph-BTBT-10, investigated via X-ray based methods and computational modeling. Methods are presented where structural information is resolved, even though the diffraction signal is very limited. Especially when dealing with liquid crystalline systems it becomes apparent that an expansion of conventional scattering techniques with modeling allows for further insights into the materials properties. In a further example a polymorphic phase with a very interesting growth behavior is characterized where the growth is not mediated due to the substrate interactions but due to cross nucleation in thicker films. Also, in those situations a combined approach where diffraction data is extended with computational methods is used to resolve a structure, far away from thermodynamical equilibrium. In a more fundamental word, a specific type of order is described, that occurs due to the anisotropy in the shape of the molecule. As X-ray based techniques always measure integrative over the whole sample and map the periodic structures, the defects and deviations from the orders structure can rarely be accessed. By careful modeling, this thesis presents a case where disorder can be measured, actually be quantified and be correlated back to the preparation conditions, revealing the influence of the preparation on the order in the film. A last example is studied, where the application of the molecule Ph-BTBT-10 as a thin film transistor material is analyzed. Charge transport characteristics and their anisotropies are measured and connected to the crystallographic structure, thus revealing the paths that charges can easily take in the molecular system. The model system Ph-BTBT-10 was chosen due to the promising thin film transistor performance, but the methods here can be extended to any molecular system. It has been shown that

molecular dynamics is a powerful tool to support careful diffraction experiments and the measured data can be readily input into the simulations. As indexation of GIXD data can only provide the crystallographic unit cell, molecular dynamics proves to be an excellent additional method to tackle the problem of structure solutions from thin films.

Bibliography

1 E. Bauer, *Zeitschrift fur Krist. - New Cryst. Struct.*, 1958, **110**, 395–431.

2 H. Lüth, *Solid surfaces, interfaces and thin films*, Springer, 2001, vol. 4.

3 J. L. Brédas, J. P. Calbert, D. A. Da Silva Filho and J. Cornil, *Proc. Natl. Acad. Sci. U. S. A.*, 2002, **99**, 5804–5809.

4 C. Winkler, A. Jeindl, F. Mayer, O. T. Hofmann, R. Tonner and E. Zojer, *Chem. Mater.*, 2019, **31**, 7054–7069.

5 D. Nabok, P. Puschnig, C. Ambrosch-Draxl, O. Werzer, R. Resel and D. M. Smilgies, *Phys. Rev. B - Condens. Matter Mater. Phys.*, 2007, **76**, 1–6.

6 J. Bernstein, *Polymorphism in Molecular Crystals*, Clarendon Press, 2002.

7 A. J. Cruz-Cabeza, N. Feeder and R. J. Davey, *Commun. Chem.*, 2020, **3**, 10–13.

8 H. Chung and Y. Diao, *J. Mater. Chem. C*, 2016, **4**, 3915–3933.

9 S. Schiefer, M. Huth, A. Dobrinevski and B. Nickel, *J. Am. Chem. Soc.*, 2007, **129**, 10316–10317.

10 R. Resel, A. O. F. Jones, G. Schweicher, R. Fischer, N. Demitri and Y. H. Geerts, *IUCrJ*, 2018, **5**, 304–308.

11 S. Ogawa, *Organic Electronics Materials and Devices*, 2015.

12 H. Iino, T. Usui and J. Hanna, *Nat. Commun.*, 2015, **6**, 6828.

13 K. Takimya, I. Osaka, T. Mori and M. Nakano, *Acc. Chem. Res.*, 2017, **47**, 1493−1502.

14 H. Minemawari, J. Tsutsumi, S. Inoue, T. Yamada, R. Kumai and T.

Hasegawa, *Appl. Phys. Express*, 2014, **7**, 091601.

15 G. R. Desiraju and A. Gavezzotti, *Acta Crystallogr. Sect. B*, 1989, **45**, 473–482.

16 A. Baggioli, M. Casalegno, G. Raos, L. Muccioli, S. Orlandi and C. Zannoni, *Chem. Mater.*, 2019, **31**, 7092–7103.

17 M. Yoneya, *J. Phys. Chem. C*, 2018, **122**, 22225–22231.

18 M. Yoneya, *Jpn. J. Appl. Phys.*,2020, **59**, 090909 , DOI:10.35848/1347-4065/abb00e.

19 S. Kim, A. Kim, K. S. Jang, S. Yoo, J. W. Ka, J. Kim, M. H. Yi, J. C. Won, S. K. Hong and Y. H. Kim, *Synth. Met.*, 2016, **220**, 311–317.

20 W. Friedrich, P. Knipping and M. Laue, *Ann. Phys.*, 1913, **346**, 971–988.

21 W. H. Bragg, W. L. Bragg, *Proc. R. Soc. London. Ser. A, Contain. Pap. a Math. Phys. Character*, 1913, **88**, 428–438.

22 P. J. Brown, A. G. Fox, E. N. Maslen, M. A. O'Keefe and B. T. M. Willis, *Int. Tables Crystallogr.*, 2006, **C**, 554–595.

23 J. W. Goodby, P. J. Collings, T. Kato, C. Tschierske, H. Gleeson, P. Raynes and V. Vill, *Handbook of Liquid Crystals, 8 Volume Set*, Wiley, 2014.

24 Y. Yamamura, T. Adachi, T. Miyazawa, K. Horiuchi, M. Sumita, M. Massalska-Arodź, S. Urban and K. Saito, *J. Phys. Chem. B*, 2012, **116**, 9255–9260.

25 J. W. Goodby, R. J. Mandle, E. J. Davis, T. Zhong and S. J. Cowling, *Liq. Cryst.*, 2015, **42**, 593–622.

26 D. Frenkel and B. Smit, *Understanding Molecular Simulation: From Algorithms to Applications*, Elsevier Science, 2001.

27 J. Als-Nielsen and D. McMorrow, *Elements of Modern X-ray Physics: Second Edition*, 2011.

28 L. G. Parratt, *Phys. Rev.*, 1954, **95**, 359–369.

29 M. Björck and G. Andersson, *J. Appl. Crystallogr.*, 2007, **40**, 1174–1178.

30 M. Svechnikov, *J. Appl. Crystallogr.*, 2020, **53**, 244–252.

31 J. S. Pedersen and I. W. Hamley, *Phys. B Phys. Condens. Matter*, 1994,

198, 16–23.

32 S. M. Danauskas, D. Li, M. Meron, B. Lin and K. Y. C. Lee, *J. Appl. Crystallogr.*, 2008, **41**, 1187–1193.

33 D. Gentili, M. Gazzano, M. Melucci, D. Jones and M. Cavallini, *Chem. Soc. Rev.*, 2019, **48**, 2502–2517.

34 A. O. F. Jones, B. Chattopadhyay, Y. H. Geerts and R. Resel, *Adv. Funct. Mater.*, 2016, **26**, 2233–2255.

35 B. Wedl, R. Resel, G. Leising, B. Kunert, I. Salzmann, M. Oehzelt, N. Koch, A. Vollmer, S. Duhm, O. Werzer, G. Gbabode, M. Sferrazza and Y. Geerts, *RSC Adv.*, 2012, **2**, 4404–4414.

36 L. Pithan, D. Nabok, C. Cocchi, P. Beyer, G. Duva, J. Simbrunner, J. Rawle, C. Nicklin, P. Schäfer, C. Draxl, F. Schreiber and S. Kowarik, *J. Chem. Phys.*, , DOI:10.1063/1.5043379.

37 C. Lercher, C. Röthel, O. M. Roscioni, Y. H. Geerts, Q. Shen, C. Teichert, R. Fischer, G. Leising, M. Sferrazza, G. Gbabode and R. Resel, *Chem. Phys. Lett.*, 2015, **630**, 12–17.

38 Y. Yuan, G. Giri, A. L. Ayzner, A. P. Zoombelt, S. C. B. Mannsfeld, J. Chen, D. Nordlund, M. F. Toney, J. Huang and Z. Bao, *Nat. Commun.*, 2014, **5**, 1–9.

39 A. O. F. Jones, Y. H. Geerts, J. Karpinska, A. R. Kennedy, R. Resel, C. Röthel, C. Ruzié, O. Werzer and M. Sferrazza, *ACS Appl. Mater. Interfaces*, 2015, **7**, 1868–1873.

40 T. Siegrist, C. Kloc, J. H. Schön, B. Batlogg, R. C. Haddon, S. Berg and G. A. Thomas, *Angew. Chemie - Int. Ed.*, 2001, **40**, 1732–1736.

41 D. Kashchiev and K. Sato, *J. Chem. Phys.*, 1998, **109**, 8530–8540.

42 P. M. Piaggi and M. Parrinello, *Proc. Natl. Acad. Sci. U. S. A.*, 2018, **115**, 10251–10256.

43 J. Taborski, P. Väterlein, H. Dietz, U. Zimmermann and E. Umbach, *J. Electron Spectros. Relat. Phenomena*, 1995, **75**, 129–147.

44 R. Resel, *J. Phys. Condens. Matter*, , DOI:10.1088/0953-8984/20/18/184009.

45 S. E. Fritz, S. M. Martin, C. D. Frisbie, M. D. Ward and M. F. Toney, *J. Am. Chem. Soc.*, 2004, **126**, 4084–4085.

46 A. C. Mayer, A. Kazimirov and G. G. Malliaras, *Phys. Rev. Lett.*, 2006,

97, 1–4.

47 S. Pachmajer, A. O. F. Jones, M. Truger, C. Röthel, I. Salzmann, O. Werzer and R. Resel, *ACS Appl. Mater. Interfaces*, 2017, **9**, 11977–11984.

48 H. Iino, T. Usui and J. I. Hanna, *Nat. Commun.*, 2015, **6**, 6828.

49 H. Wu, H. Iino and J. I. Hanna, *ACS Appl. Mater. Interfaces*, 2020, **12**, 29497–29504.

50 A. Sanzone, S. Mattiello, G. M. Garavaglia, A. M. Calascibetta, C. Ceriani, M. Sassi and L. Beverina, *Green Chem.*, 2019, **21**, 4400–4405.

51 D. Nečas and P. Klapetek, *Cent. Eur. J. Phys.*, 2012, **10**, 181–188.

52 R. Resel, E. Tamas, B. Sonderegger, P. Hofbauer and J. Keckes, *J. Appl. Crystallogr.*, 2003, **36**, 80–85.

53 A. Moser, I. Salzmann, M. Oehzelt, A. Neuhold, H. G. Flesch, J. Ivanco, S. Pop, T. Toader, D. R. T. Zahn, D. M. Smilgies and R. Resel, *Chem. Phys. Lett.*, 2013, **574**, 51–55.

54 E. Fumagalli, M. Campione, L. Raimondo, A. Sassella, M. Moret, L. Barba and G. Arrighetti, *J. Synchrotron Radiat.*, 2012, **19**, 682–687.

55 B. Schrode, S. Pachmajer, M. Dohr, C. Röthel, J. Domke, T. Fritz, R. Resel and O. Werzer, *J. Appl. Crystallogr.*, 2019, **52**, 683–689.

56 J. Simbrunner, C. Simbrunner, B. Schrode, C. Röthel, N. Bedoya-Martinez, I. Salzmann and R. Resel, *Acta Crystallogr. Sect. A Found. Adv.*, 2018, **74**, 373–387.

57 S. Plimpton, *J. Comput. Phys.*, 1995, **117**, 1–19.

58 B. R. Brooks, C. . Brooks, A. D. Mackerell, L. Nilsson, R. J. Petrella, B. Roux, Y. Won, G. Archontis, C. Bartels, S. Boresch, A. Caflisch, L. Caves, Q. Cui, A. R. Dinner, M. Feig, S. Fischer, J. Gao, M. Hodoscek, W. Im, K. Kuczera, T. Lazaridis, J. Ma, V. Ovchinnikov, E. Paci, R. W. Pastor, C. B. Post, J. Z. Pu, M. Schaefer, B. Tidor, R. M. Venable, H. L. Woodcock, X. Wu, W. Yang, Y. D.M and M. Karplus, *J. Comput. Chem.*, 2009, **30**, 1545–1614.

59 M. Dohr, O. Werzer, Q. Shen, I. Salzmann, C. Teichert, C. Ruzié, G. Schweicher, Y. H. Geerts, M. Sferrazza and R. Resel, *ChemPhysChem*, 2013, **14**, 2554–2559.

60 O. Werzer, B. Stadlober, A. Haase, M. Oehzelt and R. Resel, *Eur. Phys.*

J. B, 2008, **66**, 455–459.

61 A. Neuhold, S. Fladischer, S. Mitsche, H. G. Flesch, A. Moser, J. Novak, D. M. Smilgies, E. Kraker, B. Lamprecht, A. Haase, W. Grogger and R. Resel, *J. Appl. Phys.*, , DOI:10.1063/1.3667171.

62 S. Hofer, W. Bodlos, J. Novák, A. Sanzone, L. Beverina and R. Resel, *Liq. Cryst.*, 2021, **0**, 1–9.

63 S. Hofer, J. Unterkofler, M. Kaltenegger, G. Schweicher, C. Ruzié, A. Tamayo, T. Salzillo, M. Mas-Torrent, A. Sanzone, L. Beverina, Y. Geerts and R. Resel, *Chem. Mater.*

64 A. Moser, J. Novák, H. G. Flesch, T. Djuric, O. Werzer, A. Haase and R. Resel, *Appl. Phys. Lett.*, , DOI:10.1063/1.3665188.

65 T. Kakudate, N. Yoshimoto and Y. Saito, *Appl. Phys. Lett.*, 2007, **90**, 130–133.

66 S. F. S. P. Looijmans, D. Cavallo, L. Yu and G. W. M. Peters, *Cryst. Growth Des.*, 2018, **18**, 3921–3926.

67 D. Cavallo, F. Galli, L. Yu and G. C. Alfonso, *Cryst. Growth Des.*, 2017, **17**, 2639–2645.

68 S. Chen, H. Xi and L. Yu, *J. Am. Chem. Soc.*, 2005, **127**, 17439–17444.

69 H. L. Cheng, Y. S. Mai, W. Y. Chou, L. R. Chang and X. W. Liang, *Adv. Funct. Mater.*, 2007, **17**, 3639–3649.

70 C. Desgranges and J. Delhommelle, *J. Am. Chem. Soc.*, 2006, **128**, 10368–10369.

71 D. K. Owens and R. C. Wendt, *J. Appl. Polym. Sci.*, 1969, **13**, 1741–1747.

72 H. Ebata, T. Izawa, E. Miyazaki, K. Takimiya, M. Ikeda, H. Kuwabara and T. Yui, *J. Am. Chem. Soc.*, 2007, **129**, 15732–15733.

73 H. Minemawari, T. Yamada, H. Matsui, J. Y. Tsutsumi, S. Haas, R. Chiba, R. Kumai and T. Hasegawa, *Nature*, 2011, **475**, 364–367.

74 T. Izawa, E. Miyazaki and K. Takimiya, *Adv. Mater.*, 2008, **20**, 3388–3392.

75 H. Spreitzer, B. Kaufmann, C. Ruzié, C. Röthel, T. Arnold, Y. H. Geerts, C. Teichert, R. Resel and A. O. F. Jones, *J. Mater. Chem. C*, 2019, **7**, 8477–8484.

76 L. Lyu, D. Niu, H. Xie, Y. Zhao, N. Cao, H. Zhang, Y. Zhang, P. Liu and Y. Gao, *Phys. Chem. Chem. Phys.*, 2017, **19**, 1669–1676.

77 H. Iino and J. I. Hanna, *Adv. Mater.*, 2011, **23**, 1748–1751.

78 H. Iino and J. I. Hanna, *Polym. J.*, 2017, **49**, 23–30.

79 S. Inoue, H. Minemawari, J. Tsutsumi, M. Chikamatsu, T. Yamada, S. Horiuchi, M. Tanaka, R. Kumai, M. Yoneya and T. Hasegawa, *Chem. Mater.*, 2015, **27**, 3809–3812.

80 H. Wu, H. Iino and J. I. Hanna, *RSC Adv.*, 2017, **7**, 56586–56593.

81 H. Minemawari, J. Tsutsumi, S. Inoue, T. Yamada, R. Kumai and T. Hasegawa, *Appl. Phys. Express*, 2014, **7**, 2–5.

82 H. Iino and J. I. Hanna, *Mol. Cryst. Liq. Cryst.*, 2017, **647**, 37–43.

83 A. O. F. Jones, C. Röthel, R. Lassnig, O. N. Bedoya-Martínez, P. Christian, I. Salzmann, B. Kunert, A. Winkler and R. Resel, *CrystEngComm*, 2017, **19**, 1902–1911.

84 *J. Appl. Crystallogr.*, 2007, **40**, 202.

85 S. Pensec, F. G. Tournilhac and P. Bassoul, *J. Phys. II*, 1996, **6**, 1597–1605.

86 M. Jasiurkowska, A. Budziak, J. Czub, M. Massalska-Arodź and S. Urban, *Liq. Cryst.*, 2008, **35**, 513–518.

87 S. Diele, S. Tosch, S. Mahnke and D. Demus, *Cryst. Res. Technol.*, 1991, **26**, 809–817.

88 J. M. Seddon, *Handb. Liq. Cryst. Set*, 2008, 635–679.

89 R. Hosemann, *J. Appl. Phys.*, 1963, **34**, 25–41.

90 R. Bonart, R. Hosemann and R. L. McCullough, *Polymer (Guildf).*, 1963, **4**, 199–211.

91 A. O. F. Jones, B. Chattopadhyay, Y. H. Geerts and R. Resel, *Adv. Funct. Mater.*, 2016, **26**, 2233–2255.

92 K. Horiuchi, Y. Yamamura, R. Pełka, M. Sumita, S. Yasuzuka, M. Massalska-Arodz and K. Saito, *J. Phys. Chem. B*, 2010, **114**, 4870–4875.

93 K. Saito, T. Miyazawa, A. Fujiwara, M. Hishida, H. Saitoh, M. Massalska-Arodź and Y. Yamamura, *J. Chem. Phys.*, , DOI:10.1063/1.4821162.

94 T. Miyazawa, Y. Yamamura, M. Hishida, S. Nagatomo, M. Massalska-Arodź and K. Saito, *J. Phys. Chem. B*, 2013, **117**, 8293–8299.

95 S. Himmelberger, D. T. Duong, J. E. Northrup, J. Rivnay, F. P. V. Koch, B. S. Beckingham, N. Stingelin, R. A. Segalman, S. C. B. Mannsfeld and A. Salleo, *Adv. Funct. Mater.*, 2015, **25**, 2616–2624.

96 M. Casalegno, T. Nicolini, A. Famulari, G. Raos, R. Po and S. V. Meille, *Phys. Chem. Chem. Phys.*, 2018, **20**, 28984–28989.

97 B. Schrode, A. O. F. Jones, R. Resel, N. Bedoya, R. Schennach, Y. H. Geerts, C. Ruzié, M. Sferrazza, A. Brillante, T. Salzillo and E. Venuti, *ChemPhysChem*, 2018, **19**, 993–1000.

98 V. Coropceanu, J. Cornil, D. A. da Silva Filho, Y. Olivier, R. Silbey and J.-L. Brédas, *Chem. Rev.*, 2007, **107**, 926–952.

99 A. Köhler and H. Bässler, *Electronic Processes in Organic Semiconductors: An Introduction*, Wiley, 2015.

100 A. V Chadwick and J. N. Sherwood, in *Point Defects in Solids: Volume 2 Semiconductors and Molecular Crystals*, eds. J. H. Crawford and L. M. Slifkin, Springer US, Boston, MA, 1975, pp. 441–475.

101 F. Liu, D. E. Hooks, N. Li, J. F. Rubinson, J. N. Wacker and J. A. Swift, *Chem. Mater.*, 2020, **32**, 3952–3959.

102 I. A. Olson, A. G. Shtukenberg, B. Kahr and M. D. Ward, *Reports Prog. Phys.*, 2018, **81**, 96501.

103 J. N. Sherwood, *Mol. Cryst. Liq. Cryst.*, 1976, **32**, 37–38.

104 I. V. Kityk, B. Marciniak and A. Mefleh, *J. Phys. D. Appl. Phys.*, 2001, **34**, 1–4.

105 N. Karl, 2001, 283–326.

106 S. V. Izvekov and V. I. Sugakov, *Phys. Status Solidi*, 1995, **191**, 449–453.

107 B. D. Chapman, A. Checco, R. Pindak, T. Siegrist and C. Kloc, *J. Cryst. Growth*, 2006, **290**, 479–484.

108 D. W. Bennett, *Understanding Single-Crystal X-Ray Crystallography*, Wiley, 2010.

109 M. Haruta and H. Kurata, *Sci. Rep.*, 2012, **2**, 2–5.

110 E. J. Chan and D. J. Goossens, *Acta Crystallogr. Sect. B Struct. Sci.*,

2012, **68**, 80–88.

111 T. R. Welberry and T. Weber, *Crystallogr. Rev.*, 2016, **22**, 2–78.

112 G. K. Williamson and W. H. Hall, *Acta Metall.*, 1953, **1**, 22–31.

113 J. F. M. Hardigree, I. R. Ramirez, G. Mazzotta, C. Nicklin and M. Riede, *Appl. Phys. Lett.*, , DOI:10.1063/1.4995571.

114 H.-J. Brandt, R. Resel, J. Keckes, B. Koppelhuber-Bitschnau, N. Koch and G. Leising, *MRS Proc.*, 1999, **561**, 161.

115 G. Schweicher, N. Paquay, C. Amato, R. Resel, M. Koini, S. Talvy, V. Lemaur, J. Cornil, Y. Geerts and G. Gbabode, *Cryst. Growth Des.*, 2011, **11**, 3663–3672.

116 H. A. Becerril, M. E. Roberts, Z. Liu, J. Locklin and Z. Bao, *Adv. Mater.*, 2008, **20**, 2588–2594.

117 F. G. Del Pozo, S. Fabiano, R. Pfattner, S. Georgakopoulos, S. Galindo, X. Liu, S. Braun, M. Fahlman, J. Veciana, C. Rovira, X. Crispin, M. Berggren and M. Mas-Torrent, *Adv. Funct. Mater.*, 2016, **26**, 2379–2386.

118 I. Temiño, F. G. Del Pozo, M. R. Ajayakumar, S. Galindo, J. Puigdollers and M. Mas-Torrent, *Adv. Mater. Technol.*, , DOI:10.1002/admt.201600090.

119 B. Schrode, S. Pachmajer, M. Dohr, C. Röthel, J. Domke, T. Fritz, R. Resel and O. Werzer, *J. Appl. Crystallogr.*, 2019, **52**, 683–689.

120 M. Dohr, H. M. A. Ehmann, A. O. F. Jones, I. Salzmann, Q. Shen, C. Teichert, C. Ruzié, G. Schweicher, Y. H. Geerts, R. Resel, M. Sferrazza and O. Werzer, *Soft Matter*, 2017, **13**, 2322–2329.

121 M. Oehzelt, G. Koller, J. Ivanco, S. Berkebile, T. Haber, R. Resel, F. P. Netzer and M. G. Ramsey, *Adv. Mater.*, 2006, **18**, 2466–2470.

122 H. P. Klug and L. E. Alexander, *X-Ray Diffraction Procedures: For Polycrystalline and Amorphous Materials, 2nd Edition*, 1974.

123 B. E. Warren, *X-ray Diffraction*, Dover Publications, 1990.

124 S. Urban and C. M. Roland, *J. Non. Cryst. Solids*, 2011, **357**, 740–745.

125 S. Urban, J. Czub, J. Przedmojski, R. Dąbrowski and M. Geppi, *Mol. Cryst. Liq. Cryst.*, 2007, **477**, 87/[581]-100/[594].

126 K. Satoh, *J. Chem. Phys.*, , DOI:10.1063/1.4793524.

127 C. Legrand, J. P. Parneix, A. Chapoton and N. H. Tinh, *J. Phys. Lettres*, 1984, **45**, 283–288.

128 N. Osiecka, M. Massalska-Arodź, Z. Galewski, K. Chłędowska and A. Bąk, *Phys. Rev. E - Stat. Nonlinear, Soft Matter Phys.*, 2015, **92**, 1–5.

129 D. Marquardt, F. A. Heberle, T. Miti, B. Eicher, E. London, J. Katsaras and G. Pabst, *Langmuir*, 2017, **33**, 3731–3741.

130 M. Mas-Torrent and C. Rovira, *Chem. Rev.*, 2011, **111**, 4833–4856.

131 J. Socci, T. Salzillo, R. G. Della Valle, E. Venuti and A. Brillante, *Solid State Sci.*, 2017, **71**, 146–151.

132 T. Matsukawa, M. Yoshimura, M. Uchiyama, M. Yamagishi, A. Nakao, Y. Takahashi, J. Takeya, Y. Kitaoka, Y. Mori and T. Sasaki, *Jpn. J. Appl. Phys.*, 2010, **49**, 085502.

133 T. Kakudate, N. Yoshimoto and Y. Saito, *Appl. Phys. Lett.*, 2007, **90**, 081903.

134 T. Salzillo, N. Montes, R. Pfattner and M. Mas-Torrent, *J. Mater. Chem. C*, 2020, **8**, 15361–15367.

135 R. Pfattner, S. T. Bromley, C. Rovira and M. Mas-Torrent, *Adv. Funct. Mater.*, 2016, **26**, 2256–2275.

136 S. Galindo, A. Tamayo, F. Leonardi and M. Mas-Torrent, *Adv. Funct. Mater.*, 2017, **27**, 1700526.

137 A. Brillante, I. Bilotti, R. G. Della Valle, E. Venuti, S. Milita, C. Dionigi, F. Borgatti, A. N. Lazar, F. Biscarini, M. Mas-Torrent, N. S. Oxtoby, N. Crivillers, J. Veciana, C. Rovira, M. Leufgen, G. Schmidt and L. W. Molenkamp, *CrystEngComm*, 2008, **10**, 1899.

138 E. Benvenuti, D. Gentili, F. Chiarella, A. Portone, M. Barra, M. Cecchini, C. Cappuccino, M. Zambianchi, S. G. Lopez, T. Salzillo, E. Venuti, A. Cassinese, D. Pisignano, L. Persano, M. Cavallini, L. Maini, M. Melucci, M. Muccini and S. Toffanin, *J. Mater. Chem. C*, 2018, **6**, 5601–5608.

139 L. Antolini, G. Horowitz, F. Kouki and F. Garnier, *Adv. Mater.*, 1998, **10**, 382–385.

140 S. M. Gali, C. Quarti, Y. Olivier, J. Cornil, L. Truflandier, F. Castet, L. Muccioli and D. Beljonne, *J. Mater. Chem. C*, 2019, **7**, 4382–4391.

141 A. Y. Sosorev, D. R. Maslennikov, I. Y. Chernyshov, D. I. Dominskiy, V. V. Bruevich, M. V. Vener and D. Y. Paraschuk, *Phys. Chem. Chem.*

Phys., 2018, **20**, 18912–18918.

142 S. H. Wen, A. Li, J. Song, W. Q. Deng, K. L. Han and W. A. Goddard, *J. Phys. Chem. B*, 2009, **113**, 8813–8819.

143 G. Schweicher, G. D'Avino, M. T. Ruggiero, D. J. Harkin, K. Broch, D. Venkateshvaran, G. Liu, A. Richard, C. Ruzié, J. Armstrong, A. R. Kennedy, K. Shankland, K. Takimiya, Y. H. Geerts, J. A. Zeitler, S. Fratini and H. Sirringhaus, *Adv. Mater.*, , DOI:10.1002/adma.201902407.

144 A. Troisi and G. Orlandi, *J. Phys. Chem. A*, 2006, **110**, 4065–4070.

145 E. G. Bittle, A. J. Biacchi, L. A. Fredin, A. A. Herzing, T. C. Allison, A. R. Hight Walker and D. J. Gundlach, *Commun. Phys.*, 2019, **2**, 27.

146 H. Minemawari, M. Tanaka, S. Tsuzuki, S. Inoue, T. Yamada, R. Kumai, Y. Shimoi and T. Hasegawa, *Chem. Mater.*, 2017, **29**, 1245–1254.

147 H. Minemawari, J. Tsutsumi, S. Inoue, T. Yamada, R. Kumai and T. Hasegawa, *Appl. Phys. Express*, 2014, **7**, 8–11.

148 T. Salzillo, F. D'Amico, N. Montes, R. Pfattner and M. Mas-Torrent, *CrystEngComm*, 2020, 10.1039/d0ce01467b.

149 A. Tamayo, S. Riera-Galindo, A. O. F. Jones, R. Resel and M. Mas-Torrent, *Adv. Mater. Interfaces*, 2019, **6**, 1900950.

150 X. L. Chen, A. J. Lovinger, Z. Bao and J. Sapjeta, *Chem. Mater.*, 2001, **13**, 1341–1348.

151 J. Wade, F. Steiner, D. Niedzialek, D. T. James, Y. Jung, D. J. Yun, D. D. C. Bradley, J. Nelson and J. S. Kim, *J. Mater. Chem. C*, 2014, **2**, 10110–10115.

152 Y. Diao, B. C. K. Tee, G. Giri, J. Xu, D. H. Kim, H. A. Becerril, R. M. Stoltenberg, T. H. Lee, G. Xue, S. C. B. Mannsfeld and Z. Bao, *Nat. Mater.*, 2013, **12**, 665–671.

153 S. S. Lee, M. A. Loth, J. E. Anthony and Y. L. Loo, *J. Am. Chem. Soc.*, 2012, **134**, 5436–5439.

154 J. Chen, M. Shao, K. Xiao, A. J. Rondinone, Y. L. Loo, P. R. C. Kent, B. G. Sumpter, D. Li, J. K. Keum, P. J. Diemer, J. E. Anthony, O. D. Jurchescu and J. Huang, *Nanoscale*, 2014, **6**, 449–456.

155 G. Giri, E. Verploegen, S. C. B. Mannsfeld, S. Atahan-Evrenk, D. H. Kim, S. Y. Lee, H. A. Becerril, A. Aspuru-Guzik, M. F. Toney and Z. Bao, *Nature*, 2011, **480**, 504–508.

156 G. Giri, D. M. Delongchamp, J. Reinspach, D. A. Fischer, L. J. Richter, J. Xu, S. Benight, A. Ayzner, M. He, L. Fang, G. Xue, M. F. Toney and Z. Bao, *Chem. Mater.*, 2015, **27**, 2350–2359.

157 Y. Diao, L. Shaw, Z. Bao and S. C. B. Mannsfeld, *Energy Environ. Sci.*, 2014, **7**, 2145–2159.

158 Y. Diao, K. M. Lenn, W. Y. Lee, M. A. Blood-Forsythe, J. Xu, Y. Mao, Y. Kim, J. A. Reinspach, S. Park, A. Aspuru-Guzik, G. Xue, P. Clancy, Z. Bao and S. C. B. Mannsfeld, *J. Am. Chem. Soc.*, 2014, **136**, 17046–17057.

159 S. Riera-Galindo, A. Tamayo and M. Mas-Torrent, *ACS Omega*, 2018, **3**, 2329–2339.

160 M. R. Niazi, R. Li, M. Abdelsamie, K. Zhao, D. H. Anjum, M. M. Payne, J. Anthony, D. M. Smilgies and A. Amassian, *Adv. Funct. Mater.*, 2016, **26**, 2371–2378.

161 M. R. Niazi, R. Li, E. Qiang Li, A. R. Kirmani, M. Abdelsamie, Q. Wang, W. Pan, M. M. Payne, J. E. Anthony, D. M. Smilgies, S. T. Thoroddsen, E. P. Giannelis and A. Amassian, *Nat. Commun.*, 2015, **6**, 8598.

162 D. Grosso, *J. Mater. Chem.*, 2011, **21**, 17033.

163 M. Faustini, B. Louis, P. A. Albouy, M. Kuemmel and D. Grosso, *J. Phys. Chem. C*, 2010, **114**, 7637–7645.

164 M. Kunii, H. Iino and J. Hanna, *Appl. Phys. Lett.*, 2017, **110**, 243301.

165 J. M. Cho and T. Mori, *Phys. Rev. Appl.*, 2016, **5**, 064017.

166 F. G. Del Pozo, S. Fabiano, R. Pfattner, S. Georgakopoulos, S. Galindo, X. Liu, S. Braun, M. Fahlman, J. Veciana, C. Rovira, X. Crispin, M. Berggren and M. Mas-Torrent, *Adv. Funct. Mater.*, 2016, **26**, 2379–2386.

167 J. Smith, W. Zhang, R. Sougrat, K. Zhao, R. Li, D. Cha, A. Amassian, M. Heeney, I. McCulloch and T. D. Anthopoulos, *Adv. Mater.*, 2012, **24**, 2441–2446.

168 L. J. Richter, D. M. Delongchamp and A. Amassian, *Chem. Rev.*, 2017, **117**, 6332–6366.

169 A. F. Paterson, N. D. Treat, W. Zhang, Z. Fei, G. Wyatt-Moon, H. Faber, G. Vourlias, P. A. Patsalas, O. Solomeshch, N. Tessler, M. Heeney and T. D. Anthopoulos, *Adv. Mater.*, 2016, **28**, 7791–7798.